Characteristics of summer snow areas on glaciers observed by means of Landsat data

DOCTORAL THESIS

for the qualification of
Doctor rerum naturalium

Institute of Meteorology and Geophysics

Leopold – Franzens University

Innsbruck

Submitted by

Mag. rer. nat. Gabriele Bippus

Innsbruck, August 2011

Untersuchung von Schneeflächen auf Gletschern im Sommer mittels Landsat Daten

DISSERTATION

für das Erlangen des akademischen Grades
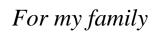
Doctor rerum naturalium

Institut für Meteorologie und Geophysik

Leopold – Franzens Universität

Innsbruck

Vorgelegt von

Mag. rer. nat. Gabriele Bippus

Innsbruck, August 2011

For my family

Abstract

In order to observe changes in climate and associated impact on the environment, a set of essential climate variables (ECV) has been defined, including inter alia glaciers and icecaps. Regular field measurements on glaciers are limited to a small number of glaciers world-wide. On the other hand, satellite sensors deliver observations of glaciers and icecaps world–wide at comparatively high spatial resolution. Such data are now already available for about 30 years providing the possibility to investigate past and present changes on glaciers and icecaps. Different to changes in the total glacier extent, which have a typical response time to changes in climate of several years to decades, the seasonal and annual extents of the accumulation and ablation areas are closely related to a glacier's mass balance. Snow area extent on a glacier in late summer, the topic addressed by this thesis, can be used as proxy for the accumulation area ratio and consequently as an indicator for mass balance.

The main objective of this thesis was the retrieval of late summer snow areas on glaciers in different geographic regions and thus to supply evidence on mass balance behaviour. As data base Landsat imagery, supplied by the U.S. Geological Survey, was selected due to the large archived data base and the free availability since 2009. Digital elevation models are used in the processing line to correct for topographic illumination effects and atmospheric propagation in the Landsat scenes, and to study area-altitude distributions for snow and ice areas. National DEMs were available for Austria and Norway. In other regions, freely available DEMs of the SRTM, ASTER G–DEM, GETASSE or VIEWFINDER are used. Additionally to Landsat images and a digital elevation model, glacier outlines are required for the processing line. Most of the glacier outlines were obtained either from the Global Land Ice Measurements from Space (GLIMS) data base or from the ESA DUE GlobGlacier project. The near infrared band of Landsat was selected for retrieving snow and ice areas because visible bands are often saturated.

After radiometric calibration and topographic correction of the Landsat image, the resulting map was combined with the glacier outlines to derive a statistical distribution of the topographically corrected top of atmosphere reflectance (TOAR) over the glacier areas. Based on the statistic of reflectance values and visual controlling using auxiliary maps, a threshold was selected and applied on the topographically corrected TOAR map to retrieve the snow areas on glaciers. The derived snow areas were validated using orthophotos of several glaciers in Austria and Norway. Furthermore, possible errors in the retrieved snow areas related to the quality of the digital elevation model used in the processing line and to the applied threshold for the discrimination of snow and ice were investigated.

In order to study geographic patterns of late summer snow areas, glaciers located in Alaska, Austria, Chile, the Canadian Arctic, Greenland, Nepal and Norway were investigated. The long-term behaviour was analysed using Landsat images acquired

between the mid 1980's and 2010. Variations of snow areas in several years were investigated in all regions except Greenland, where multiple images were not available. The derived snow areas were related to the total glacier area in each region, as well as to individual glacier areas to derive the late summer snow area ratio (LSSAR), which can be used as proxy for the accumulation area ratio (AAR) if the image was acquired close to the end of a mass balance year. Additionally, the statistics of snow areas for individual glaciers in each region were analysed taking into account the glacier area and the glacier orientation. The derived snow areas were related to long term temperature and precipitation data series from the NCEP / NCAR Reanalysis.

On glaciers in all regions a decrease of the snow areas in late summer can be observed from the mid 1980's to present. The smallest variations are found for the North Patagonian Icefield in Chile and the largest variations are found for glaciers in northern Norway. A decrease of the late summer snow area ratio from about 0.39 in 1985 to 0.01 in 2010 was derived for the Barnes Icecap in the Canadian Arctic. The derived LSSARs of individual glaciers in the selected regions were compared to AARs reported in the literature. Using the long-term mass balance measurements of the Vernagtferner in the Ötztal Alps, Austria, the derived LSSARs approximate the measured AARs in most of the investigated years rather well. The Landsat image acquisition date is thereby the main limiting factor for estimating AAR which is measured at the end of a mass balance year. The analysis of snow areas confirms that small glaciers are more sensitive to variations in seasonal and annual meteorological conditions than large glaciers. This can be observed for glaciers in all investigated regions. No general trend regarding glacier orientation was found in any of the investigated regions for snow/ice area ratio. Annual variations of the snow areas rather depend on the local topographic conditions and meteorological influences on the individual glaciers.

Zusammenfassung

Gletscher und Eiskappen gehören zu einer Reihe von essentiellen Klima Variablen, deren Beobachtung Rückschlüsse auf Klimaänderungen und deren Einfluss auf die Umwelt ermöglichen. Regelmäßige Feldarbeiten werden nur auf einigen wenigen Gletschern und Eiskappen weltweit durchgeführt. Satellitendaten hingegen ermöglichen die Beobachtung von Gletschern und Eiskappen weltweit mit einer vergleichsweise hohen räumlichen Auflösung. Solche Daten gibt es inzwischen für die letzten 30 Jahre. Diese ermöglichen die Untersuchung von vergangenen und gegenwärtigen Änderungen von Gletschern und Eiskappen. Im Gegensatz zur Gesamtfläche eines Gletschers, welche eine typische Reaktionszeit von einigen Jahren bis Jahrzehnten auf Klimaänderungen hat, können Veränderungen der Akkumulations- und Ablationsflächen auf einem Gletscher saisonal und jährlich beobachtet werden. Die Ausdehnungen dieser Flächen stehen in enger Verbindung zur Massenbilanz eines Gletschers. Die Schneebedeckungen auf Gletschern im Spätsommer, welche im Rahmen dieser Arbeit untersucht wurden, können als Annäherungen für die Akkumulationsflächen, und somit als Messgrößen für die Massenbilanzen verwendet werden.

Das Hauptziel dieser Arbeit war, Schnee- und Eisflächen auf Gletschern am Ende des Sommers in unterschiedlichen geographischen Lagen zu bestimmen, um somit Aussagen über das Massenbilanzverhalten der Gletscher machen zu können. Landsat Szenen, die vom U.S. Geological Survey zur Verfügung gestellt werden, wurden als Datengrundlage gewählt, da von diesen Satelliten eine großes Menge an Daten archiviert ist, und diese seit 2009 frei erhältlich sind. Für die Prozessierung der Daten werden digitale Höhenmodelle verwendet, um einerseits topographisch bedingte Beleuchtungseffekte und deren Ausbreitung durch die Atmosphäre in der Landsat Szenen zu filtern, und um andererseits die Flächen – Höhen Verteilungen der Schnee- und Eisflächen zu untersuchen. Für die Regionen in Österreich und Norwegen standen nationale Höhenmodelle zur Verfügung. Für die anderen Regionen wurden frei erhältliche Höhenmodelle von SRTM, ASTER G-DEM, GETASSE oder VIEWFINDER verwendet. Zusätzlich zu Landsat Daten und einem digitalen Geländemodell werden Gletschergrenzen für die Prozessierung benötigt. Die meisten dieser Gletschergrenzen stammen entweder von der GLIMS (Global Land Ice Measurements from Space) Datenbank, oder von dem DUE GlobGlacier Projekt, das von der ESA (European Space Agency) initiiert wurde. Der Landsat Kanal 4, der im nahen Infrarot arbeitet, wurde für die Unterscheidung von Schnee- und Eisflächen verwendet, da das Signal im sichtbaren Spektralbereich oft gesättigt ist.

Die Landsat Szene wird radiometrisch kalibriert und anschließend topographisch korrigiert. Die resultierende Szene wird mit den Gletschergrenzen überlagert um eine statistische Verteilung der topographisch korrigierten spektralen Reflexion von Gletscheroberflächen am oberen Rand der Atmosphäre zu erhalten. Auf Grund dieser Statistik der spektralen Reflexion und mit Hilfe von zusätzlichem Kartenmaterial für

visuelle Vergleiche wird ein Schwellwert ermittelt, dessen Anwendung auf die topographisch korrigierte spektrale Reflexion die Schneeflächen auf den Gletschern liefert. Die erhaltenen Schneeflächen wurden mit Hilfe von Orthophotos von einigen Gletschern in Österreich und Norwegen validiert. Außerdem wurden mögliche Fehlerquellen bei der Prozessierung von Schneeflächen untersucht, insbesondere der Einfluss der Qualität des digitalen Höhenmodells, welches für die Prozessierung verwendet wurde, sowie der des ausgewählten Schwellwertes zur Unterscheidung von Schnee und Eis.

Um geographische Muster in den Schneeflächen am Ende des Sommers zu analysieren wurden Gletscher in Alaska, Österreich, Chile, Grönland, Nepal, Norwegen und in der Kanadischen Arktis untersucht. Außerdem wurden Landsat Szenen prozessiert, die zwischen Mitte der 1980er Jahre und 2010 aufgenommen wurden, um das Verhalten dieser Flächen über einen längeren Zeitraum zu analysieren. Die Veränderung der Schneeflächen in mehreren Jahren wurde in allen Gebieten außer Grönland untersucht, da mehrfache Szenen, welche die Grundvoraussetzungen erfüllen, für diese Region nicht verfügbar waren. Die erhaltenen Schneeflächen wurden auf die gesamte Gletscherfläche in jeder Region bezogen, sowie für einzelne Gletscher analysiert, um das Verhältnis der Schneefläche zur Gesamtfläche der Gletscher am Ende des Sommers zu untersuchen. Sofern die verwendete Szene nahezu am Ende eines Massenbilanzjahres aufgenommen wurde, kann dieses Verhältnis als Annäherung für das Verhältnis der Akkumulationsfläche zur gesamten Gletscherfläche (AAR) genützt werden. Zusätzlich wurden Statistiken der Schneeflächen für einzelne Gletscher in jeder Region analysiert, unter Berücksichtigung der Gletschergröße und der Exposition der Gletscher. Zeitreihen der NCEP / NCAR Reanalyse von Temperatur und Niederschlag wurden verwendet um mögliche Beziehungen zu den erhaltenen Schneeflächen zu finden.

In allen Regionen konnte seit Mitte der 1980er Jahre bis 2010 eine Abnahme der Schneeflächen auf den Gletschern im Spätsommer beobachtet werden. Die geringsten Änderungen wurden für das Nord Patagonische Eisfeld in Chile gefunden, die größten für Gletscher im Norden von Norwegen. Auf dem Barnes Icecap in der Kanadischen Arktis reduzierte sich das Verhältnisse der Schneefläche zu gesamten Gletscherfläche von 0.39 in 1985 auf 0.01 in 2010. Die errechneten Schneeflächenverhältnisse von einzelnen Gletschern in den untersuchten Regionen wurden mit publizierten AAR verglichen. Der Vergleich von AAR aus langjährigen Massenbilanz Messungen am Vernagtferner in den Ötztaler Alpen in Österreich mit den errechneten Schneeflächenverhältnissen zeigt in den meisten untersuchten Jahren eine gute Übereinstimmung. Für die Abschätzung des AAR, das am Ende eines Massenbilanzjahres gemessen wird, ist das Aufnahmedatum einer Landsat Szene der größte limitierende Faktor. Die Untersuchung der Schneeflächen bestätigt, dass kleine Gletscher schneller auf saisonale und jährliche Veränderungen der meteorologischen Bedingungen reagieren als große Gletscher. Diese Beobachtung gilt für Gletscher in allen untersuchten Regionen. Bezüglich der Gletscher Exposition konnte in keiner der untersuchten Regionen ein genereller Trend des Schneeflächenverhältnisses

gefunden werden. Jährliche Veränderungen der Schneeflächen hängen vielmehr von der lokalen Topographie und den meteorologischen Einflüssen auf einen Gletscher ab.

Table of Contents

List of Figures

List of Tables

List of Symbols / Abbreviations

a.s.l.	above sea level
AAR	Accumulation Area Ratio
ACE	Altimeter Corrected Elevations
ASTER	Advanced Spaceborne Thermal Emission and Reflection Radiometer
AU	Astronomical Units
b	intercept of regression line of DN and cos(i)
B	Bias
BI	Barnes Icecap
BL	Blåmannsisen
C	C-Factor = b / m
d	earth-sun distance in astronomical units [AU]
DEM	Digital Elevation Model
DN	Digital Number
ECV	Essential Climate Variable
ELA	Equilibrium Line Altitude
EO-1 ALI	Earth Observer-1 Advanced Land Imager
ESA	European Space Agency
ETM+	Enhanced Thematic Mapper Plus
FI	Flade Isblink
G	Gain
GCOS	Global Climate Observation System
GCP	Ground Control Point
GLIMS	Global Land Ice Measurements from Space
GYGC	Grewingk-Yalik Glacier Complex
HEF	Hintereisferner
HI	Harding Icefield
HRG	High Resolution Geometric
HRVIR	High Resolution Visible and InfraRed

i	illumination angle
k	Minnaert constant
KWF	Kesselwandferner
L1G	Level 1 Geometrically Corrected Landsat data product
L1Gt	Level 1 Geometrically and Terrain Corrected Landsat data product, using DEM for topographic accuracy
L1T	Level 1 Geometrically and Terrain Corrected Landsat data product, using DEM and GCPs for topographic accuracy
LPGS	Level 1 Product Generation System
LSSAR	Late Summer Snow Area Ratio
LSSAR$_{ref}$	Late Summer Snow Area Ratio for glaciers in equilibrium
LSSIA	Late Summer Snow Ice Area
m	inclination of regression line of DN and cos(i)
MODIS	MODerate resolution Imaging Spectrometer
MODTRAN	MODerate resolution atmospheric TRANsmission
MS	MultiSpectral
MTL	Metadata file for Landsat imagery
NIR	Near InfraRed
NLAPS	National Land Archive Production System
NPI	North Patagonian Icefield
OE	Ötztal Alps
p	pressure
Pan	Panchromatic
rH	relative Humidity
RT	Radiative Transfer
SA	Sagarmatha
SHARM	Spherical HARMonics
SI	Sargent Icefield
SLC	Scan Line Corrector
SPOT	Satellite Pour l'Observation de la Terre
ST	Stubai Alps

SV	Svartisen
SWIR	Short Wave InfraRed
T	Temperature
TIR	Thermal InfraRed
TM	Thematic Mapper
TOAR	Top Of Atmosphere Reflectance
USGS	U.S. Geological Survey
UTM	Universal Transverse Mercator
VF	Vernagtferner
WGMS	World Glacier Monitoring Service
WGS84	World Geodetic System 1984
6S	Second Signal of a Satellite Signal in the Solar Spectrum
λ	wave length [nm]
φ	geographic latitude
$\rho(\lambda)$	Top-of-atmosphere (TOA) reflectance
θs	solar zenith angle
$E_{sun}(\lambda)$	solar constant at a specific wave length [W/m²]
$L(\lambda)$	spectral radiance at the sensor's aperture [W/(m² sr µm)]
$L_{max}(\lambda)$	spectral radiance that is scaled to Q_{calmax} in [W/(m² sr µm)]
$L_{min}(\lambda)$	spectral radiance that is scaled to Q_{calmin} in [W/(m² sr µm)]
Q_{cal}	quantized calibrated pixel value in DN
Q_{calmax}	maximum quantized calibrated pixel value (corresponding to $L_{max}(\lambda)$) in DN [= 255]
Q_{calmin}	minimum quantized calibrated pixel value (corresponding to $L_{min}(\lambda)$) in DN [= 1 (LPGS Products); = 0 (NLAPS Products)]

List of Symbols / Abbreviations

1. Introduction

1.1 General introduction

Climate and climate change became a topic of public interest during the last years. For better understanding the impacts of climate change on the environment, the Committee of the Global Climate Observation System (GCOS), sponsored by the World Meteorological Organization (WMO), the Intergovernmental Oceanographic Commission of the United Nations Educational, Scientific and Cultural Organization (IOC/UNESCO), United Nations Environment Programme (UNEP) and International Council for Science (ICSU), defined 50 essential climate variables (ECVs) of atmospheric, oceanographic and terrestrial domains (WMO et al., 2010). The terrestrial ECVs of high interest include inter alia topics of the cryosphere, specified by glaciers and icecaps, snow areas, icecaps and permafrost (WMO et al., 2010). Thereby, cryosphere related research areas cover a broad range of interests, including for example monitoring glacier and ice caps worldwide (e.g. GLIMS), detailed investigations on the mass balance of individual glaciers, studies on glacier volume changes, observation of glacier termini positions, snow covered areas, land and sea ice extent, contribution of melting glaciers and icecaps to sea level rise etc.

For investigations of glaciers on a global scale, remote sensing data provide a useful data base. Remote sensing data enable the investigation of large areas, even in hardly accessible regions, where glaciers and icecaps are often located. The temporal availability of remote sensing data covering a region of interest depends on the sensor and the repeat time of the satellite. Online available archives provide catalogues of remote sensing data acquired since the 1970's. One big aim is the investigation of mass balances on glaciers on global scale based on remote sensing data. Currently, such mass balance is measured regularly on a few glaciers worldwide, as the mass balance of a glacier derived from field measurements is usually extrapolated from point measurements, requiring high logistic and temporal effort.

In this work, the main focus is on the retrieval of late summer snow and ice areas (LSSIA) on glaciers as raw proxies for the accumulation and ablation areas. High or medium resolution optical satellite data are used, in order to deliver these data which are of relevance for the ECV "glaciers and icecaps". Optical satellite images are used for this task, fulfilling at least three following conditions:

1. The image has to be taken during suitable illumination conditions.

2. The image acquisition must be as close as possible to the end of summer, when the ablation area has the largest extent.

3. Glaciated areas may not be shadowed by clouds or shadows of clouds.

If these conditions are considered during the scene selection, the number of available images is significantly reduced.

If a satellite image meeting these requirements is available, snow and ice areas on glaciers can be separated due to different reflectance properties in the optical and near infrared spectral ranges. Using time series of satellite data, changes on glacier surfaces can be investigated in individual regions or over large areas with reasonable effort.

Currently, information on glacier area is available for about 100'000 glaciers covering a total area of about 240'000 km² of the estimated 160'000 glaciers worldwide, covering a total area of about 685'000 km² (WGMS, 2008). The ESA Data User Element (DUE) project DUE GlobGlacier contributed to filling gaps in the global glacier inventory, and investigating late summer snow and ice areas, elevation changes, and velocity of several hundreds to thousands of glaciers worldwide. More information about the project GlobGlacier, as well as guidelines for mapping glaciers, and detailed descriptions of all work packages are online available at http://www.globglacier.ch.

1.2 Previous glaciological research by means of optical remote sensing data

In the 1980s, first results of glaciological research based on Landsat data have been published. Pioneer publications focused on the investigation on properties of snow and ice surfaces in specific spectral ranges. Warren (1982) investigated the spectral albedo of snow and its variations due to influences of snow grain size, impurities of snow, liquid water content of snow, and the dependence of snow albedo on solar zenith angle and cloud coverage. Based on the spectral properties of snow and ice, high resolution remote sensing data have been used for snow and glacier monitoring (Rott and Markl, 1989), and to investigate glacier surfaces by calculating planetary reflectances (Hall et al., 1988).

Remote sensing data offered new possibilities of glaciological research. While glaciological field campaigns rely mainly on point measurements, remote sensing data provide data for investigations over large areas. Furthermore, repeated observations of remote regions became possible by the use of remote sensing data, while field measurements in such regions would require vast temporal and logistical efforts (Bindschadler et al., 2001). When scientists recognized the extended possibilities in glaciological research based on remote sensing data, not only the numbers, but also variety of applications increased.

Applications of optical remote sensing data for glaciological research cover a wide research field. Global glacier monitoring is the main task of the GLIMS (Global Land Ice Measurements from Space) project, initiated in the end of twentieth century as an ASTER (Advanced Spaceborne Thermal Emission and Reflection Radiometer) science team project (Raup et al., 2000). Based on high resolution optical satellite data (ASTER, and partly Landsat), glaciologists in various parts of the world map regional glacier outlines applying well defined mapping procedures (Raup and Khalsa, 2010) and provide the results to the online available GLIMS data base (Raup et al., 2007). Glacier outlines of

many glaciated regions are already online available, and the data set is further increasing. So, the retrieval of global glacier inventory is on the right track (Cogley, 2009), but knowledge on glacier mass balances varies from region to region. While some glaciers are very well investigated and observed continuously for decades, as for example Hintereisferner in the Austrian Alps (Fischer, 2010) or Størbreen in Norway (Andreassen et al., 2005), the observation and investigation of glaciers in other regions, such as the Canadian Arctic Islands, South America, and Canadian Cordillera are still in an initial status (Ohmura, 2009). For Andean glaciers, Bamber and Rivera (2007) give a review on techniques for estimating glacier mass balances from remote sensing data, including the observation of elevation changes, ice flux estimation, investigation of changing glacier areas, and the estimation of snowline and accumulation area ratio (AAR). But they also point out, that detailed investigations of Andean glaciers are rare so far, and should be extended, as for example done for glaciers in the Alps. Rabatel et al. (2005) manually determined late summer the snow lines on three French glaciers based on remote sensing data to derive the glacier mass balances and validated the results with field measurements. Their comparison of the transient snow lines derived from Landsat, SPOT, and ASTER imagery and the ELAs estimated from field measurements showed a correlation of $r^2 >$ 0.89. Based on the assumption, that the transient snow line at end of summer and the maximum extent of ablation area can be used as proxy for the equilibrium line altitude (ELA), a relation between ELA and glacier mass balance can be used to estimate glaciers' mass balances (Braithwaite, 1984).

1.3 Objectives

The two main objectives of this thesis were to develop a method for the retrieval of late summer snow and ice areas on glaciers based on optical satellite data, and to investigate spatial and temporal characteristics of this parameter in glacier regions of different climate zones world-wide. Most of the regions selected for the investigation of the late summer snow areas on glaciers were defined during the project DUE GlobGlacier based on requests of scientific users of this project and the availability of satellite data.

In support of these primary objectives, the focus on the methodological side was on the following tasks and related research questions:

1. Development of a semi-automated method to derive late summer snow and ice areas (LSSIA) on glaciers from optical satellite data.

2. Study the impact of atmospheric and terrain correction procedures for retrieval of LSSIA. For this purpose data sets from the Ötztal Alps, Austria, were used.

3. Validation and error estimation of LSSIA derived from optical satellite data using orthophotos. Suitable data sets from glaciers in the Austrian Alps and Norway were used.

4. Testing the suitability of the method to retrieve late summer snow / ice areas (LSSIA) on glaciers and icecaps in different climate zones, including glaciated areas in European Alps, Norway, Alaska, Himalaya, Greenland, Canadian Arctic and Patagonia.

5. Investigation of the influence of the applied threshold and the digital elevation model used in the processing line on the retrieved snow and ice areas on glaciers.

During the DUE GlobGlacier project the Landsat data archive with imagery acquired since the 1970's was made freely available by the U.S. Geological Survey (USGS). Additionally, a nearly global Digital Elevation Model (G–DEM) was freely made available in 2009 by the Ministry of Economy, Trade, and Industry (METI) of Japan and the United States National Aeronautics and Space Administration (NASA) based on data of the Advanced Spaceborne Thermal Emission and Reflection Radiometer (ASTER). These open data archives opened up new options for glaciological investigations in both, temporal and spatial scale. The data base was used for investigating the following research tasks and questions:

1. Investigation of spatial and temporal variations of LSSIA extent derived from optical late summer satellite images.

2. Investigation of snow area-altitude distributions in several years using DEMs for glaciers in the selected regions.

3. Are there patterns in LSSIA extents of different glaciated regions?

4. Are there any general trends in the LSSIA extents for the investigated years and / or obvious exceptions?

5. Are there relations between glacier orientation and LSSIA extent on the glaciers in the selected study regions?

6. Can the derived snow area extents be interpreted in terms of monthly temperature and precipitation anomalies derived from NCEP / NCAR Reanalysis data?

In the next Chapter, a general physical and glaciological introduction is given, explaining the scientific and physical background for this study. In Chapter 3 the applied method for the retrieval of LSSIA on glaciers is described in detail. Chapter 4 shows the applications of the developed method on glaciers located in different climate regions. Case studies are made for the summer seasons 2000 and 2001, depending on the availability of Landsat imagery meeting the requirements. Spatial and temporal variations of glacier snow and ice surfaces in different regions are presented in Chapter 5, taking into account also glacier orientation and size. NCEP / NCAR Reanalysis data are used to relate the derived snow areas to anomalies of air temperatures and surface precipitation rates from the long-term means. In the last chapter the results are summarized and suggestions on future improvements are presented.

2. Physical and glaciological background

This chapter gives an overview on the physical background of radiation fluxes in the earth - atmosphere system (section 2.1) in order to explain the signal observed by the satellites, as well as an introduction on glacier surfaces (section 2.2) and the reflectance properties of different glacier surface types (section 2.3).

2.1 Radiation transfer

The solar radiation is the main energy source on the Earth's surface. The solar constant (1368 Wm^{-2}) describes the energy flux for a mean distance from the sun to the earth at the top of the atmosphere at normal incidence. Relating this solar energy flux to the top of atmosphere as a "spherical surface", defined as four-times the spherical cross section, the mean incoming solar radiation on the top of atmosphere is about 342 W/m^2.

When the solar radiation enters the atmosphere, the intensity of radiation will be changed due to following effects:

- absorption: by the atmosphere and the surface;
- reflection: by clouds, aerosols, atmospheric gases, and by the earth's surface.

Thus, the earth surface retrieves only a part of the incoming radiation on the top of atmosphere (cf. Figure 2.1).
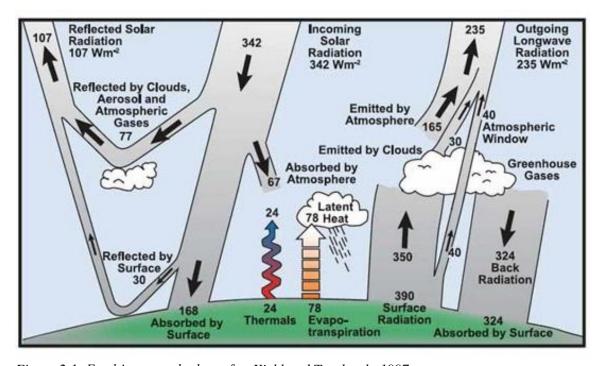
Figure 2.1: Earth's energy budget after Kiehl and Trenberth, 1997.

The radiative transfer equation describes the transport of radiation energy at a specific wavelength penetrating a layer in an absorbing and scattering medium, e.g. the atmosphere, with the thickness ds. The main processes for changes of the radiance in this medium are absorption, emission and scattering:

$$\frac{dL_\lambda}{ds} = \underbrace{\{\kappa_a(\lambda)[B_\lambda(T) - L_\lambda(\theta,\varphi)]\}}_{absorption \; / \; emission} + \underbrace{\{\kappa_s[\langle L'_\lambda\rangle - L_\lambda(\theta,\varphi)]\}}_{scattering}$$

λ	wavelength [μm]
κ_a, κ_s	absorption, scattering coefficient [m^{-1}]
L_λ	radiance of a specific wavelength [W m^{-2} sr^{-1} μm^{-1}]
ds	incremental thickness along the path
$B_\lambda(T)$	radiance of a perfect radiator [W m^{-2} sr^{-1} μm^{-1}] (Planck's law)
θ, φ	zenith and azimuth angle of the radiation
$\langle L'_\lambda\rangle$	directionally weighted mean of incoming radiation from all directions, scattered in direction (θ', φ')

$$\langle L'_\lambda\rangle = \frac{1}{4\pi}\int_0^{2\pi}\int_0^{\pi} L_\lambda(\theta',\varphi')P(\psi_s)sin\theta' d\theta' d\varphi'$$

θ', φ'	zenith and azimuth angle of the incoming radiation
ψ_s	scattering angle: angle between the directions of incoming (θ,φ) and scattered (θ',φ') radiation
$P(\psi_s)$	phase function for scattering: depends on particle size, wavelength, and number of scattering particles.

The phase function for isotropic scattering is equal 1. Isotropy means, that scattering is equal in all directions. For very small particles, as air molecules, the phase function can be described by the Rayleigh scattering approach, where scattering depends strongly on the wavelength. For particles larger than a wavelength, such as aerosols, cloud drops, or ice crystals, Mie scattering is dominant and is thus used for describing the phase function.

2.1.1 Surface albedo

The surface albedo is defined as the ratio of hemispheric fluxes of the reflected, I_r, and the incoming, I_i, radiation in the visible and infrared spectral range ($0.4 - 4$ µm):

$$a = \frac{I_r}{I_i}$$

The reflected radiation from a specific surface is again weakened in the atmosphere by the same effects as previously described. The intensity of the reflected radiation at the top of the atmosphere, as measured by a satellite sensor, varies with the wavelength, the direction of the incoming radiation, the scattering and absorption on the surface and in the atmosphere. Surface reflectance depends on the surface roughness, and the optical properties of the surface material.

Most optical satellite sensors are measuring only in parts of the reflective spectrum ($0.4 - 3$ µm), and only in discrete bands of wavelengths. To derive the total surface albedo, the reflectances of all bands in the reflective spectrum are required. For the wavelengths not covered by the satellite's sensor, the reflectances can be calculated for example by linear regression analysis, as done for Morteratschgletscher, Switzerland, by Knap et al. (1999). To derive the surface albedo from satellite measurements, the atmospheric propagation conditions have to be considered. Narrowband reflectances should be corrected for radiative effects before a narrow- to broadband albedo conversion is done.

2.1.2 Radiation at satellite

The signal retrieved by optical sensors at the top of the atmosphere depends on the wavelength and the reflection properties of the observed earth surface. Thereby, the material of the earth surface and the gaseous composite of the atmosphere determine the intensity of the radiation on the top of the atmosphere for a specific range of wavelengths, also called at-satellite radiance. Dependent on the wavelength range of the individual bands of optical satellite sensors, the signals are sensitive to gases and aerosols.

To retrieve the radiance or reflectance, respectively, at the Earth's surface, a correction for atmospheric propagation has to be taken into account. This can be done by applying a radiative transfer model, for example the 6S model (Second Signal of a Satellite Signal in the Solar Spectrum) (Vermote et al., 1997), using as input the top of atmosphere reflectance for a specific spectral range as derived from an optical satellite sensor.

Earth's surfaces hidden by water clouds and fog cannot be seen by bands working in the visible and infrared spectrum due to the absorption and scattering losses.

2.2 Glacier surfaces

2.2.1 Glacier zones

A glacier can be divided into two main mass balance zones: the accumulation zone and the ablation zone. Generally, accumulation includes all mass gains in form of snow or ice on a glacier. Ablation describes the main processes of mass loss on a glacier surface.

 Precipitation in form of snow and deposition by avalanches from surrounding slopes are the main mass sources for accumulation on a glacier surface. Mass redistribution on a glacier's surface is mainly caused by wind drift and refreezing of melt water. Snow transport due to wind drift can also contribute to ablation by transporting snow from the glacier surface to its surroundings. Depending on the temperature, the melt water can either refreeze, building a zone of superimposed ice, or drain. The latter case is the most important ablation process. Especially on glaciers located in high latitudes, sublimation can be also an important ablation process. Glaciers terminating into lakes or the sea have an additional mass loss due to calving. A detailed description of surface accumulation and ablation processes was published for example by (Cuffey and Paterson, 2010).

The boundary on a glacier, where the net accumulation and the net ablation are equal at the end of a mass balance year, is defined as the equilibrium line (Hoinkes, 1970). The mean elevation of this line, the equilibrium line altitude, can be used as a measure for estimating a glacier's annual mass balance (Braithwaite, 1984).

2.2.2 Diagenetic glacier facies

The surface of a glacier is mainly influenced by the current weather conditions, and can vary within days, or even hours, for example due to precipitation, snow deposition by strong winds or melting. In general, two states of the surface and near surface layers can be found on a glacier during a year: snow and ice.

Based on field measurements in Greenland, Benson (1958) introduced for the first time a scheme to separate the surface and near surface layers of dry snow, percolation, soaked, and ablation facies. During the following years, this scheme has been further developed, separated into layers belonging to the accumulation and the ablation zone, and extended for glaciers also in other region inter alia by Müller (1962), Paterson (1981), and Williams et al. (1991). The boundaries between the individual zones are defined by hypothetical lines. The glacier zones, associated facies, zone characteristics, and the lower limiting line, as published by Cuffey and Paterson (2010), are summarized in Table 2.1.

Glacier mass balance zone	Glacier facies zone	Zone characteristics	Lower limiting line
Accumulation zone	Dry snow zone	Permanently dry snow and firn. No melting occurs in this zone.	Dry-snow line
	Percolation zone	Surface melting can occur in this zone, but melt water percolates into the firn, resulting in a mixture of snow and ice layers.	Transient wet-snow line
	Wet-snow zone	Mixture of snow remaining from previous years, also called firn, or snow from current year and ice layers and lenses build of refrozen. Melt water drains from the percolation zone.	Transient snow line
	Superimposed ice zone	Continuous mass of refrozen melt water from winter snow on the glacier surface.	Equilibrium line
Ablation zone	Glacier ice zone	Bare ice or ice covered with rocks or dust from surrounding slopes.	Glacier front

Table 2.1: Classification of glacier zones after Cuffey and Paterson (2010).

2.3 Reflectance properties of glacier surfaces

In the visible and shortwave infrared spectral range, between $0.4 - 4.0$ µm, the energy loss from the earth's surface and in the atmosphere is mainly driven by reflectance (cf. Section 2.1). The reflectance properties of snow in the visible, near and mid infrared spectral range depend on the size and geometry of the snow grains, solid and soluble impurities in the snow layer, and, with a small effect for snow with a positive temperature, the content of liquid water (Dozier, 1989; Warren, 1982).

In the visible ($\sim0.4 - \sim0.7$ µm) and near infrared ($\sim0.7 - \sim1.4$ µm) spectral range, fresh snow reflects most of the incoming radiation, as also illustrated in Figure 2.2 showing the reflectances of different snow and ice surfaces (Hall and Martinec, 1985).

This is mainly due to the absence of impurities and liquid water in fresh snow and the small grain size. The meteorological conditions after a snow fall event are decisive for the occurrence and the kind of metamorphic processes in the snow layer, and the melting of snow. By the end of summer, the reflectance of snow from the last winter decreases, but is still larger than the reflectance of other surfaces, as bare glacier ice or surrounding

rocks. Snow on the glacier surface can not only remain from the current year, but also from previous years. Typical properties of multiannual snow, also called firn or névé, are large grains, resulting in lower reflectance compared to new snow. Solid and soluble impurities in the firn layer additionally reduce the reflectance in the visible and near infrared spectral range.
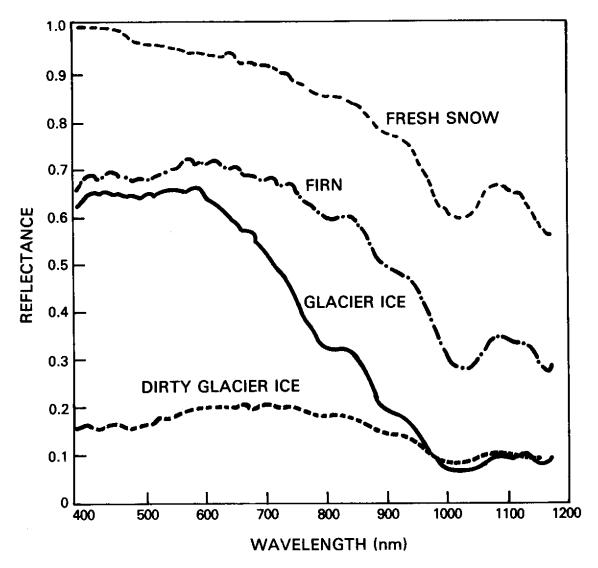
Figure 2.2: Reflectances of different snow and ice surfaces in the visible and near infrared spectral ranges (Hall and Martinec, 1985).

Depending on the solar position, the location and exposition of a glacier, and the location and the geometry of a crevasse, the glacier ice inside a crevasse can have a significantly higher directional reflectance than the glacier ice on the surface (Pfeffer and Bretherton, 1987). Dust or rocks on a glacier's surface can reduce the reflectance significantly. Dust can cover large areas of a glacier's surface and thus reduce the surface reflectance

10

(Takeuchi, 2009). Dark rocks or nunataks warmed by the sun can cause increased melting of the surrounding snow or ice area, and thus lowering the surface reflectance due to melt water on the glacier's surface.

In the shortwave infrared spectral range (1.4 – 3 µm), the reflectance of snow, firn, and glacier ice is significantly lower than in the visible and near infrared spectral range. The Normalized Difference Snow Index (NDSI, cf. Chap. 3.1) uses this property to differentiate snow and ice areas from other surfaces or water clouds.

3. Methods for the retrieval of late summer snow and ice areas (LSSIA) on glaciers

After the overview on the physical and glaciological background in Chapter 2, the focus in this chapter is on the methods to retrieve LSSIA on glaciers in a semi-automated way from optical satellite imagery. Widely used current methods to derive snow and ice areas from optical satellite imagery, and the general principles of the method used for this work are described in Section 3.1. Section 3.2 gives a detailed description of the data base required for the main processing line. Section 3.3 summarizes the radiometric calibration of optical satellite data, followed by correction techniques in Section 3.4 to improve the information derived from an optical satellite image. In Section 3.5, the main processing line for the retrieval of snow and ice areas is described and illustrated in detail.

3.1 Measurement techniques

Hall et al. (1987) established the normalized difference snow index (NDSI) for detecting snow and ice areas from optical satellite data. The reflection by snow and ice covered areas in the visible spectrum (VIS) is high compared to that from other surfaces, but low in the mid-infrared (MIR) spectral range (Wiscombe and Warren, 1980). The NDSI uses these reflectance properties for the discrimination of snow and ice areas from other surfaces.

$$NDSI = \frac{VIS - MIR}{VIS + MIR}$$

This ratio includes also a basic topographic correction. With the NDSI, water clouds and snow can be separated (Riggs et al., 1994), because water clouds have not only a high reflectivity in the visible spectral range, but also in the mid infrared. While the NDSI enables the discrimination of snow and ice areas from other surfaces in an automated way, the differentiation of late summer snow and ice areas is not possible in a straight forward manner due to similar reflectance properties in the NDSI spectral ranges. The same is valid for single band ratios, which are also often used for snow and ice mapping from optical satellite imagery (Racoviteanu et al., 2009).

König (2001) summarized various methods for different satellite sensors to measure properties of snow and glacier ice from remote sensing data, including surface reflectance and temperature properties of snow and ice areas, snow area extent, snow depth and snow water equivalent, glacier velocity, and glacier topography. Additionally, he investigated the reflectance properties of snow and ice in different metamorphic stages.

So far, the investigation of glacier surfaces from optical satellite data was mainly based on manual mapping, or using single band ratios comparable to NDSI. Furthermore, snow

mapping has been done mainly at a relatively small spatial scale, on selected glaciers or icefields, for example by De Angelis et al (2007) or Braun et al (2007).

Another possibility for getting further information about LSSIA is the use of surface albedo (cf. Section 2.1.1). But deriving the total surface albedo from optical satellite data is not trivial, because satellite sensors only work in specific spectral ranges, and thus have to be converted from narrowband to broadband albedo (Knap et al., 1999b). Knap et al. (1999a) compared surface reflectances for specific spectral ranges derived from Landsat imagery with ground-based measured surface albedo, and found differences in both, the narrowband and broadband albedo between 0.01 and 0.2, with largest differences in the ablation area. An additional uncertainty in deriving surface albedo is introduced due to the directional reflectance properties of ice and snow, describing the angular distribution of the reflected radiation in specific directions (Greuell and Oerlemans, 2005).

An atmospheric correction can be applied for the individual spectral bands to correct for radiative processes occurring in the atmosphere and influencing an optical satellite image. The top of atmosphere reflectance of a selected band is corrected by considering the solar geometry, atmospheric conditions during the image acquisition, and the physical properties of the spectral range of the selected band for gases and aerosols in the atmosphere. The radiative transfer model "Second Simulation of a Satellite Signal in the Solar Spectrum" (6S) provides such an atmospheric correction and considers also the bidirectional reflectance functions, describing the reflection from the environment and multiple reflections (cf. Section 3.4.2). This helps getting a better estimate of the real surface reflectances.

To derive glacier surfaces from Landsat imagery, the near infrared band 4, covering the spectral range $0.76 - 0.90$ µm, is the first choice. The Landsat bands $1 - 3$ in the visible spectral range $0.45 - 0.69$ µm are not useful for deriving albedo maps because of frequent saturation of the signal over snow covered areas. Bands 5 and 7, working in the shortwave infrared spectrum at $1.55 - 1.75$ µm and $2.08 - 2.35$ µm, respectively, are not useful because of the very low albedo of snow and ice, and the emitted radiance in band 6 in the thermal infrared ($10.4 - 12.5$ µm) does not enable a clear discrimination of snow and ice surfaces. For other satellite sensors different spectral bands may be used (e.g. in the visible part of the spectrum).

The raw data of a Landsat image have to be radiometrically calibrated to convert the digital numbers into the physical parameter at-satellite radiance in [W m^{-2} sr^{-1} µm^{-1}] and, in a second step, into the top of atmosphere reflectance (cf. Section 3.3). As most of the glaciers investigated in this work are located in mountainous areas, the radiometrically calibrated data are topographically corrected (cf. Section 3.4.1) to reduce topographically induced effects, as for example cast shadows. Therefore, a digital elevation model (DEM) is required. The resulting map is merged with glacier outlines, and reduced to the glacier areas. The LSSIA are retrieved from the topographically corrected top of atmosphere reflectances on the glaciers (cf. Section 3.5).

After vectorization of the snow and ice mask it is possible to map late summer snow lines (LSSL) as proxy for equilibrium lines. For the delineation of the LSSL on a glacier, a clear boundary between snow and ice area is required. Masks of snow and ice contain information also for patchy areas, and are thus used for further investigations in this thesis.
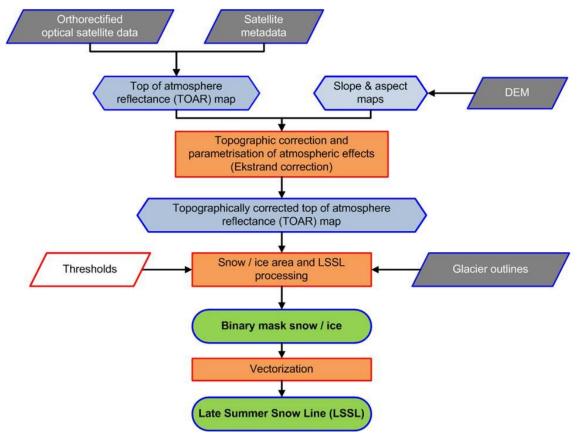
Figure 3.1: Flow line for processing of late summer snow ice area (LSSIA) maps and snow line (LSSL) retrieval.

Figure 3.1 shows an overview on the retrieval flow line of glacier surfaces from optical satellite imagery. Grey boxes are required as minimum input (cf. Section 3.2), blue marked are intermediate products, orange are processing steps (cf. Sections 3.3 - 3.5), and green coloured boxes are the resulting products.

3.2 Required data base

The minimum required data base for the retrieval of LSSIA from optical satellite imagery consists of three parts:

1. Orthorectified optical satellite data, including the associated metadata.

2. A Digital Elevation Model (DEM).

15

3. Glacier outlines meeting the standards of the Global Land Ice Measurements from Space (GLIMS) data base.

Each part of the required data set is described in detail in the following sections.

3.2.1 Optical satellite data

Since the launch of the first satellite "Sputnik 1" of the Soviet Union in 1957 (Jorden, 1957), earth observation by means of remote sensing became an important basis for scientific investigations. Currently, the longest continuous record of scientific satellite data is provided by Landsat series of satellites, with the first Landsat satellite launch in 1972 (Chander et al., 2009a). Two of six satellites are still working: the Landsat 5 with the TM (Thematic Mapper) sensor and the Landsat 7 with the ETM+ (Enhanced Thematic Mapper Plus) sensor. Sensors of both satellites are covering visible and infrared spectral ranges, including near, mid, and thermal infrared. The pixel sizes of the visible, near and mid infrared bands of both satellites are 30 m. The thermal band of Landsat 5 TM has a pixel size of 120 m, and has been improved to 60 m pixel size on Landsat 7 ETM+. Landsat 7 ETM+ additionally has a panchromatic band with higher spatial resolution (15 m). Since January 2009, all Landsat data are available free of charge.

Other high resolution sensors as ASTER (Advance Spaceborne Thermal Emission and Reflection Radiometer) on board of the satellite Terra, the sensors on board of SPOT (Satellite pour l'Observation de la Terre) are working in similar spectral ranges as the Landsat sensors. The sensors of Ikonos or QuickBird cover the visible and near infrared spectral ranges. These sensors have higher spatial resolution (1 m – 30 m), but smaller swath sizes than the Landsat sensors. ASTER scenes are freely available for research activities contributing to the GLIMS (Global Land Ice Measurements from Space) data base. Otherwise, images of high resolution optical sensors are only available for charges.

Table 3.1 gives an overview on some of the currently working optical satellite sensors with high spatial resolution.

For this study, the freely available images of Landsat 5 TM and 7 ETM+ are used as optical satellite image data base. Most Landsat scenes can be searched, selected, and directly downloaded from online servers. If a selected scene is not already downloadable, it can be ordered and will be made available by the U.S. Geological Survey (USGS) a few days later. All original data sets used in this study have been downloaded from the data server of the USGS (http://glovis.usgs.gov).

For mapping of glacier surface and to enable a comparison of snow and ice covered areas in various years, the acquisition date of the satellite imagery is critical. Images taken at the end of summer, as close as possible to the maximum extent of the ablation area are preferred.

Satellite	Sensor	Launch	Pixel size (m)	Revisit (days)	Image size (km x km)
Landsat 5	TM	Mar 1985	30 (MS), 120 (TIR)	16	185 x 172
Landsat 7	ETM+	Apr 1999	30 (MS), 60 (TIR), 15 (Pan)	16	185 x 170
Terra	ASTER	Jul 1999	15 (MS), 30 (SWIR), 90 (TIR)	16	60 x 60
SPOT 4	2 HRVIRs	Mar 1998	10 (MS), 20 (SWIR)	26	60 x 60 (2 times)
SPOT 5	2 HRGs	May 2002	2.5, 5 (Pan), 10 (MS), 20 (SWIR)	26	60 x 60
Ikonos		Sep 1999	1 (Pan), 4 (MS)	3	11.3 x 11.3 (nadir); 13.8 x 13.8 (26° off-nadir)
QuickBird		Oct 2001	0.61 (Pan), 2.44 (MS)	1 – 3.5	16.5 x 16.5

Table 3.1: Selection of currently working satellites with high resolution optical sensors.

If there is no completely cloud free scene, clouds and cloud shadows should be masked before the main processing line starts. A further critical issue for the scene selection are summer snow fall events. Already a layer of summer snow of a few millimetres may be sufficient to hide the extent of accumulation and ablation areas on the glacier surfaces. To avoid such cases, summer time series of optical satellite data should be checked before a scene is selected.

The scenes downloaded from the USGS server are already orthorectified and projected in the UTM (Universal Transverse Mercator) coordinate system, referenced on the WGS84 (World Geodetic System 1984) ellipsoid. There are different levels of the orthorectification. The orthorectification to be used for mapping of glacier surfaces should be L1T (Level 1 Geometrically and Terrain Corrected Landsat product, using ground control points (GCP) and a digital elevation model (DEM) to attain absolute geodetic accuracy), or L1Gt (Level 1 Geometrically and Terrain Corrected Landsat product, using a DEM for topographic accuracy). L1G (Level 1 Geometrically Corrected Landsat data product) data are only referenced on the geoid without any ground control points, and are not suitable for processing due to possible shifts in the geo-locations of up to 300 m. The information on the product type is denoted in the metadata file of each Landsat data set. Level L1G processed scenes either have to be re-orthorectified by manually searching ground control points or should be excluded otherwise.

More information on the product levels of Landsat data are online available at http://edcsns17.cr.usgs.gov/helpdocs/landsat/product_descriptions.html#sys_terrain_etm_l1gt.

The meta information for each satellite scene is important for the image calibration and the scene dependent radiometric correction. One data set includes each band of the sensor as a single file in GeoTIFF format, as well as one file with most meta information, characterized by "MTL", one file with the GCPs (Ground Control Points) used for the orthorectification and/or controlling, denoted by "GCP", and one file with general information, denoted as "README.txt". The MTL file includes information on the image projection, band resolutions, radiometric calibration parameters, and further properties of the scene. For the radiometric calibration of a Landsat band (cf. Section 3.3.1), the information of the associated MTL file is required.

For converting at-satellite radiance [W m-2 sr-1 µm-1] into top of atmosphere reflectance (cf. Section 3.3.2), the accurate acquisition time of a scene is required as additional information. For Landsat sensors, that information is stored in an online archive for each scene in xml format, available at http://landsat.usgs.gov/consumer.php.
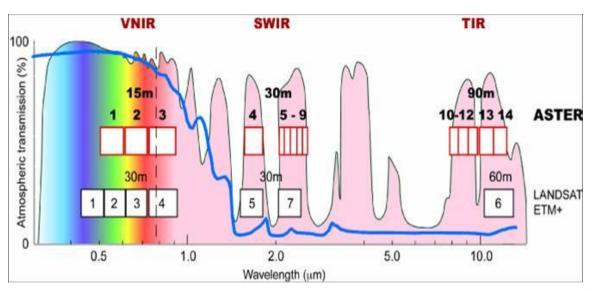
Figure 3.2: Visible and infrared spectrum. Spectral bands and pixel sizes of Landsat 7 ETM+ and ASTER bands are overlaid. From: http://asterweb.jpl.nasa.gov/characteristics.asp.

On 31st May 2003, the Scan Line Corrector (SLC) of the Landsat 7 ETM+ sensor failed. The SLC is required to correct for the forward motion of the Landsat spacecraft, resulting in parallel alignment of all the scans. The failure of the SLC causes striped data gaps between the single scans, with larger gaps on the east and west margin, and less data gaps in the centre of the scene. These data sets are marked as "SLC-OFF" data. Although the SLC-OFF data sets include scene related gap masks, the percentage of missing data is often too large to enable useful investigations in areas covered by the gap stripes.

Also optical imagery of other satellites, as ASTER or SPOT, have to fulfil the upper denoted requirements regarding cloud coverage, acquisition date, and orthorectification. A similar band selection for the retrieval of LSSIA is probable, although the spectral ranges of the bands of other sensors are not identical to these of Landsat (cf. Figure 3.2 and Table 3.2).

Band	Landsat 4/5 TM [μm]	Landsat 7 ETM+ [μm]	ASTER [μm]
1	0.45 – 0.52	0.45 – 0.515	0.52 – 0.60 N
2	0.52 – 0.60	0.525 – 0.605	0.63 – 0.69 N
3	0.63 – 0.69	0.63 – 0.69	0.78 – 0.86 N / B
4	0.76 – 0.90	0.78 – 0.90	1.60 – 1.70
5	1.55 – 1.75	1.55 – 1.75	2.145 – 2.185
6	10.40 – 12.50	10.40 – 12.50	2.185 – 2.225
7	2.08 – 2.35	2.09 – 2.35	2.235 – 2.285
8	---	0.52 – 0.90	2.295 – 2.365
9	---	---	2.360 – 2.430
10	---	---	8.125 – 11.65
11	---	---	8.475 – 8.825
12	---	---	8.925 – 9.275
13	---	---	10.25 – 10.95
14	---	---	10.95 – 11.65

Table 3.2: Spectral ranges of Landsat 4/5 TM, Landsat 7 ETM+, and ASTER bands. After showing anomalies since April 2007, the ASTER bands working in the Short Wave Infrared (bands 4 – 9: 1.60 μm – 2.430 μm) finally failed in April 2008. Abbreviations: N = Nadir looking. N / B = Nadir and Backward looking.

3.2.2 Digital Elevation Model (DEM)

Additionally to an optical satellite image meeting the previously described requirements, a digital elevation model (DEM) is required for the main processing line to retrieve LSSIA from optical satellite data. The projection of the DEM has to be identical to that of the optical satellite image for the processing line. In case of Landsat data, that means a UTM WGS84 projection. The pixel size of the DEM should be ideally at least equal to the pixel size of the optical satellite image. In case of Landsat imagery, this condition is only fulfilled by high resolution national DEMs or the Global ASTER DEM (ASTER GDEM), released on June 29, 2009.

National DEMs usually have a high quality standard and often have a very high resolution, but are often only available for charges. Nevertheless, if a national high resolution DEM is available, it is always the first choice for the processing line. If the national DEM covers only a part of the optical satellite image, the remaining area can be filled with data from another DEM.

The projection and the pixel size of the DEM are often different from the required UTM WGS84 projection of the Landsat imagery. In this case, the DEM has to be reprojected and resampled to fit the geometric conditions of the Landsat scene.

The quality of the ASTER GDEM varies from region to region due to clouds on ASTER scenes used for producing the GDEM. Unfortunately, so far it is not possible to get information on the quality of single ASTER GDEM tiles, because there is no available documentation on the data base used for processing the DEM tiles. So, ASTER GDEM has to be downloaded, extracted and individually reviewed regarding quality. Thus, although the ASTER GDEM offers a large spatial coverage, between 83°N and 83°S, and has relatively high resolution with 30 m grid size, it is only used for the standard processing line after a visual quality check.

If ASTER GDEM shows clear mistakes, the DEM derived from the Shuttle Radar Topography Mission (SRTM) can be used alternatively. In between, the fourth version of the SRTM DEM is available (Jarvis et al., 2008). The DEM of SRTM has only 90 m grid size on equator, but has consistent quality for the whole covered area, extending from 60°N to 60°S. Due to the relatively coarse resolution, especially steep slopes and peaks are smoothed and flattened in the DEM of SRTM. The effect of the coarse resolution of the DEM compared to the grid size of the optical satellite imagery can be partly observed after the topographic correction on the top of atmosphere reflectance map of the processed band.

A fully global DEM is the GETASSE30 DEM of the ESA (European Space Agency), which is based on Altimeter Corrected Elevations (ACE). With a pixel size of 1 km it is only useful for large and flat icecaps, as for example Flade Isblink in Greenland. In these cases, the GETASSE30 DEM has often a higher quality than the ASTER GDEM, and is thus often used outside the coverage of the DEM of SRTM. Nevertheless, for correcting small scaled topographic effects, as often occur in steep mountainous terrain, or small scaled glaciers, a DEM with smaller pixel size is preferred.

For Alaska and USA, the U.S. Geological Survey provides a DEM with 60 m pixel size. As it shows high quality in these areas, it is used for all investigations in Alaska. For selected small regions, the SPIRIT DEM (Korona et al., 2009) is available. For Flade Isblink, Greenland, an INSAR DEM, covering most of the icecap, is alternatively available to the GETASSE30 and the VIEWFINDER DEM.

Another data base storing DEMs derived from SRTM, geographical maps, and ASTER GDEM for selected regions is online available at http://www.viewfinder.org/dem.html.

DEMs of this webpage have been used mainly for glaciers in the Himalaya, as these DEMs show a better, or in the worst case, the same quality as the DEM of SRTM. Table 3.3 gives an overview on all DEMs used in this study.

DEM	Grid size	Coverage	Tile size
National DEM	< 30 m (depends on region)	regional	--
ASTER GDEM	30 m	83°N – 83°S	1° x 1°
USGS DEM	10 m – 60 m	USA, Alaska	1° x 1°
SRTM	90 m	60°N – 60°S	5° x 5°
VIEWFINDER DEM	30 m – 90 m	regional	1° x 1°
GETASSE30 DEM	1000 m	90°N – 90°S	15° x 15°
SPIRIT DEM	40 m	regional	--

Table 3.3: Comparison of pixel size, spatial coverage, and tile size of the digital elevation models used for the main processing line for the retrieval of glacier surfaces.

3.2.3 Glacier outlines

Glacier outlines are not only required to determine the relevant areas, and to set the resulting snow areas in relation to the total area of individual glaciers. The continuously growing GLIMS data base (http://www.glims.org) provides glacier outlines and related information for currently more than 120'000 glaciers worldwide. Information about each glacier, as well as information about the analysis and the analyst is stored in the associated attribute table. In this table also information on snow and ice area extent, as well as elevation information of these areas can be added. Detailed tutorials and guidelines how to meet the GLIMS standards have been published for example by Raup and Khalsa (2007), Paul et al. (2010), and Rau et al. (2005).

During the ESA funded GlobGlacier project, glacier outlines are mapped for regions in Alaska, Greenland, Baffin Island, Himalaya, Karakoram, Norway, and the European Alps. Some of these new inventories are already available via the GLIMS data base, and the remaining will be made available during the next months. The glacier outlines of this project are used as input in several selected study regions for the main processing line.

For the region Ötztal Alps in Austria, glacier outlines of 1997 are kindly made available by members of the Institute of Meteorology and Geophysics at the University of Innsbruck, Austria. Meanwhile, the glacier inventory of this region for the years 1969, 1997 and 2006, projected in the national coordinate system MGI 28 (MilitärGeographisches Institut Zone M28, geodetic date of Austria) on the ellipsoid Hermannskogel, is freely available on the homepage of the institute (http://imgi.uibk.ac.at/iceclim/glacierinventory).

The glacier outlines of the Sagarmatha Basin in Nepal used in this study have been mapped by members of the International Centre for Integrated Mountain Development (ICIMOD). The data are freely available after registration on the Mountain Geo Portal of ICIMOD (http://geoportal.icimod.org/Downloads/Download.aspx?ID=19).

3.3 Radiometric calibration of optical satellite data

Raw satellite image data are provided in digital numbers (DN). To convert the raw data of a satellite image to physical values, a band specific radiometric calibration is required. Several satellite data providers already offer different stages of calibrated products, as for example at-satellite radiance [W/(m² sr µm)] or brightness temperature [K] produced by the ASTER science team (http://asterweb.jpl.nasa.gov/data_products.asp). If the downloaded optical satellite imagery is not pre-processed, as for example usual for Landsat data, the associated calibration constants for each scene and each band are included in the provided data set. Chander et al. (2009) summarized the calibration equations and constants for the Landsat and the EO-1 ALI (Earth Observer-1 Advanced Land Imager) sensors. Relevant information about satellite systems, radiometric calibration, and further satellite related information is also available in online user guides, as for example on the Landsat homepage (http://landsathandbook.gsfc.nasa.gov/handbook/handbook_toc.html).

In the following two sections, the conversion of DN to Top of Atmosphere Radiance (TOAR) is shown on the example of Landsat data. General forms of conversion equations are also valid for other optical sensors.

3.3.1 At-satellite radiance

Raw Landsat data processed with the software Level 1 Product Generation System (LPGS) are provided in DN scaled between 1 and 254, using additionally values 0 and 255 for marking gaps and saturation, respectively. Before April 2004, the National Land Archive Production System (NLAPS) was used for the processing of Landsat imagery. This software scaled the DN between 0 and 254, but used the value 0 not only for the lowest radiance in the scene, but also to mark data gaps. On 5th April 2004, this difference was removed, reserving the DN value 0 for marking and filling gaps, and the DN value 255 for saturation. The correct use of the minimum and maximum DN is essential for the radiometric calibration.

The differences between LPGS and NLAPS software are described in detail on the Landsat homepage (https://landsat.usgs.gov/products_IP_LPGSvsNLAPS.php). After correctly converting the raw data to at-satellite radiance, the differences in the scaling are removed (Scaramuzza, 2002).

Based on the information stored in the metadata file (cf. Section 3.2.1), the digital numbers of an optical satellite image can be converted to the physical parameter at-satellite radiance [W/(m² sr µm)]. This conversion is described by the general equation:

$$L(\lambda) = G * Q_{cal} + B$$

L(λ)   spectral radiance at the sensor's aperture [W/(m² sr µm)]

G   rescaled gain [W/(m² sr µm)/DN]

Q_{cal} quantized calibrated pixel value [DN]

B   rescaled bias [W/(m² sr µm)]

In the case of Landsat data, this equation can also be written as:

$$L(\lambda) = [\frac{Q_{calmax} - Q_{calmin}}{L_{max}(\lambda) - L_{min}(\lambda)}] * Q_{cal} + L_{min}(\lambda)$$

with $$G = \frac{Q_{calmax} - Q_{calmin}}{L_{max}(\lambda) - L_{min}(\lambda)}$$

and $$B = L_{min}(\lambda)$$

L(λ)   spectral radiance at the sensor's aperture in [W/(m² sr µm)]

Lmax(λ)   spectral radiance that is scaled to Qcalmax in [W/(m² sr µm)]

Lmin(λ)   spectral radiance that is scaled to Qcalmin in [W/(m² sr µm)]

Qcal   quantized calibrated pixel value in DN

Qcalmax   maximum quantized calibrated pixel value (corresponding to Lmax(λ)) in DN [= 255]

Qcalmin   minimum quantized calibrated pixel value (corresponding to Lmin(λ)) in DN [= 1 (LPGS Products); = 0 (NLAPS Products)]

3.3.2 Top of atmosphere reflectance

Based on the resulting physical parameter at-satellite radiance in [W / (m² sr µm)], the top of atmosphere reflectance can be calculated in a second step. Therefore, the earth-sun distance in Astronomical Units (AU) for the image acquisition date and time, the geographic location of the scene, the solar zenith angle and the solar constant for a specific spectral range [W/(m² µm)] are required. The earth-sun distance can either be

calculated, for example by the software "SOLPOS2.0", (online available at: http://rredc.nrel.gov/solar/codesandalgorithms/solpos/), or be derived from an online available Excel file (http://landsathandbook.gsfc.nasa.gov/handbook/excel_files/d.xls). The solar constant for a specific spectral range can be derived from the metadata file. Table 3.4 summarizes the solar spectral irradiances [W/(m²µm)] at top of atmosphere for the Landsat TM and ETM+ sensors.

Band	Spectral range [µm]	Landsat 4 TM (NLAPS & LPGS)	Landsat 5 TM	Landsat 7 ETM+
1	0.45 – 0.52	1983.000	1983.000	1969.000
2	0.52 – 0.60	1795.000	1796.000	1840.000
3	0.63 – 0.69	1539.000	1536.000	1551.000
4	0.76 – 0.90	1028.000	1031.000	1044.000
5	1.55 – 1.75	219.800	220.000	225.700
7	2.08 – 2.35	83.49	83.44	82.07
8	0.52 – 0.90	--	--	1368.000

Table 3.4: Solar spectral irradiances [W/(m²µm)] at top of atmosphere for Landsat sensors.

The conversion from at-satellite radiance [W/(m² sr µm)] to top of atmosphere reflectance is calculated by the following equation:

$$\rho(\lambda) = \frac{L(\lambda) * \pi * d^2}{E_{sun}(\lambda) * \cos(\Theta_s)}$$

$\rho(\lambda)$ Spectral top of atmosphere reflectance

$L(\lambda)$ Spectral radiance at the sensor's aperture [W/(m² sr µm)]

d Earth-sun distance in astronomical units [AU]

$E_{sun}(\lambda)$ Solar constant for a specific wave length range [W/(m² µm)]

Θ_s Solar zenith angle [rad]

The resulting map will be used for all further processing steps.

3.4 Correction techniques for optical satellite data

3.4.1 Radiometric normalization of terrain illumination effects

The resulting top of atmosphere reflectance (TOAR) map is still affected by atmospherically and, especially in mountainous terrain, by topographically induced effects. While large parts of investigated glaciers are located in mountainous terrain and thus are affected by topography, a topographic correction should be applied to reduce or even remove these effects (Teillet et al., 1982). Several methods to correct for topographic effects have been developed, tested and documented during the last years.

Teillet et al. (1982) introduced the Cosine correction, which is based on the ratio of cosines of sun zenith angle and illumination angle in relation to the normal on a pixel. Statistical methods have been presented inter alia by Meyer et al. (1993) and Ziegler et al. (2006). But their results significantly varied depending on the selected scene.

Applying semi-empirical methods for the topographic correction on different optical satellite imagery proved to be more successful. The C-factor correction, which has been also introduced by Teillet et al. (1982), is based on the cosine correction, but adds a factor C to each term of the ratio.

Therefore, the original data is brought into the form of a linear equation:

$$L_t \; = \; m * \cos(i) + b$$

The C factor is defined as the quotient of intercept b and the inclination m of the regression line of the original digital numbers on the ordinate and the cosine of the illumination angle, cos(i), on the abscissa. The C-Factor can be derived empirically.

A further semi-empirical correction method is denoted after Minnaert. Minnaert (1941) originally investigated the lunar light and extended therefore the cosine correction by introducing a factor k, now known as Minnaert constant. This constant factor also includes a rudimentary parameterization of atmospheric effects. Based on Minnaert's correction method, Ekstrand (1996) developed a topographic correction method by weighting the Minnaert constant with the cosine of the illumination angle.

All these methods have been tested and compared by several authors, e.g. Meyer et al. (1993), McDonald et al. (2000), Ziegler et al. (2006) and Gao and Zhang (2009). While the plain cosine correction has been clearly excluded from the list of useful topographic correction methods by all authors, the results of the other methods were quite different. Although all tests have been done with scenes of mountainous, forested areas, the performance of a method seems to depend on individual topography and illumination conditions. So far, there is no preferred method for the topographic correction (Richter et al., 2009).

While most of these tests for topographic correction methods have been done for forested areas, the application of the topographic correction for this study is required for glaciated

areas and surroundings. Thus, the following four methods for topographic correction have been tested and compared to each other also in this study:

- Cosine correction: $L_h = L_t * \dfrac{\cos(\theta_s)}{\cos(i)}$

- C-factor correction: $L_h = L_t * \dfrac{\cos(\theta_s)+C}{\cos(i)+C}$

- Minnaert correction: $L_h = L_t * \left(\dfrac{\cos(\theta_s)}{\cos(i)}\right)^k$

- Ekstrand correction: $L_h = L_t * \left(\dfrac{\cos(\theta_s)}{\cos(i)}\right)^{k*\cos(i)}$

L_t	radiance on an inclined surface
L_h	equivalent radiance on a horizontal surface
θ_s	solar zenith angle
i	solar illumination angle in relation to a normal on a pixel
$C = \dfrac{b}{m}$	C-factor for modelling diffuse sky radiation:
b	intercept of regression line of original digital numbers and cos(i)
m	inclination of regression line of original digital numbers and cos(i)
k	Minnaert constant $(0.0 < k < 1.0)$

On the top of atmosphere reflectance, one of these topographic correction methods is applied to obtain the topographically corrected reflectance. The solar illumination angle is calculated for each pixel by using slope and aspect maps derived from the digital elevation model (DEM).

As already mentioned, the cosine correction is based on the simple ratio of the solar zenith angle and the incidence angle. While only direct illumination is considered, the results of this correction methods show significant differences compared to the true surface reflectance because atmospheric effects, as for example diffuse radiance, are neglected.

The other three correction methods account for differences in the atmospheric irradiance by means of empirical factors that are related to changes of the direct/diffuse irradiance and implicitly also for deviations of the surface from the Lambertian (ideally diffuse) reflection behaviour.
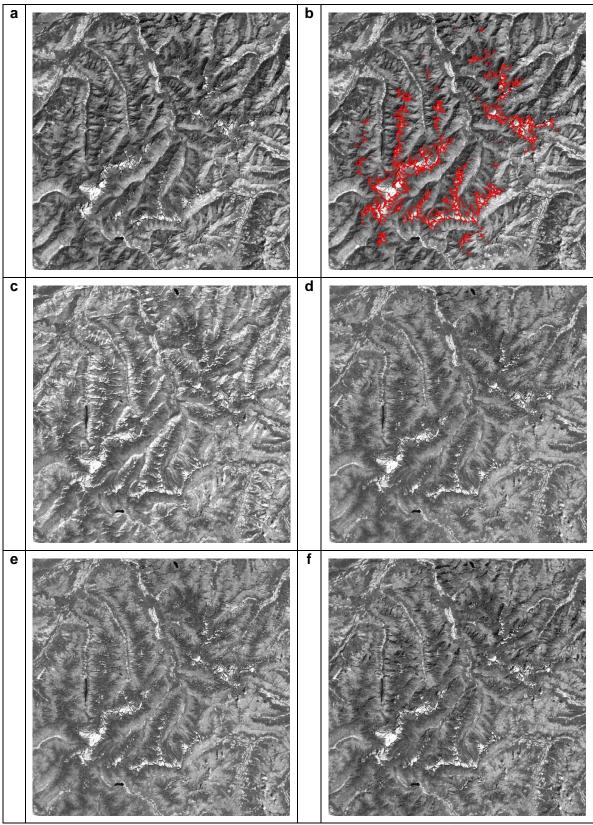
Table 3.5: Subset of the Landsat 5 TM TOAR band 4, showing the Ötztal and the Stubai Alps, Austria, taken on 31 August 2009, 09:53:29 UTC, and processed with national DEM with 10 m pixel size. a) uncorrected scene; b) uncorrected scene with glacier outlines; c) cosine corrected scene; d) C-factor corrected scene; e) Minnaert corrected scene; f) Ekstrand corrected scene.

The Minnaert constant is a measure for the Lambertian surface conditions and also a function of the phase angle (Teillet et al., 1982). It can be empirically derived by linearizing the correction equation logarithmically and calculating the slope of the regression. The Minnaert factor k varies between 0 and 1, with k=1 describing a Lambertian surface.

The C-factor can also be determined empirically by the assumption that the original data can be considered in the form of a regression line with the Digital Numbers on the ordinate and the cosine of the illumination angle, cos(i), on the abscissa. The correction factor C can now be calculated by the ratio of the intercept and the inclination of the regression line. Both constants, k and C, are applied as extensions on the cosine correction equation. The C-factor is used as additive term, while the Minnaert constant weights the equation as a power factor. The Ekstrand correction (Ekstrand, 1996) is based on the Minnaert correction, but weights the Minnaert constant with the cosine of the solar incidence angle.

The images in Table 3.5 compare the uncorrected top of atmosphere reflectance of band 4 and the topographically corrected TOAR maps of band 4 after applying cosine, C-factor, Minnaert, and Ekstrand correction, respectively.

The graphics in Table 3.6 show the differences between the uncorrected top of atmosphere reflectance of a Landsat 7 ETM+ band 4 and the tested topographic corrections of this band on a subset of a scene of the Ötztal Alps, Austria/Italy, acquired on 10th September 2004. The dark stripes on the right scene margin are data gaps due to the failure of the Scan Line Corrector on board of Landsat 7 ETM+ in end of May 2003. Black pixels within the scene indicate the saturation of the signal, occurring on snow covered areas.

The smallest difference range is found for the Ekstrand corrected scene, while the largest differences, up to 0.77, are derived for the cosine corrected scene.

After testing all methods, it was obvious that the Cosine correction is not useful for the topographic correction in mountainous terrain due to overcorrection resulting in a bias of the reflectance in dependence of the local incidence angle. Also the C-Factor correction overcorrects some smaller parts of the selected test scenes. The Minnaert correction is a suitable method for large areas, but especially in steep terrain the Ekstrand correction provided the best results. This is also in line with results reported in the literature, for example by Törma and Härmä (2003) or Law and Nichol (2004).

Although the Ekstrand correction has been mainly used for the investigation of forested areas so far, tests show also good results in mixed terrain, especially in steep mountainous terrain. Thus, the Ekstrand correction is used as standard method for the topographic correction. Not only the kind of topographic correction, but also the resolution of the DEM used as basis for the topographic correction is critical for the quality of the resulting maps showing the glacier surfaces.
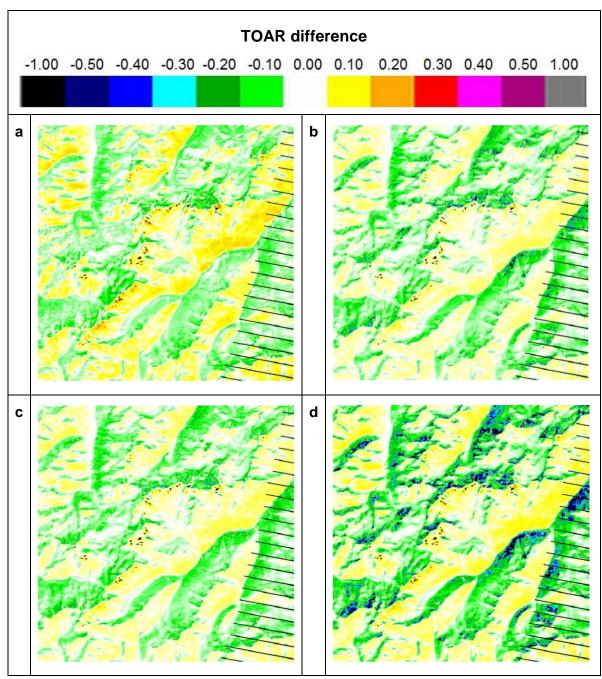
Table 3.6: Differences of topographically corrected top of atmosphere reflectances of Landsat 7 ETM+ band 4 to the uncorrected TOAR of the band, shown on a subset of a Landsat 7 ETM+ scene of Ötztal Alps, Austria, of 2004-09-10. a) difference between the uncorrected top of atmosphere reflectance of band 4 (TOAR4) and the Ekstrand corrected TOAR4; b) difference between the uncorrected TOAR4 and the Minnaert corrected TOAR4; c) difference between the uncorrected TOAR4 and the C-Factor corrected TOAR4; d) difference between the uncorrected TOAR4 and the Cosine corrected TOAR4.

3.4.2 Atmospheric propagation

To correct for atmospheric effects a radiative transfer (RT) model can be applied on the individual bands of the optical satellite imagery. Such a model, the 6S (Second Simulation of a Satellite Signal in the Solar Spectrum), has been developed by Kotchenova et al. (2006b). Kotchenova et al. (2006) and Kotchenova and Vermote (2007) tested the 6S model against other RT models, as a Monte Carlo code, MODTRAN (MODerate resolution atmospheric TRANsmission), and SHARM (Spherical HARMonics), and found good agreements. Originally developed for the application on MODIS (Moderate Resolution Imaging Spectroradiometer) data, the 6S model has also been established for the correction of other optical sensors, including inter alia Landsat TM and ETM+ sensors. The 6S code is not only very well documented, but also freely available, and can be downloaded from http://6s.ltdri.org/index.html.

The 6S model requires not only information on the used satellite sensor, but, and this is the more difficult part, also some knowledge on the atmospheric conditions at the point of interest at the time of the satellite image acquisition. The required parameters of the optical satellite sensor are already predefined for the most common satellites and sensors, and can easily be selected from a list. It is also possible to select user defined conditions for a satellite and/or a sensor. The geographic location of the point of interest has to be specified in geographical coordinates (latitude/longitude). The elevation of the point of interest can be defined manually or derived from a digital elevation model. Several atmospheric models are predefined for locations worldwide to consider aerosol concentration or visibility, respectively, and atmospheric layering defined by temperature (T), ground pressure (p) and relative humidity (rH). A first guess of the surface albedo is required. This first guess can be defined as a global value, when the point of interest is representative for a surface extending over a large area, or as a local value, when various surfaces with different surface albedo are located in the surroundings of the point of interest.

Based on these input data, the 6S model calculates several parameters, of which only selected parameters are necessary for the atmospheric correction (cf. Figure 3.3) the location for the correction must be defined by latitude, longitude and ground altitude or alternatively the atmospheric parameter ground pressure. Contributions to the irradiance at the ground in [W/(m² µm)] and of the radiance at the satellite in [W/(m² sr µm)] are important components for the atmospheric correction.

Nevertheless, the atmospheric correction requires some knowledge on the atmospheric conditions of the area of interest at the time of the satellite image acquisition. Such information, required as model input, is often not available for remote, glaciated areas, as most of the areas of interest in this work are. Thus, for this study, the atmospheric correction is only shown for the example of the Ötztal Alps in Austria, where some of the required input data are available from a meteorological station.
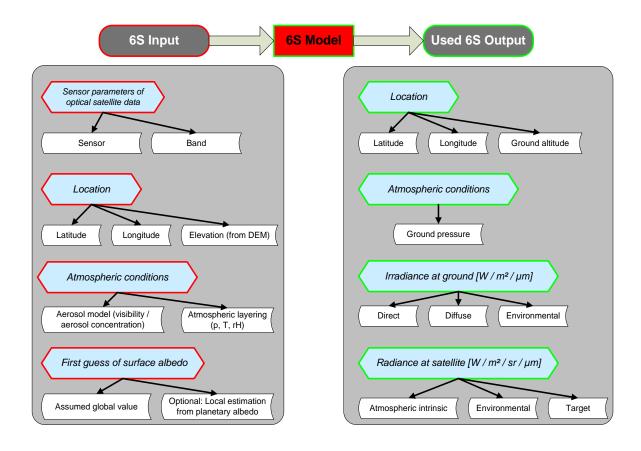
Figure 3.3: Overview on the required input and the used output information of the radiative transfer model 6S.

3.4.3 Comparison of correction techniques

The southern part of the Ötztal valley in the Austrian Alps was selected for testing the correction methods for the normalization of terrain illumination effects, and the radiative transfer model 6S, as meteorological data are available from the weather station Obergurgl (cf. Section 4.1) in this region.

Ground elevations of the test site range between about 800 m a.s.l. and about 3800 m a.s.l., indicating low temperatures in winter, and rather low to moderate temperatures in summer.

The valleys in this region are rather arid compared to other regions in the European Alps. In order to find the best match of the atmospheric conditions with a predefined atmospheric model (Kotchenova et al., 2006a), two models were tested for this test site: the mid-latitude summer (cf. Figure 3.4), and the sub-arctic summer (cf. Figure 3.5). The climatological conditions of the test site indicate that the pre-defined atmospheric model "sub-arctic summer" characterized by lower temperature and less humidity at the ground, better matches the local atmospheric conditions than the model "mid-latitude summer".
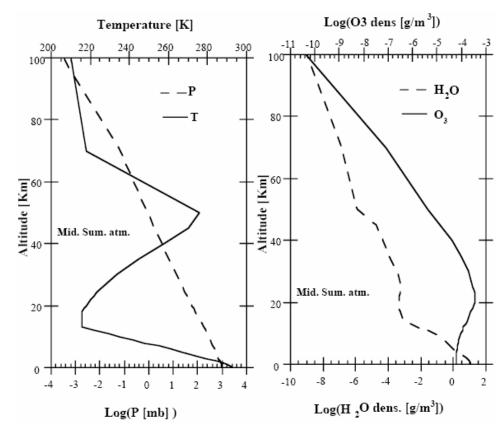
Figure 3.4: Atmospheric layering of the predefined model "mid-latitude summer" (atm2), after McClatchey et al. (1971).
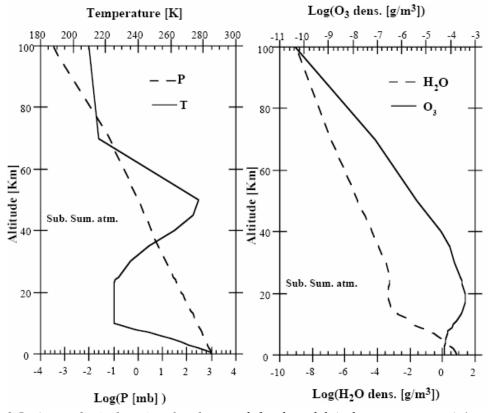
Figure 3.5: Atmospheric layering for the pre-defined model 'sub-arctic summer' (atm4), after McClatchey et al. (1971).
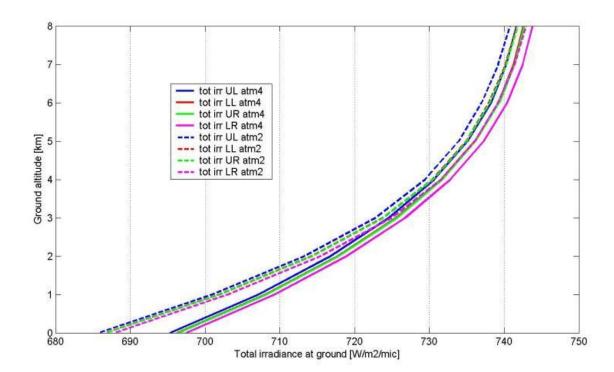
Figure 3.6: Total irradiance at ground [W/(m² μm)], calculated for the corner coordinates (UL: upper left; LL: lower left; UR: upper right; LR: lower right) of the subset covering the Ötztal Alps (cf. Section 3.4.1) using two different atmospheric models for the atmospheric parameterization: mid-latitude summer (dashed lines), and sub-arctic summer (solid lines). To investigate the dependence of the irradiance at ground on the target elevation, the model was executed using target elevations ranging from sea level (0 km) to almost the top of atmosphere (8 km).

In Figure 3.6 and Figure 3.7, the total irradiance at the ground, and the individual components of the irradiance, the direct, diffuse, and environmental irradiances, for the NIR Landsat 7 ETM+ band 4 derived for both atmospheric models are shown for different elevations. All calculations are done for each corner coordinate of the total Landsat 7 ETM+ scene of 2004-09-10 (Path 193 / Row 027). The abbreviations "atm2" and "atm4" refer to the predefined atmospheric model numbering required for the 6S input.

Spatial variations between the corner coordinates of the Landsat scene, extending over about 180 km, are negligible at all components of the irradiance and for both atmospheric models. Above 2 km ground elevation, the outputs of both atmospheric models merge. The largest difference between the sub-Arctic summer and the mid-latitude summer model, about 10 W/(m² μm), occurs in the direct irradiance close to the sea level. Variations in the diffuse and the environmental irradiance due to different atmospheric models are less than 1.5 W/(m² μm) over all elevations, and are thus negligible.
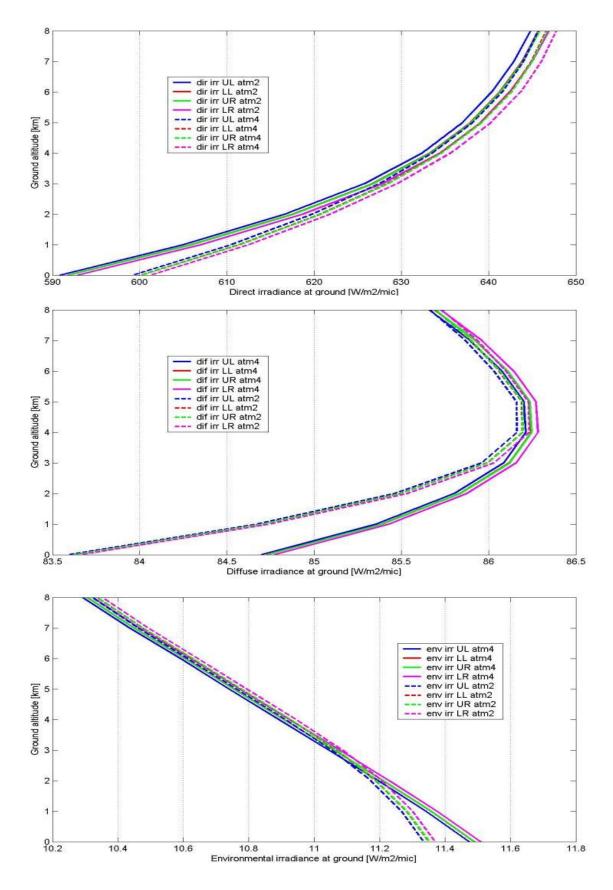
Figure 3.7: Direct, diffuse, and environmental irradiance [W/(m² µm)] derived for two atmospheric models for the test site Ötztal, Austria, in dependence of the target elevation.

For a subset of the used Landsat 7 ETM+ scene of 2004-09-10 showing the test area Ötztal, the resulting atmospherically corrected top of atmosphere reflectance of the near infrared band is compared to the maps derived by the topographic corrections of the methods described in Section 3.4.1.

Subtracting the atmospherically corrected top of atmosphere reflectance map from the uncorrected TOAR map of the Landsat 7 ETM+ band 4 (TOAR4) results in differences ranging between -0.20 and 0.20. Higher uncorrected TOAR4 values occur often on north orientated areas, while on south orientated slopes the atmospherically corrected TOAR4 values are often higher. The largest differences are found close to mountain ridges, often on accumulation areas of glaciers, on north and northwest, as well as on south and southeast orientated slopes. Also non-glaciated, but steep slopes with these aspects show partly high differences.

The difference map derived from subtracting the Ekstrand corrected TOAR4 map from the raw TAOR4 map shows another distribution, and higher differences up to almost 0.30. The most positive differences occur on south and southeast orientated slopes, meaning that the uncorrected TOAR4 map has higher values in these regions compared to the Ekstrand corrected TOAR4 map. On the other side, the most negative differences are found on north and northwest orientated slopes.

Subtracting the Ekstrand corrected TOAR4 map from the atmospherically corrected TOAR4 map enhances the differences derived from subtract the Ekstrand corrected TOAR4 from the uncorrected TOAR4 map, especially in south and southeast orientated regions with already high differences. The difference maps derived for the Minnaert corrected and the C-Factor corrected TOAR4 map subtracted from the atmospherically corrected TOAR4 map show large differences in north and northwest orientated slopes, with difference values up to 0.50. On south and southeast orientated slopes the differences are lower in both cases, with values up to 0.30. The cosine corrected TOAR4 map shows the large differences to the atmospherically corrected TOAR4 map, with difference values up to almost 1.0 on north and northwest orientated slopes and also in flat terrain, and values up to 0.30 on south and southeast orientated slopes. This is also in line with the results for the cosine correction described in Section 3.4.1, and enhances the statement that the Cosine correction is unsuited for the normalization of terrain induced illumination effects.

All described difference maps calculated for the near infrared band of Landsat, which is also used for the further investigations, are shown in Table 3.7.
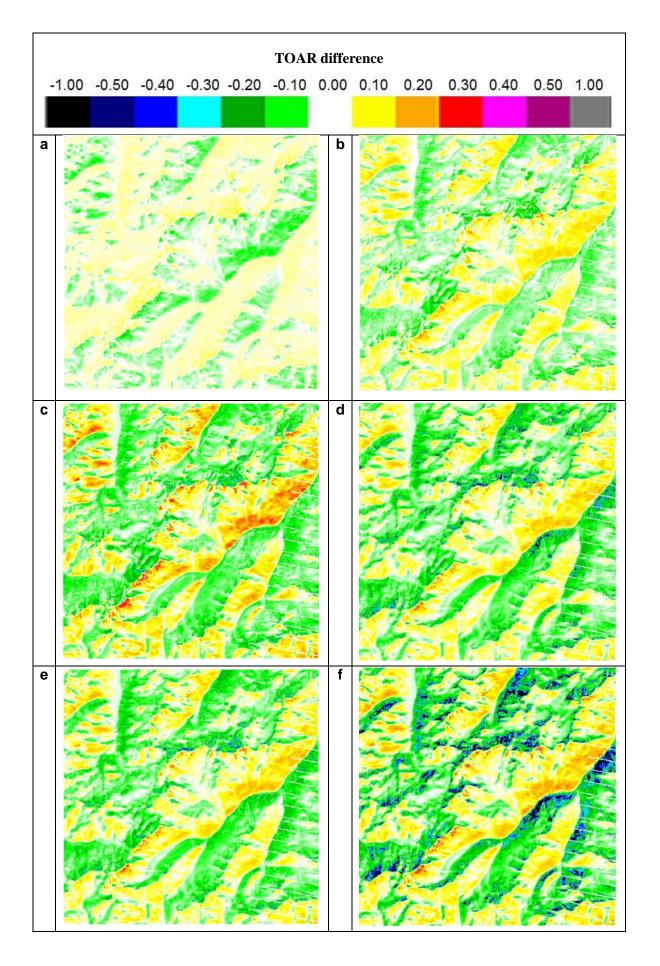
Table 3.7: Differences of the atmospherically corrected top of atmosphere reflectance of band 4 (TOAR4) by 6S and the parametric topographically corrected TOAR4 of a subset of a Landsat 7 ETM+ scene of 2004-09-10 showing the Ötztal Alps, Austria. a) difference map between the raw TOAR4 and the atmospherically corrected TOAR4 using the 6S model; b) difference map between the raw TOAR4 and the topographically corrected TOAR based on the Ekstrand method; c) difference map between the atmospherically corrected TOAR 4 using the 6S model and the topographically corrected TOAR4 using the Ekstrand method; d) difference map between the atmospherically corrected TOAR 4 using the 6S model and the topographically corrected TOAR4 using the Minnaert method; e) difference map between the atmospherically corrected TOAR 4 using the 6S model and the topographically corrected TOAR4, using the C-Factor correction; f) difference map between the atmospherically corrected TOAR 4 using the 6S model and the topographically corrected TOAR4, using the Cosine correction.

3.5 Retrieval of late summer snow and ice areas

Based on the topographically corrected TOAR of the NIR Landsat band 4 on the glaciers, late summer snow and ice areas (LSSIA) on the glaciers are derived by applying a threshold, resulting in a binary snow mask. The following illustrations of the retrieval of LSSIA are based on a Landsat 5 TM image of 12 September 2006, showing the Harding Icefield, Alaska. In a first step, the image data of the Ekstrand corrected TOAR map are superimposed by the glacier outlines (Figure 3.8).

This step not only reduces the computational effort, but also enables the retrieval of a histogram of the topographically corrected TOAR on the glaciers (cf. Figure 3.9). For the creation of the histograms, the topographically corrected TOAR is rescaled by a factor 100 to retrieve integer values instead of floating numbers. In the illustrated histograms in this section, the values of the topographically corrected TOAR on the x-axis are numbered by default in tens. But in the further related descriptions and discussions, the originally scaled topographically corrected TOAR values (0.00 – 1.00) are used.

Based on the histogram, a threshold is selected to define the snow areas on the glaciers. This threshold can vary not only in space but also in time and thus has to be selected individually for each scene.
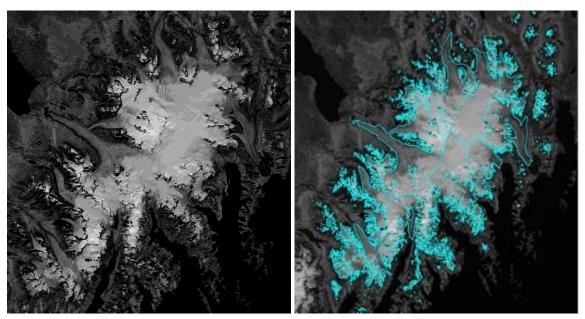
Figure 3.8: Left: Ekstrand corrected TOAR of Landsat 5 TM band 4. Right: Topographically corrected TOAR map combined with glacier outlines, mapped by members of the Geographical Institute, University of Zurich, Switzerland, and now publicly available on the GLIMS data base.

The threshold is selected via a stepwise approximation followed by a cross-check with the auxiliary maps. In the beginning, a large range of possible thresholds, e.g. $0.20 - 0.80$, is selected. Within this range, temporary snow maps are calculated varying the applied threshold in steps of 0.05
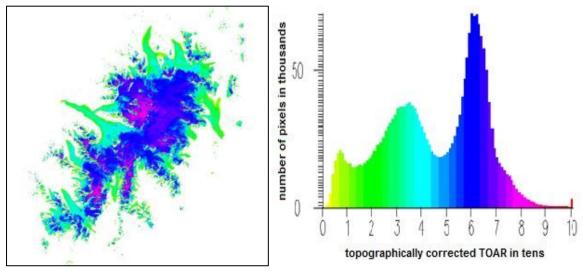
Figure 3.9: Image section with the topographically corrected TOAR map on the glaciers, and the associated histogram derived for the subset of the Landsat 5 TM scene of 12/09/2006 of the Harding Icefield, Alaska.

The resulting snow maps are vectorized, and the resulting vectorized outlines of the snow areas are compared with the histogram, the uncorrected and the topographically corrected top of atmosphere reflectance map of Landsat band 4, different RGB composites, as for example Landsat 543, or 321, and in critical cases also with the related DEM, slope and aspect map. . The under- and overestimation of the snow areas derived from applying too low or too high thresholds are illustrated in Figure 3.10.
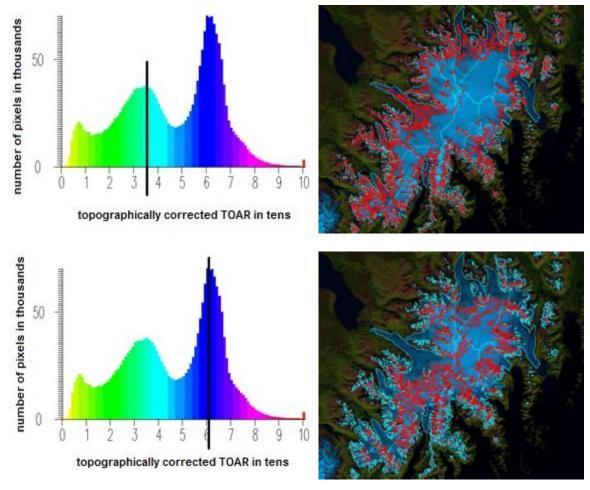
Figure 3.10: Threshold approximation and visual comparison of resulting boundaries of late summer snow areas with the RGB 543 composite of Landsat 5 TM. Upper image pair: threshold too low resulting in an overestimation of the late summer snow areas. Lower image pair: threshold too high resulting in an underestimation of the late summer snow areas.

Thus, the range of possible thresholds is reduced to $10 - 15$ values. Within this new range, the snow map is created for each threshold using an interval of 0.01 as step size. The previously described comparison is repeated for each temporary snow map, until the best fit is found. The finally selected threshold is that value of the topographically corrected TOAR of band 4 yielding the best match of the snow areas compared to the auxiliary maps (cf. Figure 3.11 and Figure 3.12).
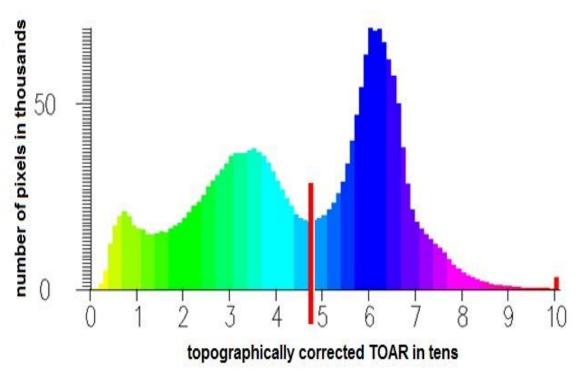
Figure 3.11: Finally selected threshold for the mapping of late summer snow areas on the glaciers.

The resulting late summer snow areas are set into relation to the total glacier area to derive the late summer snow area ratio (LSSAR). If the LSSAR is derived for a region in a multi-annual scale, and set into a relation to a mean LSSAR, the individual LSSARs can be used as a measure of annual sensitivity.

The LSSAR derived from the late summer snow/glacier area extent can also be used as proxy for the accumulation area ratio (AAR) of individual glaciers or for whole glaciated regions. According to the relation between the AAR and the net balance of a glacier introduced by Dyurgerov (1996), the LSSAR can be used to approximate the net mass balance of selected glaciers. Relations between the LSSARs and the AARs on the glaciers in the selected study regions are discussed in detail in Chapter 5.

The resulting late summer snow map can also be vectorized and combined with a DEM to get information on elevations of transient snow lines, often used as proxy for the equilibrium line altitude of a glacier.
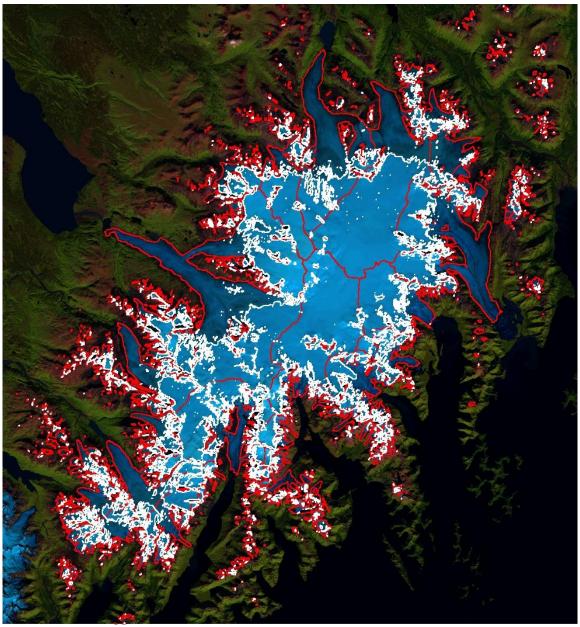
Figure 3.12: Outlines of the late summer snow areas on the Harding Icefield, Alaska, derived by applying the finally selected threshold on the topographically corrected TOAR map of Landsat band 4.

3.6 Validation of classification method

In this section options for validating the derived Late Summer Snow and Ice Areas (LSSIA) are described and the strengths and weaknesses of the various options are discussed. So far, snow products derived from optical satellite data were mainly validated by comparison with snow maps processed using different sensors. In some cases, results have been compared to in-situ measurements (e.g. Parajka and Blöschl, 2006) or snow maps derived by different snow retrieval methods (e.g. Hall and Riggs, 2007) .However,

these validations or comparisons refer to snow over ice-free land surfaces, the retrieval of which is simpler than snow on glaciers.

In the case of ice-free surfaces the two classes (snow vs. snow-free land) can be clearly discriminated because of pronounced spectral contrast, whereas snow and glacier ice show similar behaviour of spectral reflectance. Therefore, validating snow areas on glaciers is not simple. Another critical issue is the question of temporal dynamics. In comparison to the total glacier area, the extent of snow areas on glaciers may change rapidly. This requires close temporal coincidence of the data sets to be compared.

Preferably, these should be acquired on the same day. Time differences of a few days should usually not provide major errors, in particular if the meteorological data suggest that only minor changes in snow areas had occurred. Although the processed late summer snow and ice areas refer to dates near the end of the ablation period, validation of the algorithm and products can in principle also be performed with coincident data sets of dates earlier in summer. However, late summer data sets are preferable, as the snow albedo often decreases during summer, resulting in more challenging conditions for snow and ice area classification than in early summer.

The preferred option for the validation of late summer snow and ice areas are high resolution orthorectified images where snow and ice areas can be mapped automatically as well as manually. The main limitations for applying this option are the limited availability of such data sets (at the right time of the year) and the data costs. Glacier surfaces can significantly change within days, depending on the weather. Thus, data used for validation of glacier surfaces have to be taken as close as possible to the date of Landsat image acquisition used for the main processing. The time difference between acquisition date of the Landsat image and the orthophoto used for validation should be less than one week. This requirement significantly limits the data sets for validation, as both, a Landsat scene and an orthophoto have to be available. Larger temporal differences between the acquisition of satellite imagery and an orthophoto question the comparability of the late summer snow areas due to changes of the glacier surfaces either due to melting or snow fall events. Another option is the use of oblique airborne and/or in situ photos, often enabling clear identification of the snowline on glaciers by manual methods. However, a difficult problem is the accurate geometric rectification of these data. Also, in most cases such images cover only part of a glacier.

Sometimes high resolution optical data of different sensors (e.g. Landsat, ASTER, or SPOT) are available on the same date or shifted in time by a few days. Producing late summer snow and ice area maps with these data does not allow a fully independent validation of the products. However, comparison tests would be relevant for the assessment of consistency of the products and for checking the processing line.

Mass balance maps show the extent of ablation and accumulation areas on glaciers at the end of the ablation period. The ablation and accumulation areas are often (but not necessarily) closely related to the snow area at the end of summer. Major differences may

occur for the following cases: (i) superimposed ice which belongs to the accumulation area; (ii) late summer snowfall which obscures the extent of the ablation area; (iii) remaining firn areas if the mass balance of the previous year was more positive or less negative. Another possible source of uncertainty is the accuracy of the ablation and accumulation areas in the mass balance maps because these may be based on different sources (point measurements in combination with in situ photos and/or aerial photos) which do not always provide the same level of detail over the full glacier area.

In two of the selected study regions, orthophotos of some glaciers meeting the temporal requirements are available for validation. Table 3.8 gives an overview on the data sets used for the validation of glacier surfaces.

Region	Number of investigated glaciers	Acquisition date	
		Landsat scene	Orthophoto
Ötztal Alps, Austria	4 individual glaciers	13/09/1999	09/09/1999
Breheimen, Norway	1 icecap, consisting of 8 outlet glaciers	10/08/2004	12/08/2004

Table 3.8: Data sets used for validation.

The time difference between acquisition date of the Landsat image and orthophoto used for validation is less than one week. Meteorological reanalysis data are reviewed to ensure, that no snow fall events or other relevant weather events occurred in the days between image acquisitions. Nevertheless, the used orthophotos are partly composites of several individual photos, and have partly different illumination conditions. This has to be considered, when automated snow mapping from orthophotos is attempted with thresholds on the single bands. Usually, a manual correction afterwards is necessary, or filling gaps by manual snow mapping may be required.

The digital orthophotos used for validation have pixel sizes of 1 m or 0.5 m. By comparing the products derived from orthophotos with those from Landsat data with 30 m pixel size, the different spatial resolutions can cause differences in results.

3.6.1 Validation methods

Based on orthophotos, the late summer snow area of selected glaciers is either derived by applying thresholds on the image channels of the orthophoto and manual correction afterwards or by purely manual mapping. The extent of snow covered areas on a glacier as well as the total glacier area are derived from the product of pixel size and according number of pixels, using the area equal projection Albers on the WGS84 ellipsoid. The

extent of the snow covered area on a glacier is set in relation to the total glacier area to derive the late summer snow area ratio (LSSAR).

Based on the DEM used for the main processing line, the area altitude distribution is extracted for the snow covered areas derived from the Landsat scene, for snow covered areas mapped from the orthophoto, and for the total area of the selected glacier. Thus, snow areas can be related to discrete elevation intervals and to the glacier extent in these elevation intervals.

3.6.2 Validation site Ötztal Alps, Austria

An orthophoto, Vernagtferner 1999 (Orthophotokarte, 2001), with the scale 1:10'000, covering four glaciers in the Ötztal Alps, Austria, was used for validation. The glaciers covered by this orthophoto are of different size, and different exposition, but contribute to the same basin (cf. *Figure 3.13*) and span over similar elevation zones.

The Landsat scene used for the validation covers inter alia several hundred glaciers. The threshold, 0.38, applied on the Landsat scene for retrieval of late summer snow areas is selected in order to find the best match for all glaciers on this scene. This threshold is also in line with the threshold used by Floricioiu et al. (2002) for snow classification from band 4 of the same Landsat scene.

The north-east corner of Vernagtferner is not covered by the orthophoto. Thus, the snow area in this part has been manually reduced to the margins of the orthophoto to make the snow areas derived from orthophoto comparable with those from the Landsat image. The late summer snow area ratio (LSSAR) of the reduced area on Vernagtferner compared to the LSSAR of the total snow area derived from Landsat is the same (0.52).
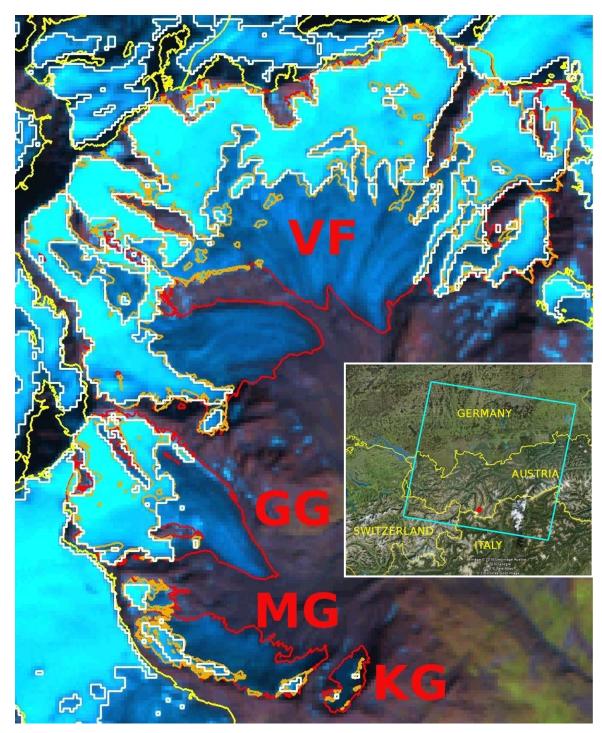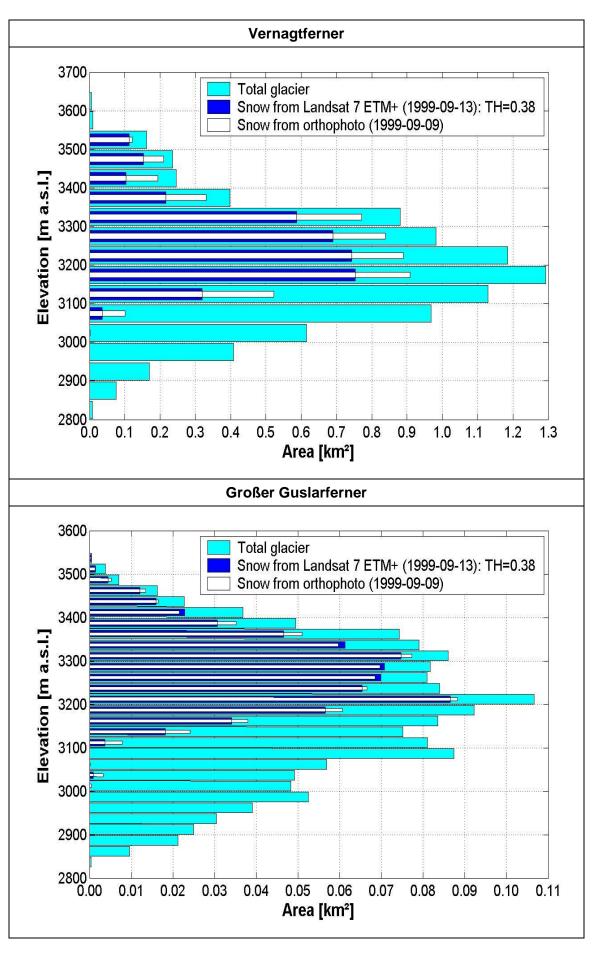
Figure 3.13: Subset of Landsat 7 ETM+ RGB543 composite (13/09/1999) covering the area of the orthophoto (09/09/1999) used for validation. Red outlines are the validated glaciers. The neighboured glaciers are indicated in yellow. Outlines of late summer snow areas derived from Landsat scene by the main processing line are drawn in white. Orange lines are outlines of late summer snow areas manually mapped from the orthophoto.
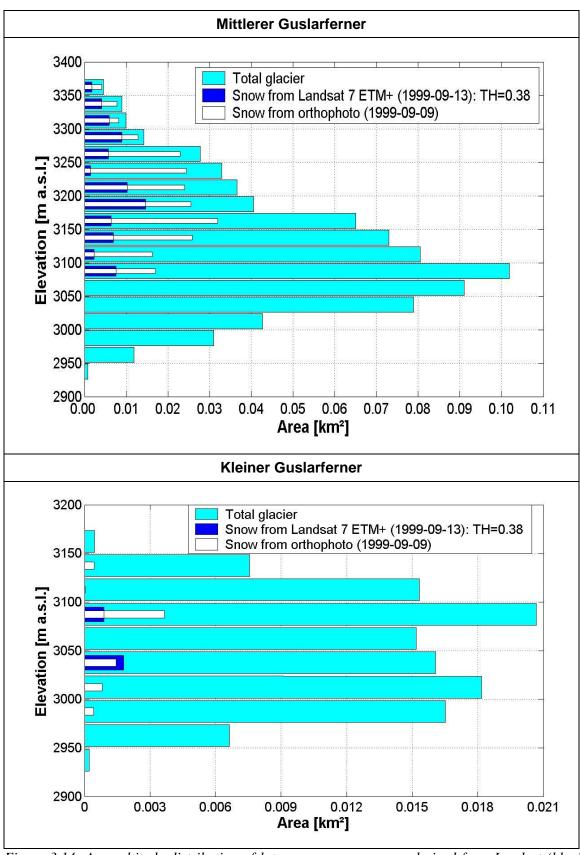
Figure 3.14: Area altitude distribution of late summer snow areas derived from Landsat (blue) and orthophoto (white), and total glacier area (cyan) of selected glaciers in Ötztal Alps, Austria. Areas of the Vernagtferner are grouped into 50 m elevation intervals. The areas of the other three glaciers are grouped into 25 m elevation intervals.

Glacier name	Exposition	Total glacier area [km²]	LSSA (LS) [km²]	LSSA (OP) [km²]	LSSAR (LS)	LSSAR (OP)
Vernagtferner	SE	8.7704	4.5170	4.8883	0.52	0.56
Grosser Guslarferner	E	1.4811	0.7691	0.7090	0.52	0.48
Mittlerer Guslarferner	NE	0.7526	0.1154	0.2210	0.15	0.29
Kleiner Guslarferner	N	0.1169	0.0027	0.0068	0.02	0.06

Table 3.9: Validation results of selected glaciers in Ötztal Alps, Austria. LSSA = Late summer snow area. LSSAR = Late summer snow area ratio. LS = Landsat. OP = Orthophoto.

Glacier outlines for Ötztal Alps have been mapped based on orthophotos of 1997 (Lambrecht and Kuhn, 2007), and were by courtesy made available by A. Lambrecht, Institute of Meteorology and Geophysics, University of Innsbruck, Austria. These outlines have been manually updated based on the orthophoto of Vernagtferner 1999 (Orthophotokarte, 2001). The updated outlines were used for all validation activities in the Ötztal Alps.

Table 3.9 shows the validation results of the individual glaciers of Ötztal Alps, Austria. Snow areas derived from Landsat image, and snow areas derived from orthophoto are set into relation to the total glacier area of the associated elevation intervals. The late summer snow areas (LSSA), and the associated late summer snow area ratios (LSSAR) for the snow areas derived from Landsat image and orthophoto are compared for each glacier.

The late summer snow areas show deviations between 0.0041 km² on Kleiner Guslarferner and 0.3713 km² on Vernagtferner. For three of four investigated glaciers, the resulting LSSAR derived from Landsat image and from orthophoto deviate by about 0.04. In case of Mittlerer Guslarferner, the deviation of the LSSAR is about 0.14. On this glacier, the snow area mapped from orthophoto exceeds that derived from Landsat image at all altitude intervals (Figure 3.14).

This is partly caused by areas located in cast shadows and thus not classified as snow from the Landsat image with the main processing line. In other parts, the snow areas mapped from the orthophoto cover only small parts of single Landsat pixels. These effects cumulate and result in the relatively large difference in the LSSAR. In addition, there was some remnant new snow from a recent snow fall on the north-facing slopes on 9 September (orthophoto) melting away until 13 September (Landsat).

The graphics in Figure 3.14 are the associated area altitude distributions of the late summer snow areas derived from Landsat and orthophoto per total glacier area in discrete elevation intervals of all investigated glaciers in this region.

3.6.3 Validation site Breheimen, Norway

Spørteggbreen is a small icecap located in Breheimen, Norway, leeward the large icecap Jostedalsbreen. On 10 August 2004, a Landsat 7 ETM+ scene with Spørteggbreen in the scene centre was taken. Thus, although the scan line correction (SLC) did not work anymore, the icecap is scanned without any data gaps. An orthophoto of Spørteggbreen is available for 12 August 2004.

An archive of available orthophotos of Norway is online provided via http://norgeibilder.no. Although the descriptions on this webpage are only in Norwegian, a self-explaining graphical navigation interface, and an easy search panel help the user searching and browsing the available data sets. For visualizing differences on glacier surfaces, a high zoom to the selected glacier is required, meaning a scale of 1:50000 or better with 0.5 m resolution of the original data. The orthophotos themselves, including geometric information, are not downloadable from this homepage, but screenshots of selected areas can be saved in any graphical format, as for example jpg. To make the saved image useable for validation, the graphic has to be orthorectified afterwards using manually selected ground control points (GCPs) and a digital elevation model. While orthorectification requires relatively large effort, those orthophotos have been prepared only for a few selected regions.

The Landsat scene used for validation purposes has useful data only in the centre of the scene due to the failure of the Landsat scan line corrector (SLC) end of May 2003 (Chander et al., 2009b). Furthermore, the scene originally was only available as L1G product, which means, that it was only radiometrically and geometrically corrected, but not terrain corrected, resulting in a shift of several hundred meters. Using manually selected ground control points and the national DEM of this region, the Landsat scene was orthorectified, projected to UTM with WGS84 ellipsoid, and thereby resampled to the pixel size of the DEM (25m). The national DEM, as well as initially used glacier outlines of Norway have been kindly made available by L.M. Andreassen, from the Norwegian Water Resources and Energy Directorate (NVE), Norway. The glacier outlines are now also online available on the GLIMS data base (http://www.glims.org).

The icecap Spørteggbreen consists of 8 outlet glaciers. The total area of the icecap, based on the outlines of 2003 available via GLIMS data base, is 27.468 km². When the total area is derived via pixel counting from the Landsat image of 2004, this value increases to 27.828 km² due to the slight area bias of the UTM projection (cf. section 3.2.1).

For Spørteggbreen, Norway, the area-altitude distributions of the snow areas and the total icecap are presented in Figure 3.16. In most of the elevation intervals, the snow area

derived from Landsat image fits the snow area mapped from the orthophoto. This also agrees with the derived late summer snow area ratios (LSSAR), which is 0.42 in both cases. The difference for the LSSAR of the total icecap is about 0.06 %. In terms of areas, the snow area derived from Landsat data is 11.80 km², while the snow area mapped from orthophoto covers 11.62 km².
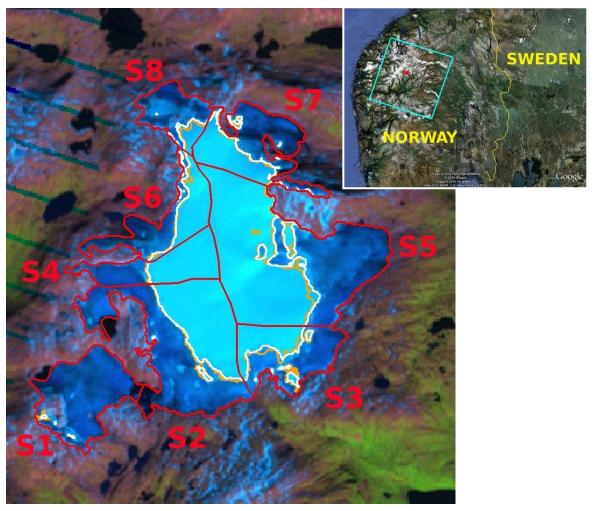
Figure 3.15: Subset of Landsat 7 ETM+ RGB543 composite of 10/08/2004 showing the icecap Spørteggbreen, combined with glacier outlines (red), late summer snow derived by the standard processing line from the Landsat scene (white) and manually mapped from orthophoto of 12/08/2004 (orange). The IDs S1 – S8 refer to the glacier IDs. Upper right corner: location and extent of the Landsat scene (blue) and the orthophoto (red dot).
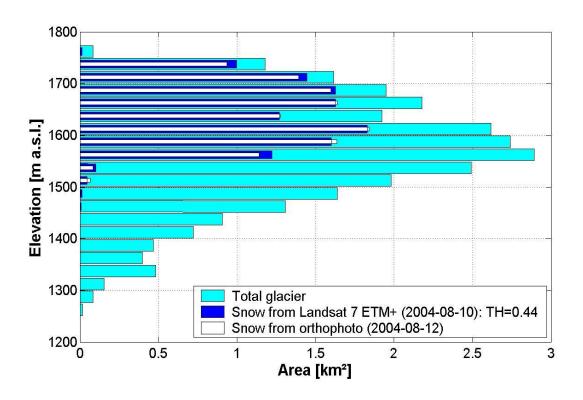
Figure 3.16: Area altitude distribution of late summer snow areas and total glacier area of Spørteggbreen per 25 m elevation interval, derived from national DEM.

Glacier ID	Exposition	Glacier area [km²]	LSSA (LS) [km²]	LSSA (OP) [km²]	LSSAR (LS)	LSSAR (OP)
S1	SSW	2.949	0.0119	0.0200	0.004	0.007
S2	SW	6.064	2.3569	2.4450	0.39	0.40
S3	SE	2.484	0.9263	1.0056	0.37	0.40
S4	W	1.869	1.1925	1.2056	0.64	0.64
S5	E	8.054	4.9144	4.7013	0.61	0.58
S6	NW	2.169	0.9725	0.9306	0.45	0.43
S7	NE	2.834	1.1644	1.1181	0.41	0.39
S8	NNW	1.404	0.2581	0.1931	0.18	0.14
Total		27.877	11.797	11.6193	0.42	0.42

Table 3.10: Validation results of individual glaciers of the icecap Spørteggbreen, Norway. LSSA = Late summer snow area. LSSAR = Late summer snow area ratio. LS = Landsat. OP = Orthophoto.

If individual glaciers are used for validation, this difference can be larger for some of the glaciers. Table 3.10 shows the validation results for the individual glaciers on the icecap. Differences in the late summer snow areas vary between 0.0081 km² on S1 and 0.2131 km² on S5. The LSSARs of individual glaciers of Spørteggbreen derived from Landsat and from orthophoto show a minimum difference of 0.003 on S1 and a maximum difference of 0.04 on S8.

3.7 Error sources for classification of late summer snow and ice areas

Classification errors of LSSIA can be caused by large crevasses (Pfeffer and Bretherton, 1987), polluted snow, bright glacier ice, clouds, cloud shadows, or cast shadowed areas.

As already mention in Section 3.2.1, optical satellite imagery with extensive cloud coverage should be excluded from the selected data base. When this is not possible, or clouds cover only small parts of a scene, it is useful to mask the clouds and their shadows to avoid misclassification during the semi-automated LSSIA classification. For automated mapping of water clouds often the NDSI (cf. Section 3.1) combined with a threshold is a useful tool to discriminate snow and ice surfaces from clouds. Unfortunately, this method is not absolutely accurate. Thus, a manual post-mapping is usually required. In case of ice clouds, the NDSI is not of use. The signal reflected from bright glacier surfaces, such as snow covered areas, can partly even penetrate thin ice cloud layers. Especially on large snow covered icecaps, it is very difficult to discriminate a thin ice cloud layer from the underlying snow area. Careful cloud detection before the semi-automated processing line is started for the retrieval of LSSIA not only avoids misclassification, but also enables more straight forward processing when the error introducing areas are manually masked out.

Misclassifications due to large crevasses mainly occur on the tongues of large glaciers. Therefore, the solar angle, the incidence angle of the incoming radiation, the position of the satellite sensor, the form and exposition of the glacier crevasses and the ice albedo of the inner walls of the crevasse are relevant variables. Such misclassifications are usually clearly identifiable and can thus easily be manually corrected after the main processing line.

Shadowed areas on glaciers are main error sources for the retrieval of glacier facies. As most of the investigated glaciers are located in mountainous, partly very steep terrain, the error due to cast shadow on some of the glaciers is large. A manual correction in such areas is difficult due to the low contrasts. A cast shadow mask derived from a DEM and calculated for the solar position at the optical satellite image acquisition date and time can help to be aware of the problematic zones. For the generation of a cast shadow mask, the region of interest should be reduced as far as possible, as the calculation of a cast shadow mask requires high computational effort. Regardless the high computing power, a DEM

with high quality and small pixel size should be used, as these parameters directly affect the quality of the cast shadow mask.

Polluted snow and bright glacier ice areas are very difficult to be determined as sources for the misclassification of LSSIA. In both cases, seasonal time series of optical satellite imagery might help to identify such regions. But the required imagery is not always available. In general, errors introduced due to these glacier surfaces are considered as a factor of uncertainty in the final LSSIA classification.

3.8 Error estimation

The main problems for identifying glacier facies are related to:

1. Fresh snow fall that covers the glacier surface.

2. Low contrast in reflectance of snow and ice.

3. Topographic corrections impaired by DEM errors.

4. Discrimination of snow vs. firn (névé).

5. Identification of superimposed ice.

(1) Fresh snow fall can occur on glaciers any time and may hide the snow line and the ice area partly or completely. Such images need to be excluded for the analysis of glacier facies. Time series help to find the image taken closest to the maximum extent of the ablation areas on glaciers. If only a single image is available, the presence of fresh snow can be assessed by checking the ice-free areas surrounding the glacier. Another option is the use of meteorological data to check the possibility of recent fresh snow fall, though local effects may cause uncertainties in inferring snow fall from station data of numerical meteorological data.

(2) The albedo difference between snow and glacier ice is sometimes small in late summer, because the snow surface may be polluted by dust originating from the surrounding terrain or from long-range transport. Possible classification errors due to this effect can be checked by visual inspection of the images and the classification results. Glacier ice areas usually reveal different surface texture (flow lines, drainage features) than snow areas.

(3) The classification of snow and ice areas is based on parametrically corrected TOA reflectance. The atmospheric propagation effects play a minor role compared to the geometric corrections. The quality of the geometric corrections depends on the quality of the DEM. The impact of the DEM was investigated in all study regions by comparing classification results derived with different DEMs used for the processing line. The use of low resolution DEMs results in misclassifications of parts of the snow covered areas on glaciers, mainly in steep terrain. Therefore the highest resolution available DEM should

be used for processing, even if processing time slightly increases due to larger image files.

(4) The discrimination of late summer snow of the current year and névé may cause problems in some years, if the reflectance properties of these two snow types are similar. Névé is snow of previous years and belongs to the ablation area of a glacier. If the mass balance should be inferred from snow and ice area extent this discrimination is important. Multi-annual névé usually has lower albedo than snow of the current year, so that in these cases the discrimination is a minor problem. In some years, when the mass balance is more positive (or less negative) than in the previous year(s), névé areas may not be apparent on the glacier surface, so that this problem does not exist. A sequence of end of summer satellite images over 2 or more years help to understand if this problem exists in a given year. The comparison with field photography and air photos (oblique or orthophotos) can also help to avoid misclassification.

(5) Superimposed ice is melt water that refreezes in early summer on the cold ice surface below the winter snow. Superimposed ice is an important component of the mass balance on Arctic glaciers, as it belongs to the accumulation area. The spectral reflectance of superimposed ice is similar to that of glacier ice, so that the discrimination of these two target types is hardly possible. The classification of snow and ice areas is correct in these cases, but these areas do not fully agree with the extent of the accumulation and ablation areas. This would affect the estimation of the mass balance.

3.8.1 Sensitivity of late summer snow / ice area classification on threshold selection

The quality of the retrieved late summer snow/ice area extents varies from glacier to glacier within a scene due to the application of a mean threshold. Nevertheless, the accuracy of the LSSIA on the glaciers used for validation is in most cases within a range of 0.05 regarding the late summer snow area ratio (LSSAR). In one case, the deviation of the LSSAR is 0.14, while this difference is mainly caused by snow in cast shadowed areas mapped from the orthophoto, but not classified via the standard processing line from the Landsat image.

Based on the available data sets used for retrieval of LSSA the impact of the DEM quality and of the selected threshold on the quality of the final products was investigated in selected study regions by:

- Varying the selected threshold by +/- 0.05, and +/- 0.02.

- Using different DEMs for the processing line.

- Using different DEMs for the processing line and varying the selected threshold by +/- 0.05, and +/- 0.02.

Region	No. of scenes	Statistical parameter	Change of LSSAR (TH +/- 0.05)	Change of LSSAR (TH +/- 0.02)
Alaska	8	MIN	+/- 0.01	0.00
		MAX	+/- 0.19	+/- 0.10
		MEAN	+/- 0.07	+/- 0.03
		STDEV	0.05	0.03
Alps	7	MIN	+/- 0.03	+/- 0.01
		MAX	+/- 0.14	+/- 0.03
		MEAN	+/- 0.06	+/- 0.02
		STDEV	0.02	0.01
Baffin Island	7	MIN	+/- 0.05	+/- 0.02
		MAX	+/- 0.28	+/- 0.10
		MEAN	+/- 0.11	+/- 0.05
		STDEV	0.07	0.03
Norway	3	MIN	+/- 0.06	+/- 0.02
		MAX	+/- 0.11	+/- 0.03
		MEAN	+/- 0.07	+/- 0.02
		STDEV	0.02	0.00
Himalaya	6	MIN	+/- 0.03	+/- 0.01
		MAX	+/- 0.14	+/- 0.06
		MEAN	+/- 0.07	+/- 0.03
		STDEV	0.04	0.02

Table 3.11: Summary of changes in late summer snow area ratio for investigated scenes in different regions due to variations of the selected threshold. LSSAR = late summer snow area ratio, TH = threshold, MIN = minimum change, MAX = maximum change, MEAN = mean change, STDEV = standard deviation.

Varying the selected threshold by +/-0.05 has a scene dependent effect on the late summer snow and ice areas on glaciers. The change in the resulting snow area ratios on the selected images ranges between +/-0.01 and +/-0.28, with an overall mean change of +/-0.07. By reducing the variation of the threshold to +/-0.02, the change in the resulting late summer snow area ratio ranges between 0.00 and +/-0.10, with a mean deviation of about 0.03 in most regions and of 0.05 for the investigated scenes covering glaciers of Baffin Island. Table 3.11 summarizes the changes in late summer snow area ratios due to variations of the selected threshold for investigated scenes in different regions.

The horizontal deviation of the late summer snow line, where it was definable, showed in general an accuracy of +/- 2 Landsat pixels. In a few parts of the validated glaciers, the

deviation of the LSSL derived from orthophoto and compared to that derived from Landsat image increases to 11 Landsat pixels. Those areas are in most cases partly snow covered but also partly ice covered. Matching the classification from Landsat data as snow or ice, respectively, would require a change in the selected threshold, resulting in clear misclassifications in other regions of the scene.

Varying the selected threshold by +/-0.05 has a scene dependent effect on the late summer snow and ice areas on glaciers. The change in the resulting snow area ratios on the selected images ranges between +/-0.01 and +/-0.28, with an overall mean change of +/-0.07. By reducing the variation of the threshold to +/-0.02, the change in the resulting snow area ratio ranges between 0.00 and +/-0.10, with a mean deviation of about 0.03 in most regions and of 0.05 for the investigated scenes covering glaciers of Baffin Island. Table 3.11 summarizes the changes in snow area ratios due to variations of the selected threshold for investigated scenes in different regions.

3.8.2 Influence of DEM on late summer snow area retrieval

Not only the kind of topographic correction and the threshold selection, but also the resolution of the DEM used as basis for the topographic correction is critical for the quality of the resulting glacier surface maps. The effect of different DEM pixel sizes on the derived LSSAR is investigated for scenes in the selected key regions, comparing the available DEMs. The same Landsat scene per region is processed with each of these DEMs, and glacier surface maps are derived following the main processing line (cf. Chapter 3.5).

The variation of the LSSAR due to the use of different DEMs for the main processing line ranges between 0.001 for the selected scene in Himalaya and 0.031 for the scene covering Flade Isblink in Greenland.

An additional variation of the threshold by ±0.02 results in changes of the derived LSSAR between 0.018 and 0.044. Changes between 0.046 and 0.16 are observed if the threshold is varied about ±0.05.

Table 3.12 shows the late summer snow area ratios of selected scenes in different regions using various DEMs for the main processing line, and varying thresholds (TH) for the retrieval of late summer snow/ice areas.

Region	No. of scenes	Used DEM	LSSAR (TH)	Change of LSSAR (TH +0.05)	Change of LSSAR (TH -0.05)	Change of LSSAR (TH +0.02)	Change of LSSAR (TH -0.02)
Greenland	1	INSAR	0.490	-0.157	0.099	-0.044	0.037
		VIEW-FINDER	0.497	-0.135	0.094	-0.035	0.033
		GETASSE	0.495	-0.157	0.099	-0.044	0.037
		ASTER	0.466	-0.160	0.102	-0.044	0.037
Patagonia	2 (merged)	SRTM	0.454	-0.068	0.048	-0.022	0.019
		GETASSE	0.447	-0.066	0.049	-0.022	0.020
		ASTER	0.434	-0.089	0.058	-0.029	0.025
Alaska	1	USGS	0.485	-0.054	0.051	-0.020	0.020
		GETASSE	0.471	-0.051	0.053	-0.020	0.020
		ASTER	0.474	-0.065	0.058	-0.024	0.023
Alps	1	NATIONAL	0.180	-0.054	0.051	-0.021	0.020
		VIEW-FINDER	0.191	-0.056	0.055	-0.022	0.022
		SRTM	0.192	-0.057	0.055	-0.022	0.022
		ASTER	0.189	-0.055	0.054	-0.022	0.022
Himalaya	1	VIEW-FINDER	0.252	-0.056	0.048	-0.021	0.019
		SRTM	0.251	-0.053	0.047	-0.018	0.018
		ASTER	0.248	-0.052	0.046	-0.018	0.018

Table 3.12: Summary of snow area ratios derived for selected scenes in different regions using several DEMs, but the same threshold for the retrieval of late summer snow/ice area maps, as well as changes of snow area ratios due to variations of the threshold of +/- 0.05 and +/- 0.02.

4. Maps of late summer snow and ice areas in the different study regions

4.1 Study areas

For this study, twelve regions in seven countries were selected (cf. Table 4.1). For nine of these regions, late summer Landsat imagery from several years meeting the requirements described in section 3.2.1 is analysed (Table 4.1). Exceptions are the icecap Flade Isblink in Greenland, marked by the light blue star in Figure 4.1, where only one Landsat image meeting the requirements is available, and glaciers in the region Breheimen, marked by the red star in Figure 4.1, which are only used for validation purposes, as a high resolution orthophoto taken close to the Landsat image acquisition date is available for selected glaciers. Nevertheless, this study area is used to extend the data base for a spatial comparison of glacier facies at the end of summer, as Landsat imagery of this year is also available for most of the other selected regions.

Country	Region	DEM
Alaska	Harding Icefield, Sargent Icefield, Grewingk-Yalik Glacier Complex	USGS
Austria	Stubai Alps, Ötztal Alps (validation)	National (10 m)
Baffin Island, Canadian Arctic	Barnes Icecap	GETASSE
Chile	North Patagonian Icefield	SRTM
Greenland	Flade Isblink	VIEWFINDER
Nepal	Sagarmatha	VIEWFINDER
Norway	Svartisen, Blåmannsisen; Breheimen (only validation)	National (25 m)

Table 4.1: Overview on the regions selected for case studies and validation purposes, and the DEMs used for processing line.

Figure 4.1 shows an overview on the locations of the selected regions. For the regions marked with yellow stars late summer Landsat images of several years are investigated. The red star with yellow outline over the European Alps indicates that glaciers in this region are additionally used for validation purposes due to the availability of a very high resolution orthophoto of selected glaciers, taken close to the Landsat image acquisition (cf. Section 3.6).

Figure 4.1: Overview on the selected regions for processing late summer snow and ice areas on glaciers.

Areas of the glaciers and icecaps investigated in this study range between <0.1 km² and more than 9000 km². Landsat imagery enables the detection of areas equal or larger than 0.001 km², which corresponds to 1 Landsat pixel. The largest icecaps investigated in this study are Flade Isblink in Greenland with a total glacier area of about 9100 km², and Barnes Icecap on Baffin Island in the Canadian Arctic with a total glacier area of ca. 5900 km². The glacier areas in the other study regions are significantly smaller, and total glacier areas range from about 36 km² in the Stubai Alps, Austria, to about 4140 km² on the North Patagonian Icefield, Chile. Figure 4.2 gives an overview on the distribution of the total glacier areas in the selected study regions.

Investigations on the icecaps in Greenland and on Baffin Island are performed for the total area, the outlet glaciers are not investigated individually. In the remaining regions, the investigations of late summer snow areas are not only related to the total glacier area in the regions, but also to individual glaciers, considering glacier size and glacier exposition.

Table 4.2 and Figure 4.2 show the distribution of the number of glaciers in the selected study areas classified according to the individual glacier size. In the following sections, the glaciers of all selected study regions are classified by the glacier area (Table 4.2). Also the discussions in Chapter 5 refer to this classification.

Glacier class	Glacier area [km²]	HI	SI	GYGC	ST	OE	SV	BL	SA	NPI	BI	FI
1	0.01 - <0.1	447	770	179	30	74	139	20	41	0	0	0
2	≥0.1 – <1.0	240	355	82	35	105	211	33	108	9	0	0
3	≥1.0 – <10	65	118	12	11	27	83	16	38	63	0	0
4	≥10 - <100	16	37	13	0	1	10	2	7	27	0	0
5	≥100 - <1000	6	3	0	0	0	0	0	0	9	0	0
6	≥1000	0	0	0	0	0	0	0	0	0	1	1
	Total	774	1283	286	76	207	443	71	194	108	1	1

Table 4.2: Glacier class definition and number of glaciers in the selected study areas classified by the glacier size. HI = Harding Icefield, SI = Sargent Icefield, GYGC = Grewingk-Yalik Glacier Complex, ST = Stubai Alps, OE = Ötztal Alps, SV = Svartisen, BL = Blåmannsisen, SA = Sagarmatha, NPI = North Patagonian Icefield, BI = Barnes Icecap, FI = Flade Isblink.
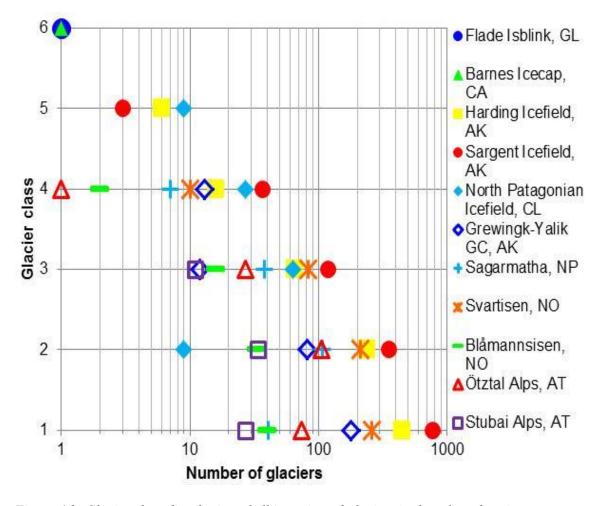
Figure 4.2: Glacier class distribution of all investigated glaciers in the selected regions.

The altitudes of the selected glaciers and icecaps range between sea level and more than 8200 m a.s.l. in the case of the glaciers in the Sagarmatha basin in the central Himalaya. The area altitude distributions for the mountain glaciers, as well as icefields and icecaps in the different regions are compared in Figure 4.3 and Figure 4.4, respectively. Due to the large differences in the glacier areas and the altitude ranges, two figures with different scales are used to show the area altitude distributions.
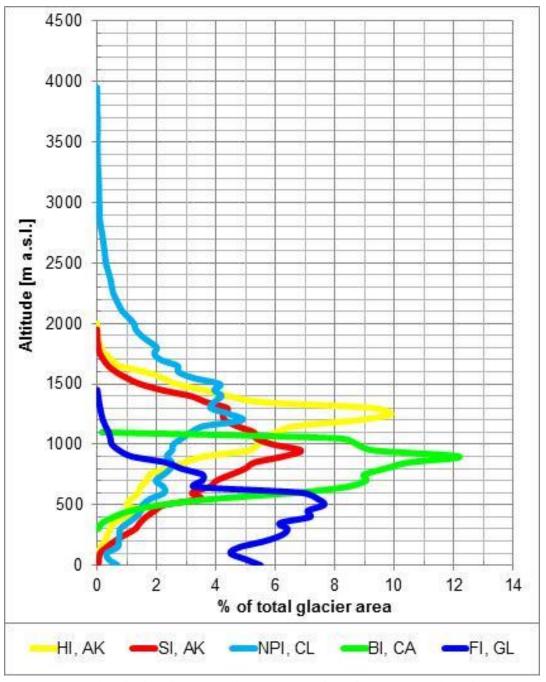
Figure 4.3: Area altitude distribution of glaciers, icefields and icecaps in selected regions. Total glacier areas of all shown regions are larger than 2000 km². Areas are derived for 50 m elevation intervals and presented as percental of the total glacier area.
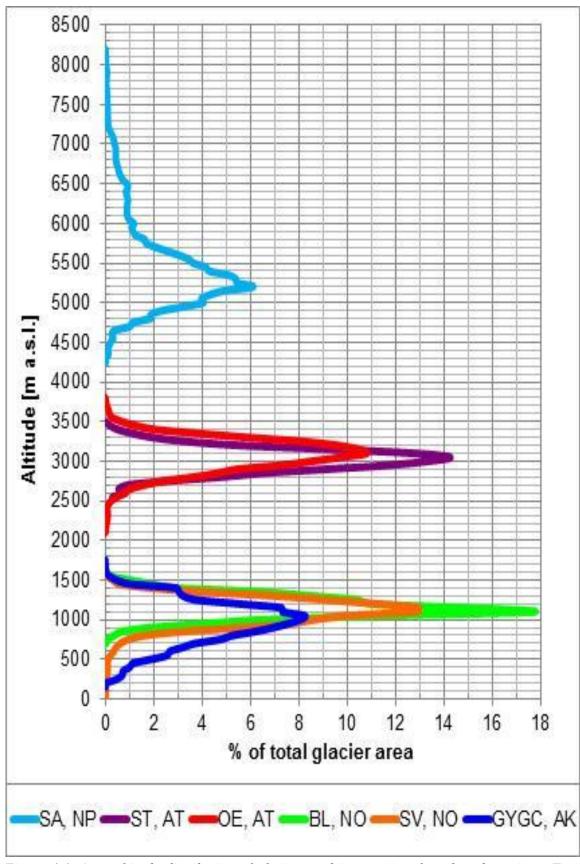
Figure 4.4: Area altitude distribution of glaciers and icecaps in selected study regions. Total glacier areas of all shown regions are smaller than 600 km². Areas are derived for 50 m elevation intervals and presented as percental of the total glacier area.

It is obvious, that the glaciers and icecaps located in different regions all over the world are influenced by different meteorological and climatological conditions. All regions, except of the European Alps and Sagarmatha in Nepal, are located in high latitudes, and close to the coast. The glaciers in the European Alps and in the Himalaya are instead located at higher altitudes.

More details on climatologic influences and individual characteristics of the study regions are given in the following sections, where case studies are presented for each region for the summer seasons 2000 and 2001, respectively.

4.2 LSSIA maps of the selected glacier regions in different climate zones

Based on the processing line described in Chapter 3 even large data sets can be computed with relatively small effort.

The semi-automated method is used to retrieve LSSIA in different climate zones all around the world. In this section, case studies for all selected regions are presented for the summer 2000 or 2001, respectively, depending on the availability of Landsat imagery meeting the requirements described in Section 3.2.1. The results of the case studies are shown in the following subsections.

4.2.1 Alaska: Sargent Icefield (21/08/2001), Harding Icefield (12/08/2001), and Grewingk-Yalik Glacier Complex (09/08/2000), Kenai Mountains

The Kenai Mountains, including the Sargent Icefield, the Harding Icefield, and the Grewingk-Yalik Glacier Complex (GYGC), are located on the Kenai Peninsula, Alaska, at the coast of the Gulf of Alaska. The climate can be generally described as sub-Arctic maritime on the coastal side, and sub-Arctic continental on the lee side of the icefields (Adalgeirsdóttir et al., 1998). The Kenai Mountains, with elevations ranging from sea level up to over 1800 m a.s.l., form a massive barrier for the frequent cyclones transporting moist air from the Gulf of Alaska to the land, resulting in frequent and strong precipitation events in form of maritime snow on the eastside of the Kenai Mountains, but also cause a strong precipitation gradient towards the lee side of the mountains (Giffen et al., 2007).

Meteorological data of three stations in the vicinity of the Harding Icefield, Seward, located on the east side of the Harding Icefield, and Homer and Kenai, located on the west side of the Harding Icefield, illustrate this precipitation gradient (Adalgeirsdóttir et al., 1998).

Three regions of the Kenai Mountains are selected and named after the dominating glaciers or icefields, respectively, resulting in the Sargent Icefield (Figure 4.6) located in the northeast of the Kenai Peninsula, centred at about 60.25°N / 148,64°W, the Harding Icefield (Figure 4.8), located southwest of the Sargent Icefield with the centre at about 59,95°N / 150.14°W, and the Grewingk-Yalik Glacier Complex (Figure 4.10), located southwest of the Harding Icefield, in the southwest of the Kenai Peninsula centred at about 59,55°N / 150.85°W. Although the naming convention is reduced to these 3 names, not only the large outlet glaciers of the icefields are investigated in this study, but also several hundred small glaciers in the vicinity of the icefields.

The aspect patterns related to the number of glaciers of all three regions selected in the Kenai Mountains are very similar (Figure 4.5, upper row). About half of all glaciers in each region in the Kenai Mountains are southwest, west, or northwest orientated. About a quarter of the glaciers in all regions in Alaska are either northern or southern orientated. The rest of the glaciers have a dominant eastern component in the main aspect.
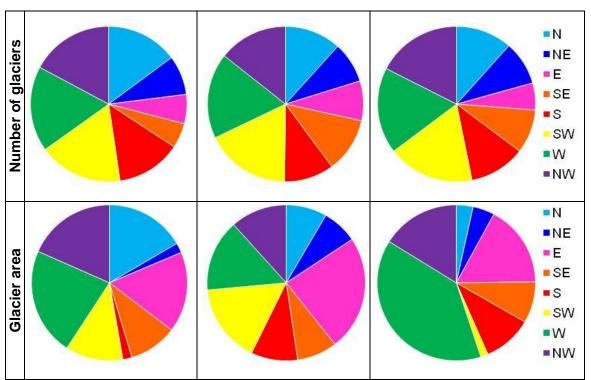
Figure 4.5: Main aspects of the glaciers located in the selected study regions in Alaska: Harding Icefield (left), Sargent Icefield (middle), and Grewingk-Yalik Glacier Complex (right). The graphics in the upper row show the main glacier aspects in dependence of the number of glaciers. The graphics in the lower row show the main glacier aspects in dependence of the glacier area.

Relating the glacier expositions to the glacier areas result in all regions in Alaska in different aspect distributions, driven by the expositions of the large glaciers in each region (Figure 4.5, lower row). In the region Harding Icefield, the aspect distribution in dependence of the glacier area is controlled by the six glaciers of glacier class 5: the west

orientated Tustumena Glacier (336.5 km²), the northwest orientated glacier Harding Icefield (206 km²), the southeast orientated Northwestern Glacier (161 km²), the east orientated Bear Glacier (149 km²), the north orientated Skilak Glacier (125.5 km²), and the southwest orientated McCarty Glacier (119 km²).

On the Sargent Icefield, the largest glacier is the east orientated Chenega Glacier with an area of about 392 km², mapped based on Landsat imagery of 2006. This glacier dominates the aspect distribution in dependence of the glacier area, followed by three further large glaciers, the south orientated Excelsior Glacier (129 km²), the southwest orientated Ellsworth Glacier (123.5 km²), and the southeast orientated Princeton Glacier (104 km²). Several west and northwest orientated glaciers with an area between 10 km² and 100 km² are located at the Sargent Icefield, resulting in relatively large parts of these expositions in the aspect distribution related to the glacier area.

For the Grewingk-Yalik Glacier Complex, the aspect distribution in dependence of the glacier area is driven by several west orientated glaciers with a glacier area between 10 km² and 100 km², including the largest glacier, the Grewingk Glacier (72 km²). The east orientated Yalik Glacier (52 km²) is the second largest glacier. Beside several glaciers with an area between 1 km² and 10 km², this glacier mainly contributes to a relatively strong east component in the aspect distribution related to the glacier area compared to that related to the number of glaciers. Both large glaciers are used for the naming convention of this region. The strong presence of the northwest orientation in the aspect distribution related to the glacier area is driven by several glaciers with an area between 1 km² and 10 km².

The glacier altitudes of the Sargent and the Harding Icefield reach about 1800 m a.s.l., while the maximum elevation on the Grewingk-Yalik Glacier Complex is about 1500 m a.s.l.. The main glacier area of the Sargent Icefield and of the Grewingk-Yalik Glacier Complex is located between about 800 m a.s.l. and 1100 m a.s.l. (Figure 4.7 and Figure 4.11), while it is slightly higher on the Harding Icefield, between about 1000 m a.s.l. – 1300 m a.s.l. (Figure 4.9).

The three regions are covered by Landsat images defined by 3 different paths, 067 – 069, along the row 018. The USGS path and row system as graphic or an online converter of path and row to geographical coordinates is online available at http://landsat.usgs.gov. The Sargent Icefield is covered by the Landsat images with the paths 067 and 068 and the row 018, the Harding Icefield is covered by Landsat images with the paths 068 and 069 and the row 018, and the Grewingk-Yalik Glacier complex is completely covered by the Landsat path 069 and the row 018. Images with the path 068 and the row 018 cover only the northern part of the Grewingk-Yalik Glacier Complex, and are thus not used for further investigations, although the imagery is processed.

For all three regions, the USGS DEM with 60 m resolution is used for the main processing line, and for the retrieval of topographic information of the glaciers and the

resulting late summer snow areas. Glacier outlines of the Kenai Mountains were mapped within GlobGlacier, and are now publicly available via the GLIMS data base.

For the case studies in Alaska, three different Landsat images are required to cover all named regions with images meeting the requirements. For the Sargent Icefield, a Landsat 7 ETM+ scene of 21 August 2001, Path 068 / Row 018, is used for the case study. This image has significant cloud coverage over parts of the Harding Icefield. Thus, for the Harding Icefield, another Landsat 7 ETM+ scene, path 069 row 018, recorded on 12 August 2001 was used. Unfortunately, the Grewingk-Yalik Glacier Complex, also covered by this scene, is covered by high clouds over large areas. Other scenes of 2001 showing the Grewingk-Yalik Glacier Complex do not meet the requirements. Thus, a Landsat 7 ETM+ scene, path 069 row 018, of 09 August 2000 is used for the case study on the Grewingk-Yalik Glacier Complex.

Region	Path/Row	Image acquisition date	Applied threshold	Total glacier area [km²]	Total late summer snow area [km²]	LSSAR
Sargent Icefield	068 / 018	21/08/2001	0.35	2204.51	1181.58	0.54
Harding Icefield	069 / 018	12/08/2001	0.48	2011.77	1482.49	0.74
Grewingk-Yalik Glacier Complex	069 / 018	09/08/2000	0.31	458.52	314.54	0.69

Table 4.3: Summary of the data base and the results derived for the case studies on glaciers in the selected regions in Alaska.

The applied threshold for the Landsat 7 ETM+ scene of 21 August 2001, showing the Sargent Icefield, is 0.35, resulting in a total snow covered area of about 1182 km². Related to the total glacier area, about 2204 km², a late summer snow area ratio of 0.54 is derived for all glaciers in the region Sargent Icefield. Between 700 m a.s.l. and 1500 m a.s.l. more than the half of the glacier area per elevation interval is covered by snow, with the largest snow covered area located between 900 m a.s.l. and 1000 m a.s.l, where also the largest total glacier area is found. The lowest elevation where snow is classified is between 200 m a.s.l. and 300 m a.s.l.. Figure 4.6 shows the RGB 543 composite of the investigated Landsat 7 ETM+ subset combined with glacier outlines and the derived outlines of the late summer snow areas. The associated area altitude distribution of both, total glacier and snow area of this region is presented in Figure 4.7. Information on the case studies in Alaska and the classification results are summarized in Table 4.3.
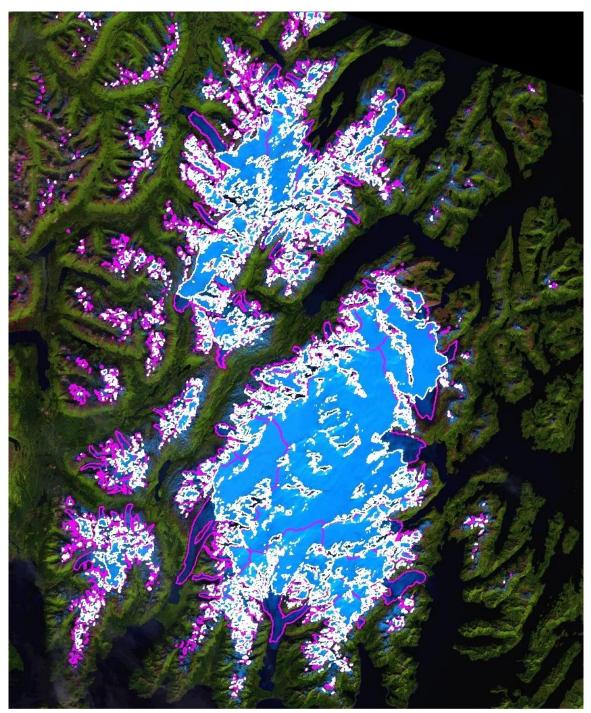
Figure 4.6: Outlines of the late summer snow areas (white) on the glaciers (pink) of Sargent Icefield and surrounding glaciers, derived from Landsat 7 ETM+ scene of 21 August 2001 (Path 068 / Row 018). The applied threshold is 0.35. The DEM of USGS is used for the processing line.

On the Landsat 7 ETM+ scene of 12 August 2001, covering the Harding Icefield, a threshold of 0.48 is used for the snow classification. The resulting snow covered area is about 1482 km², ranging between about 300 m a.s.l. and 1900 m a.s.l.. Between 800 m a.s.l. and 1700 m a.s.l. large parts of the glacier areas per elevation interval are covered by snow. With a total glacier area of about 2012 km² in the region Harding Icefield, the

associated late summer snow area ratio is about 0.74. The total glacier area of the region Harding Icefield includes also glaciers of the surroundings of the Harding Icefield itself, and is based on glacier outlines mapped during the ESA project GlobGlacier from Landsat imagery of 2006. This area is used as reference in this study, as all investigations are based on these glacier outlines, although Giffen et al. (2007b) reported a smaller total glacier area of 1902.79 km² for the Harding Icefield and surrounding glaciers, mapped from a Landsat 7 ETM+ scene of 09 August 2000. Based on the publication of Giffen et al. (2007b), it is not clearly obvious, which glaciers of the surroundings are included in this area calculation, but the difference in the retrieved areas should be kept in mind.
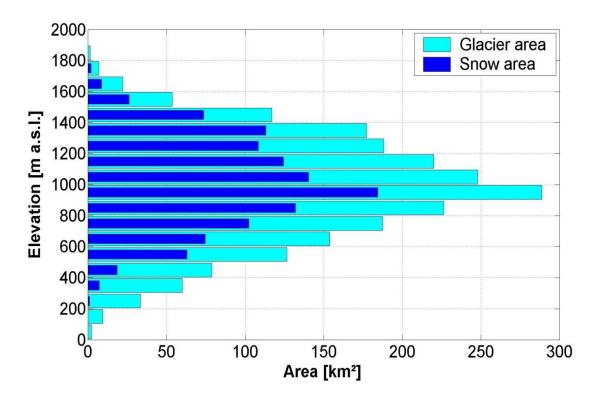
Figure 4.7: Area altitude distribution of the snow covered area on Sargent Icefield and surrounding glaciers, and of the total glacier area based on the USGS DEM. The late summer snow area is derived from the Landsat 7 ETM+ scene of 21/08/2001, applying the threshold 0.35. Areas are grouped into 100 m elevation intervals.

Figure 4.8 shows the outlines of the late summer snow areas and the glaciers of the Harding Icefield, based on the RGB 543 composite of the Landsat 7 ETM+ scene (Path 069 / Row 018) of 12 August 2001. The associated area altitude distribution of the late summer snow and the glacier area derived from the USGS DEM is shown in Figure 4.9.
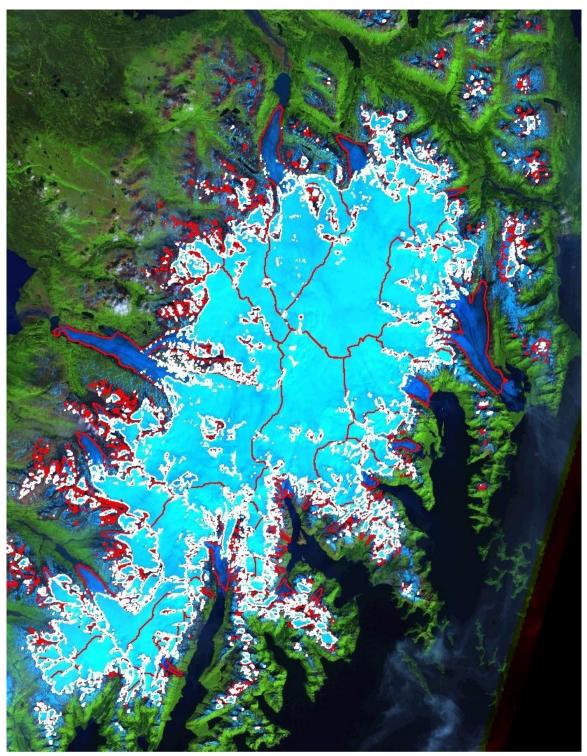
Figure 4.8: RGB 543 composite of Landsat 7 ETM+ (Path 069 / Row 018) showing the Harding Icefield on 12 August 2001. Glacier outlines (red) and late summer snow area outlines (white) are overlaid. The applied threshold is 0.48. The DEM of USGS is used for the processing line.
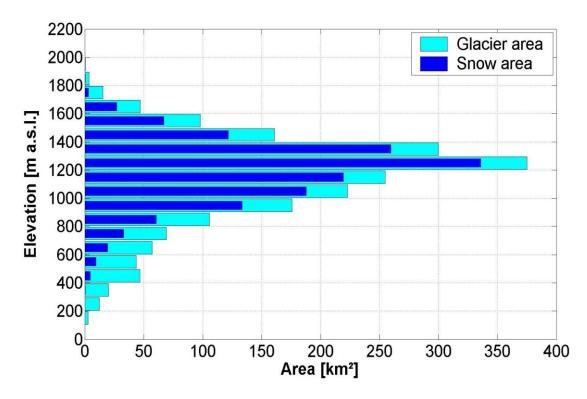
Figure 4.9: Area altitude distribution of the late summer snow area derived by the standard processing line from Landsat 7 ETM+ scene of 12/08/2001, using the threshold 0.48, and the area altitude distribution of the total glacier area of Harding Icefield, derived from USGS DEM. Areas are grouped into 100 m elevation intervals.

For the snow area classification on the Landsat 7 ETM+ scene of 09 August 2000, showing the Grewingk-Yalik Glacier Complex, a threshold of 0.31 is applied. The resulting late summer snow area is about 315 km², resulting in a snow area ratio of 0.69 with a total glacier area of about 459 km². Also for the glaciers on and around the Grewingk-Yalik Glacier Complex, Giffen et al. (2007b) reported a smaller total glacier area of 424.32 km² for the year 2000. As for the Harding Icefield, it is not obvious, which glaciers are included in this area calculation. As the investigations of the late summer snow area in this study are based on the glacier outlines mapped from a Landsat scene of 2009 within the GlobGlacier project, the retrieved late summer snow areas are related to the area of these glacier outlines.

The main snow areas are at elevations between about 900 m a.s.l. and 1200 m a.s.l., where also the main glacier areas can be found. The lowest snow covered areas are between about 400 m a.s.l. and 500 m a.s.l., about 200 m to 300 m above the lowest glacier elevation. Different from the Sargent and the Harding Icefield, there are no tidewater glaciers in the Grewingk-Yalik Glacier Complex. The dominant glacier form in this region is the valley glacier, terminating on land or in lakes (Giffen et al., 2007). Resulting outlines of the late summer snow and of the glaciers on the Grewingk-Yalik

71

Glacier Complex are presented in Figure 4.10, and the associated area altitude distribution is shown in Figure 4.11.
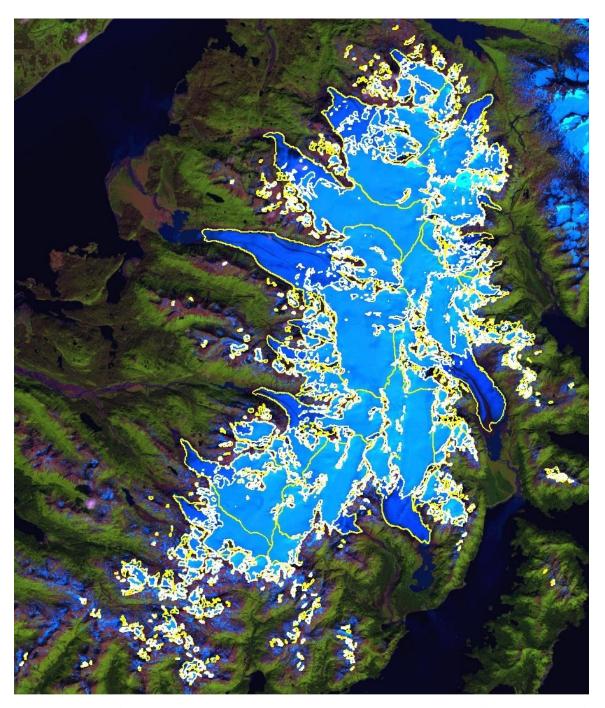
Figure 4.10: Outlines of late summer snow areas (white) on the glaciers (yellow) of Grewingk-Yalik Glacier Complex and surrounding glaciers, derived from Landsat 7 ETM+ scene of 09 August 2000 (Path 069 / Row 018). The applied threshold is 0.31. The DEM of USGS is used for the processing line.
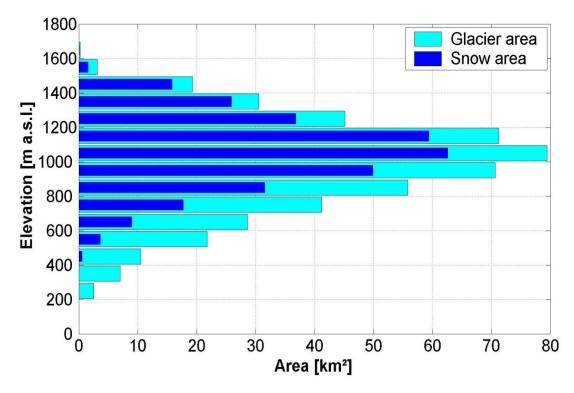
Figure 4.11: Area altitude distribution of the late summer snow area derived by the standard processing line from Landsat 7 ETM+ scene of 09/08/2000, using the threshold 0.31, and the area altitude distribution of the total glacier area of the Grewingk-Yalik Glacier Complex, derived from USGS DEM. Areas are grouped into 100 m elevation intervals.

4.2.2 Austria: Ötztal Alps and Stubai Alps (2000-09-15)

The study site Ötztal Alps (Austrian section) is located north of the main alpine ridge, close to the border to Italy. The Ötztal valley is one of the most arid valleys in the European Alps. A meteorological station is located in Obergurgl (46°52'N, 11°02'E, 1938 m a.s.l.), a village in the southern part of the Ötztal valley. At this station, meteorological observations and measurements are available since the 1950s. Based on daily mean temperatures measured between 1971 and 2000, a mean annual temperature of 2.2°C is derived for this weather station. For the same period and the same location, a mean annual precipitation rate of about 820 mm was measured. On other weather stations in this valley, the annual precipitation rate is even less than 700 mm when the high surrounding mountains form a natural barrier. These data and more detailed information on climatological data in Austria are published at the homepage of the Zentralanstalt für Meteorologie und Geodynamik (http://www.zamg.ac.at/fix/klima/oe71-00/klima2000/klimadaten_oesterreich_1971_frame1.htm).

More than 200 glaciers are located in the Ötztal Alps, covering in total more than 157 km². Glacier elevations range between about 2100 m a.s.l., and 3800 m a.s.l., with main parts of the glacier areas located between about 2800 m a.s.l. and 3400 m a.s.l. (Figure 4.14).

Most of the glaciers in the Ötztal Alps have a dominant north orientation, which is clearly represented by the number of glaciers with a northern aspect, as well as by the total glacier area with a dominant northern aspect. Only a few glaciers are orientated to the south and southwest, and the associated glacier area is negligible in the analysed data set, because glaciers with these orientations extend to the south of the main Alpine ridge (Italy). The amount of glaciers with the dominant aspect to the west, southeast, and east, respectively, is about equal, but the glacier areas with a dominant west orientation are significantly smaller compared to the glaciers with the main aspect to the east and south east (Figure 4.12, upper graphics).

Number of glaciers	Glacier area
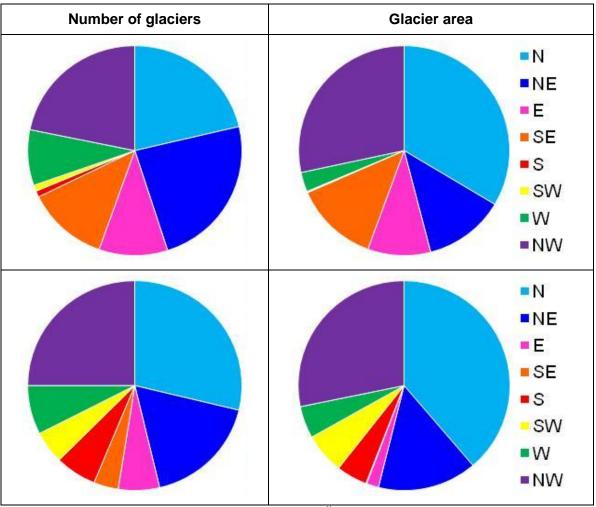
Figure 4.12: Main aspects of the glaciers in the Ötztal (upper graphics) and Stubai (lower graphics) Alps, Austria. The left graphic shows the main glacier aspects in dependence of the number of glaciers, the right graphic shows the main glacier aspects in dependence of the glacier area.

The second study region in the Austrian Alps, the Stubai Alps, is located north east of the Ötztal Alps. Most of the glaciers in the Stubai Alps are significantly smaller than these located in the Ötztal Alps. In 1985, the 117 glaciers in the Stubai Alps covered an area of

about 62.28 km² (Schicker, 2006). Based on ASTER scenes of 2003, for 88 of these glaciers the outlines were manually mapped. 14 glaciers disappeared between 1985 and 2003, and several glaciers were hidden by clouds on these ASTER scenes. The resulting area for the mapped 88 glaciers in 2003 covers about 36.35 km². This area is used as reference glacier area for most of the further investigations in the Stubai Alps in this study. In Section 5.2.2, the investigations of the late summer snow areas derived from Landsat images of 1985 and 1986 are related to the glacier area extents of both years 1985 and 2003. The Stubai Alps are in general lower than the Ötztal Alps, but the main glacier areas can be found at similar elevations, between about 2800 m a.s.l. and 3300 m a.s.l.. The elevation range where glaciers can be found in the Stubai Alps extends only between about 2500 m a.s.l. and 3500 m a.s.l. (Figure 4.15). Similar to the Ötztal Alps, the major part of the glaciers are orientated to the north, northeast, and northwest. The remaining glaciers in the Stubai Alps have the dominant aspect in all other directions (Figure 4.12, lower graphics).

A scene of 15 September 2000 is selected for the case studies for these study areas, as both regions are covered by one Landsat scene (Path 193 / Row 027). A national DEM with 10 m resolution is available for Austria and was used for the processing line and for the retrieval of topographic information on the glacier and the snow areas. Glaciers located in close vicinity to the Ötztal and the Stubai Alps, but on the Italian side, are investigated during the main processing line, but are not used here for further studies, and are thus not presented here in detail. Nevertheless, Figure 4.13 shows not only the glacier outlines and the late summer snow areas of Stubai and Ötztal Alps derived by applying the threshold 0.47, but also of the glaciers in Italy.

Glacier outlines of both regions in Austria were mapped by members of the Institute for Meteorology and Geophysics (IMGI) at University of Innsbruck, Austria. The glacier outlines of the Stubai Alps for the years 1985 and 2003 are online available via the GLIMS data base. The inventory of Ötztal Alps for the year 1997 was kindly made available for this study by A. Lambrecht of IMGI, University of Innsbruck, Austria (Lambrecht and Kuhn, 2007). An update of this inventory (Abermann et al., 2009) is currently available at the homepage of the Institute of Meteorology and Geophysics, University of Innsbruck, Austria, (http://imgi.uibk.ac.at/iceclim/glacierinventory), and is planned to be made available also via the GLIMS data base (personal communication, M. Kuhn, 2010).
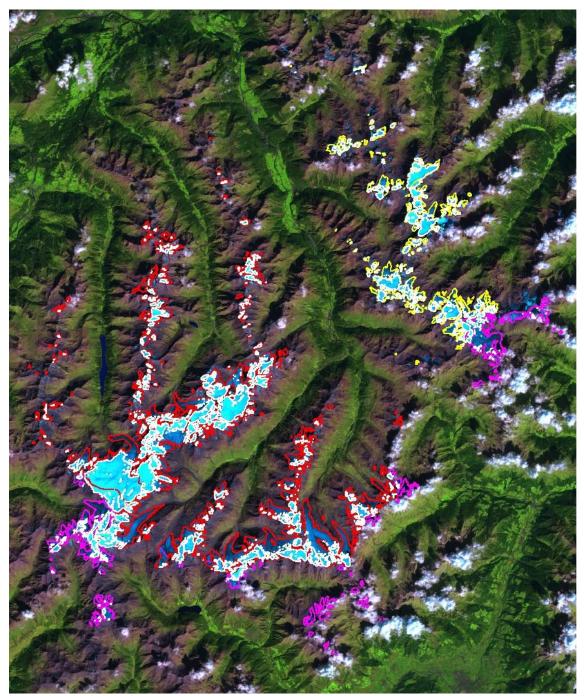
Figure 4.13: Outlines of late summer snow areas (white) on glaciers of Stubai (yellow), and Ötztal Alps (red) at the Austrian side, and on glaciers (pink) in Italy, derived from Landsat 7 ETM+ scene of 15 September 2000. The applied threshold is 0.47. The national DEMs of Austria and South Tyrol, Italy, are used for the processing line.

The resulting late summer snow area in the Ötztal Alps derived from the Landsat 7 ETM+ scene of 15 September 2000 covers about 61 km², which corresponds to a late summer snow area ratio of 0.39. The minimum elevation of the late summer snow area is at about 2700 m a.s.l., about 600 m above the lowest glacier area. The main snow areas are between 3100 m a.s.l. and 3300 m a.s.l. elevation zones, where also large glacier areas are

located. Above 3200 m a.s.l., the late summer snow area covers more than half of the glacier area in each elevation interval (Figure 4.14).

On the glaciers in the Stubai Alps, the resulting late summer snow area covers about 18 km², corresponding to a late summer snow area ratio of 0.49. The minimum snow elevation is also between 2700 m a.s.l. and 2800 m a.s.l., with the main snow areas between 3000 m a.s.l. and 3200 m a.s.l., where the largest parts of the glacier areas can be found. Comparable to the Ötztal Alps, the snow areas above 3000 m a.s.l. cover more than 50% of the associated glacier area in the corresponding elevation interval (Figure 4.15). Table 4.4 summarizes the main parameters and results of the case studies in the selected regions in Austria.

Region	Image acquisition date	Applied threshold	Total glacier area [km²]	Total late summer snow area [km²]	LSSAR
Ötztal Alps	15/09/2000	0.47	157.40	61.07	0.39
Stubai Alps	15/09/2000	0.47	36.35	17.72	0.49

Table 4.4: Summary of the results derived for the case studies on glaciers in the selected regions in Austria.
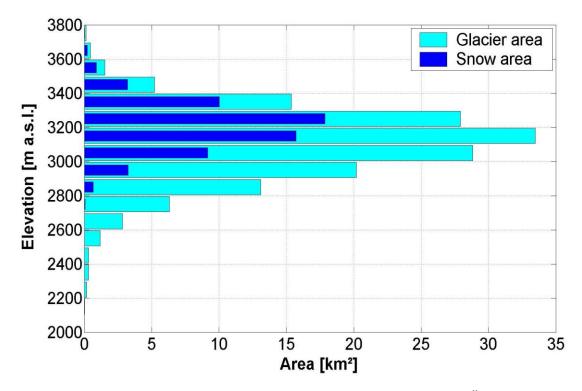
Figure 4.14: Area altitude distribution of the glaciers and snow areas in the Ötztal Alps, derived from the Landsat 7 ETM+ scene of 2000-09-15 applying the threshold 0.47 and using the national DEM for the processing line. Areas are grouped into 100 m elevation intervals.
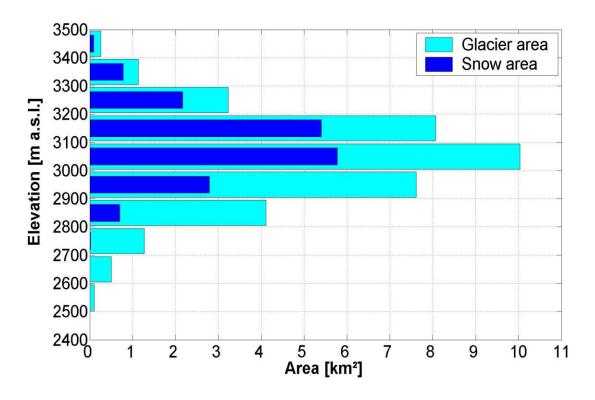
Figure 4.15: Area altitude distribution of the glaciers and snow areas in the Stubai Alps, derived from the Landsat 7 ETM+ scene of 2000-09-15 applying the threshold 0.47 and using the national DEM for the processing line. Areas are grouped into 100 m elevation intervals.

4.2.3 Canadian Arctic: Barnes Icecap (2001-08-08)

The Barnes Icecap (70°N, 73°W) is located on the highland of the fifth largest island in the world, the Baffin Island, which belongs to the Canadian Arctic. About 37000 km² of the total island area (305000 km²) are covered by glaciers and ice caps.

The Baffin Island is located within an Arctic climate zone, characterized by long and dark winters without any solar radiation, but also long days during summer. Due to the high albedo of the vast areas of snow and ice in the Arctic, the amount of absorption of solar radiation is low even during summer (ACIA, 2005). The distribution of precipitation amounts in the Arctic is still an open question. The Barnes Icecap is located approximately in the centre of Baffin Island, and is thus less affected by the maritime influences as the glaciers located along the coast.

The Barnes Icecap covers an area of about 5900 km², and ranges between about 300 m a.s.l. and 11124 m a.s.l. at the north-western dome of the icecap (Andrews et al., 2002). For this case study, a Landsat 7 ETM+ scene of 08 August 2001 is used (Path 025 / Row 011), although the icefield is partly covered by clouds. As the clouds are only water clouds over pure ice, misclassifications of clouds as snow are limited to a few pixels. The icefield is covered by two Landsat stripes, Path 025 / Row 011, and Path 024 / Row 011.

Due to the large area and the relatively flat plateau on the icecap, the GETASSE DEM was used for the main processing line, and also for the retrieval of topographic information of the icefield and the resulting late summer snow areas. Glacier outlines used for the case study were mapped during the GlobGlacier project.
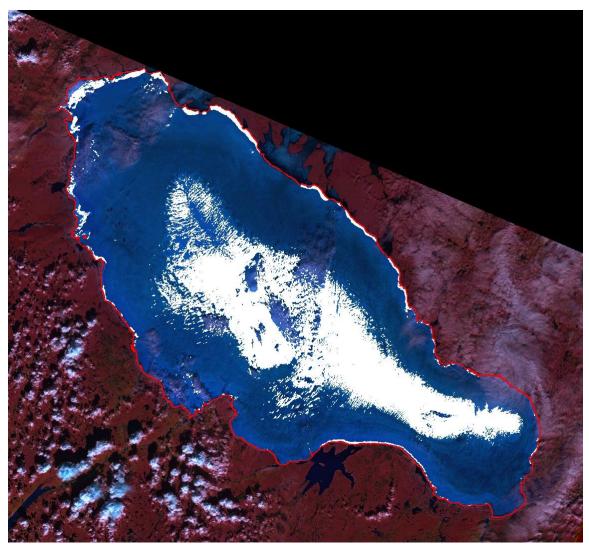
Figure 4.16: Snow areas (white) on Barnes Icecap (outline in red), derived from a Landsat 7 ETM+ scene of 08 August 2001. The applied threshold is 0.26. The GETASSE DEM is used for the processing line.

A threshold of 0.26 is applied, resulting in about 904 km² snow covered area (Figure 4.16). Setting this snow covered area in relation to the total glacier area results in a late summer snow area ratio of 0.15. The main snow areas are between 800 m a.s.l. and 1000 m a.s.l., and a few areas classified as snow are at lower elevations, at the margin all around the icecap. The area altitude distribution of the derived late summer snow area and the total icecap is illustrated in Figure 4.17.
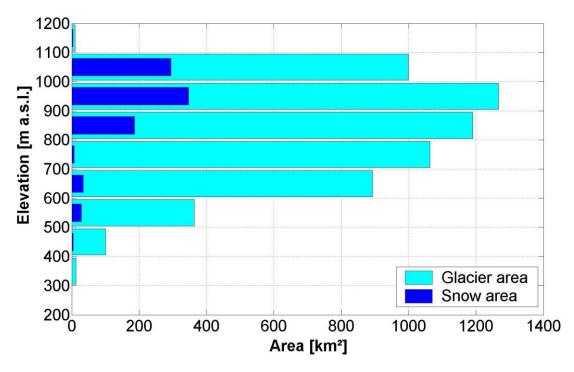
Figure 4.17: Area altitude distribution of late summer snow area and total glacier area of the Barnes Icecap, derived from the GETASSE DEM and the Landsat image of 08 August 2001 using the threshold 0.26 for glacier facies classification. Areas are grouped into 100 m elevation intervals.

4.2.4 Chile: North Patagonian Icefield (2000-03-08)

The North Patagonian Icefield (NPI) is located in the southern part of Chile, South America, along the Chilean coast, centred at about 47,0°S and 73,5°W. In the late 1980's, the reported area of the icefield was about 4200 km², feeding 28 outlet glaciers (Aniya, 1988). For this study, an updated glacier inventory of the NPI, mapped based on data of the year 2001 by members of the University of Chile, and made online available via the GLIMS data base, is used. The area covered by these outlines is about 4138 km². All further investigations in this study related to the NPI are referring to this new glacier area. The main ice area on the NPI is located between 1100 m a.s.l. and 1500 m a.s.l., but several peaks reach much higher elevations. The highest peak on the NPI is the Monte San Valentin with 3910 m a.s.l..

The climate is dominated by strong westerly winds, driven by the sub polar troughs around Antarctica. This belt of low pressure systems transports cold and moist air to the west wind zone, with the Andes forming the only but massive land barrier. This results in frequent precipitation events on the west coast of southern South America all around the year, and large precipitation amounts, often in form of snow on higher elevations (Bippus, 2007).

Regarding the number of glaciers, more than a quarter of all glaciers on the NPI are orientated to the east. The other aspects are equally represented (Figure 4.18). Regarding the glacier area, about half of the glacier area is west orientated, which is mainly driven by the both largest glaciers on the NPI, the San Quintin and the San Rafael glacier. Almost a quarter of the total glacier area has a dominant south west aspect. The remaining glacier areas are mainly north east or east orientated. Only a minor part of the total glacier area has another main aspect.
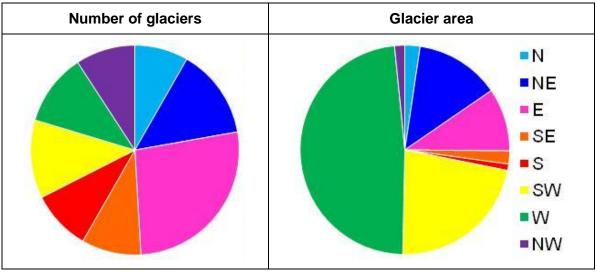
Figure 4.18: Main aspect distribution of the glaciers on the North Patagonia Icefield, Chile, mapped based on data of 2001. The left graphic shows the main glacier aspects in dependence of the number of glaciers, the right graphic shows the main glacier aspects in dependence of the glacier area.

For this case study of the North Patagonian Icefield (NPI), Landsat 7 ETM+ imagery of 08 March 2000 was used. To cover the total icefield, two neighboured Landsat scenes have to be merged, Path 232 / Row 092 and Row 093 (Figure 4.19). The DEM of SRTM covers the total icefield and is selected for the main processing line and for the retrieval of topographic information on the icefield and the derived snow areas, as the ASTER GDEM partly showed irregularities on the icefield.

Figure 4.20 shows the area altitude distribution of the glacier area of the North Patagonian Icefield, as well as of the late summer snow areas derived from the Landsat 7 ETM+ scenes of 08 March 2000 using the threshold 0.54 and the DEM of SRTM for the processing of glacier facies. The shown areas extend over 100 m elevation intervals. The total late summer snow area covers about 1178 km². The associated late summer snow area ratio for the total icefield is 0.45.
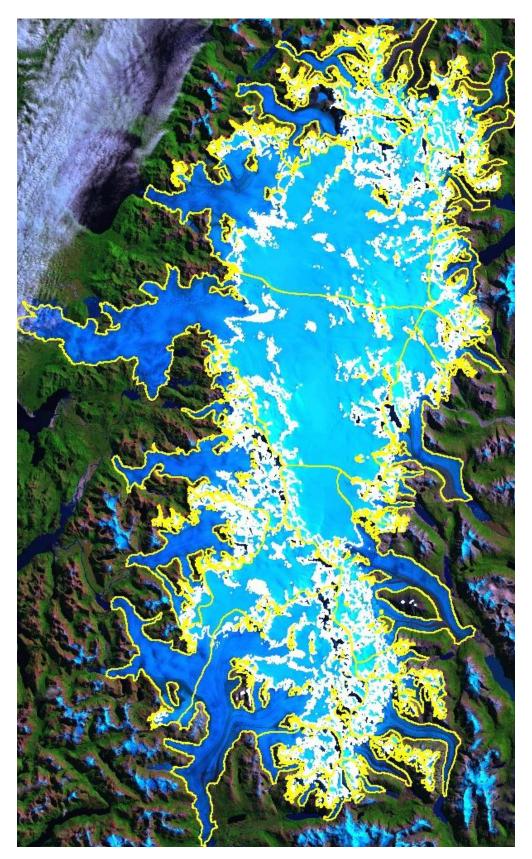
Figure 4.19: Outlines (white) of late summer snow areas (TH=0.54) on the North Patagonian Icefield, Chile, retrieved from topographically corrected near infrared band 4 of 2 merged Landsat 7 ETM+ scenes of 08 March 2000 and glacier outlines (yellow) of 2001 (GLIMS) on the Landsat RGB 543 composite. The DEM of SRTM is used for the processing line.
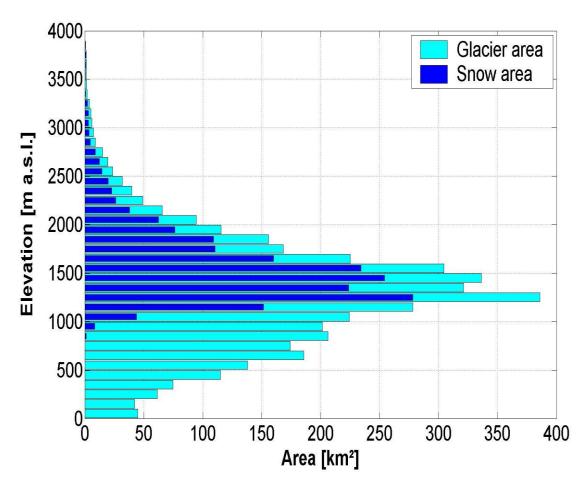
Figure 4.20: Area altitude distribution of the glacier and snow areas on the North Patagonian Icefield, based on the DEM of SRTM. For the classification of glacier facies from the Landsat 7 ETM+ scene of 08 March 2000, the threshold 0.54 is applied. Areas are grouped into 100 m elevation intervals.

4.2.5 Greenland: Flade Isblink (2001-07-03)

The icecap Flade Isblink is located on a north-eastern peninsula of Greenland, at about 82°N, 16°W. It covers an area of about 9087 km². Altitudes of Flade Isblink derived from the INSAR DEM vary between sea level (0 m a.s.l.) and 1425 m a.s.l. on the top of the icecap. Flade Isblink is in the high Arctic, and is thus influenced by the Arctic climate. Due to the high reflectivity of snow and ice, the absorption of solar radiation is relatively low. Temperatures are usually far below 0°C all around the year, but a general warming has been observed during the last decades (ACIA, 2005).

The glacier outlines of Flade Isblink are mapped during GlobGlacier based on the same Landsat 7 ETM+ scene used in this study (Path 013 / Row 001) of 03 July 2001. Unfortunately, this is the only available Landsat 7 ETM+ scene meeting the requirements described in section 3.2.1, and Landsat 5 TM does not cover these high latitudes.
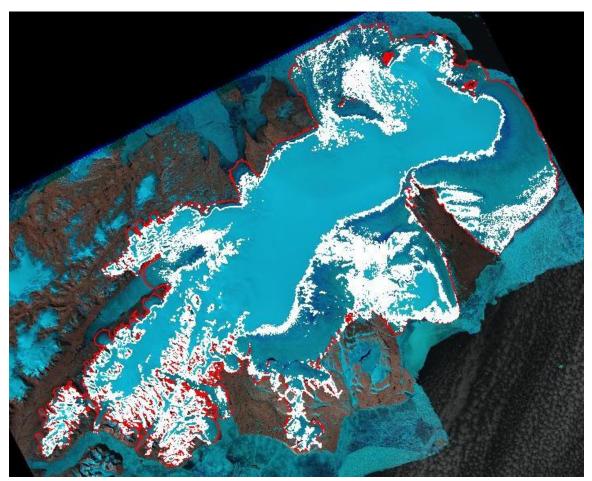
Figure 4.21: Outlines of summer snow areas (white) on the icecap Flade Isblink (outline in red), derived from Landsat 7 ETM+ scene of 2001-07-03. The applied threshold is 0.55. The Viewfinder DEM is used for the processing line.

For the processing line, the Viewfinder DEM is used. A threshold of 0.55 is applied, resulting in a snow covered area of about 4620 km² (Figure 4.21). Snow areas are distributed over all elevations, with the main area between 500 m a.s.l. and 600 m a.s.l., where also the main glacier area is found (Figure 4.22). At elevations higher than 500 m a.s.l. more than half of the glacier area per elevation interval is covered by snow, while below this altitude, where also large ice areas are found, the snow areas per elevation interval are significantly smaller than the glacier areas. The associated summer snow area ratio is 0.51. The derived snow covered area might be misclassified in some cases, as the glacier ice on the Flade Isblink is very clean, and thus has a high reflectivity similar to that of snow. The resulting values might thus be used with caution regarding further interpretations.

The INSAR DEM (Korona et al., 2009) was also made available by the GlobGlacier project, and was used for a comparative processing. But opposite to the Viewfinder DEM, the INSAR DEM does not cover the total icefield. The snow area derived from the INSAR processed image using the same threshold is about 4560 km², resulting in a

summer snow area ratio of 0.50. As the differences in the results are not large, the Viewfinder DEM is used to get overall results.
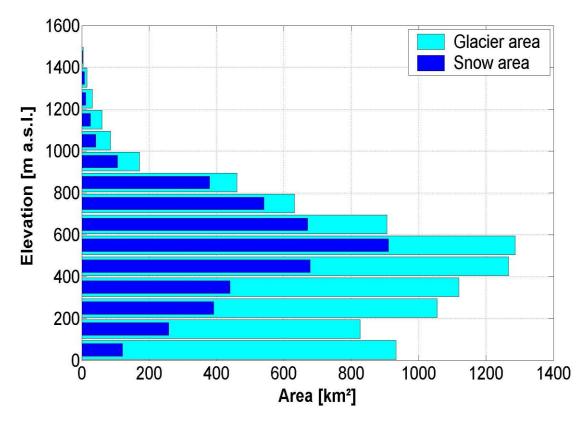
Figure 4.22: Area altitude distribution of summer snow and glacier area of Flade Isblink, derived from Landsat image of 03 July 2001 (applied threshold: 0.55) and the Viewfinder DEM. Areas are grouped into 100 m elevation intervals.

4.2.6 Nepal: Sagarmatha basin (2001-10-17)

The Sagarmatha basin is located in the Central Himalaya in Nepal, at about 27.9°N and 26.71°E. The basin contains several outlet glaciers flowing down from some of the world's highest peaks, including the Mount Everest.

The glaciers of the central Himalaya are exceptional compared to these of the other study regions, due to the influence of the summer and winter monsoons on the Himalaya ridge. The summer monsoon, also known as the rainy season, as it dominates the annual precipitation amount in this area, occurs during June to August in this region (Bhatt and Nakamura, 2005). But precipitation of the summer monsoon is greatest at low elevations, while precipitation of the winter monsoon in form of snow is more dominant at higher elevations (Singh et al., 1995). The months between winter and summer monsoon are usually relatively dry, but due to the high altitudes of the Himalayan peaks and glaciers, orographic precipitation in form of snow can occur all over the year. Currently, in situ

measurements of precipitation and detailed information on spatial and temporal distribution of precipitation in individual basins are still rare due to the difficult accessibility of most areas in the Himalaya.

The Sagarmatha basin is orientated to the south. This is clearly represented by the glacier aspect regarding the glacier area, and the number of glaciers. About half of all glaciers in the basin have a dominant southern component in the flow direction, covering about 75 % of the total glacier area. Regarding the number of glaciers, all other aspects are represented in an almost equal distribution, but the associated glacier areas are significantly smaller (Figure 4.23).
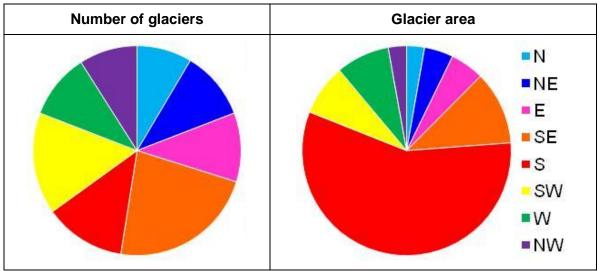
Figure 4.23: Main aspect distribution of the glaciers in the Sagarmatha basin, Nepal. The left graphic shows the main glacier aspects in dependence of the number of glaciers, the right graphic shows the main glacier aspects in dependence of the glacier area.

A Landsat 7 ETM+ scene of 17 October 2001 (Path 140 / Row 041) is used for the case study on the glaciers in the Sagarmatha basin, Nepal (Figure 4.24). The Viewfinder DEM is used for the main processing line and for the retrieval of topographic information on the glaciers and the snow areas. Glacier outlines are derived from the ICIMOD homepage (http://www.icimod.org). The investigated glaciers in the Sagarmatha basin are located between about 4260 m a.s.l. and 8230 m a.s.l. and cover an area of about 355 km². The snow covered area derived from this scene by applying a threshold of 0.41 is 116 km², ranging between about 4700 m a.s.l. and 8200 m a.s.l. (Figure 4.25). This results in a late summer snow area ratio of 0.33.

The main snow area is not – as in all other study regions – located in the elevation zones of the main glacier area, but rather in higher elevations. This is mainly caused by the shape of Himalayan glaciers, characterized by long glacier tongues, which are often covered by surface moraines and debris.
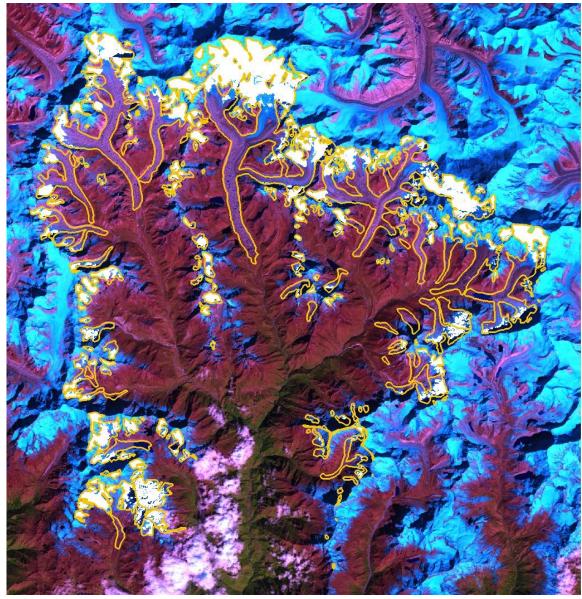
Figure 4.24: Late summer snow areas (white) on glaciers (orange) in the Sagarmatha Basin, Nepal, derived from Landsat 7 ETM+ scene of 17 October 2001. The applied threshold is 0.41. The Viewfinder DEM is used for the processing line.

In cast shadowed areas, on this scene on north and east facing slopes, the classification of snow and ice is not possible due to the low reflectivity in general. Based on the elevations of cast shadowed areas and regarding the general pattern of the snow and ice area distribution, large parts of these areas might be snow covered. Thus, the retrieved snow area may underestimate the real snow area in these regions. An increase of the total snow covered area by about 5 km² would result in an increase of the late summer snow area ratio by about 0.01, and about 10 km² additional snow covered area would result in an increase of the late summer snow area ratio by about 0.03 related to the currently derived value.
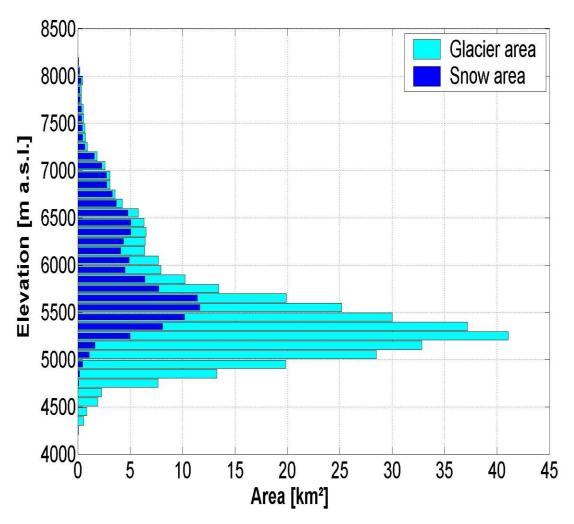
Figure 4.25: Area altitude distribution of the glacier and snow areas derived from the Viewfinder DEM and the Landsat 7 ETM+ scene of 17 October 2001 applying the threshold 0.41 for the glacier facies classification. Areas are grouped into 100 m elevation intervals.

4.2.7 Norway: Blåmannsisen and Svartisen (2001-08-20)

Blåmannsisen is located in northern Norway, at about 67.26°N and 16.08°E. The climate in this region can be already described as sub-Arctic continental. Glacier elevations range between about 600 m a.s.l. and 1700 m a.s.l., covering a total area of about 101 km².

A few kilometres southwest of Blåmannsisen, the region Svartisen is located, centred at about 66.6°N and 14.08°E. The Svartisen icecap is locate closer to the coast, and is thus influenced by sub-Arctic maritime climate conditions on the coastal side of the icefield, and by rather sub-Arctic continental climate conditions on the glaciers located further inland. This is also illustrated by the elevation range, the glaciers are located between about sea level with glaciers terminating in the sea, and 1600 m a.s.l.. A total area of about 532 km² is covered by all glaciers of Svartisen. A large amount of all glaciers in both regions has a dominant northern or eastern direction in the glacier aspect. These

aspect distributions are represented by both, the number of glaciers, and the total glacier area. Only a few glaciers are orientated to the south, southwest, and west (Figure 4.26).

Number of glaciers	Glacier area
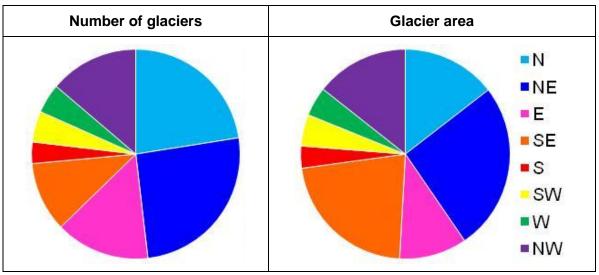
Figure 4.26: Main aspect distribution of the glaciers located in Blåmannsisen and Svartisen, Norway. Glacier outlines are derived from Landsat imagery of 1999. The left graphic shows the main glacier aspects in dependence of the number of glaciers, the right graphic shows the main glacier aspects in dependence of the glacier area.

A Landsat 7 ETM+ scene of 20 August 2001, Path 198 / Row 013, is used for this study on the glaciers in Blåmannsisen and Svartisen, which are both covered by this scene. A national DEM with 25 m resolution was kindly made available by L. M. Andreassen of NVE, Oslo, Norway. Glacier outlines, mapped based on Landsat imagery of 1999, are derived from the GLIMS data base.

A threshold of 0.53 is used for the retrieval of late summer snow and ice areas on the glaciers in both regions. In Blåmannsisen, this threshold results in about 36 km² snow covered area (Figure 4.27), corresponding to a LSSAR of 0.35. In Svartisen, about 110 km² are classified as late summer snow (Figure 4.28), resulting in a LSSAR of 0.21. In Svartisen, several glaciers are hidden by clouds on the selected Landsat scene. As there is no other Landsat image taken in 2000 or 2001 meeting the requirements, this scene is used nevertheless for the case study, but keeping in mind, that the derived snow areas on the glaciers in Svartisen underestimate the real late summer snow areas. Assuming that large parts of the glacier surfaces of east Svartisen, which are obscured by clouds are snow covered, an additional snow area between about 60 to 70 km² can be estimated. This results in an increase of the associated LSSAR about 0.12 to 0.14. The estimated LSSAR of Svartisen would thus be in the same range as the LSSAR derived for Blåmannsisen.

Maps of late summer snow and ice areas in the different study regions
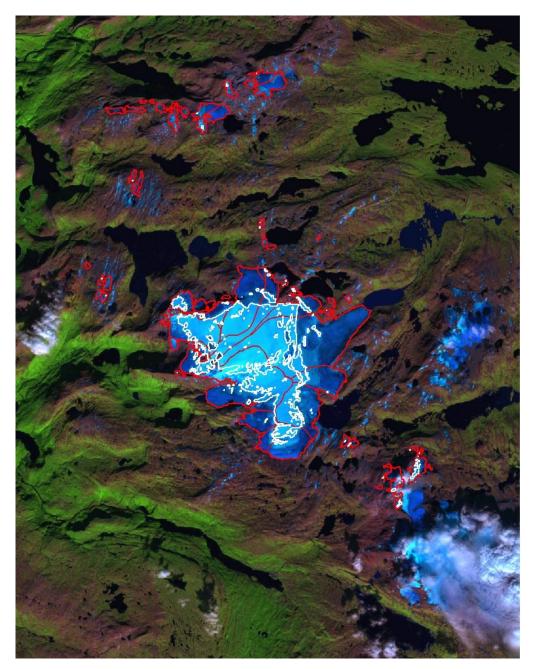
Figure 4.27: Outlines of the late summer snow areas (white) on glaciers of Blåmannsisen, Norway, derived from Landsat 7 ETM+ scene of 20 August 2001. The applied threshold is 0.53. The national DEM is used for the processing line.

Region	Image acquisition date	Applied threshold	Total glacier area [km²]	Total late summer snow area [km²]	LSSAR
Blåmannsisen	20/08/2001	0.53	101.34	35.72	0.35
Svartisen	20/08/2001	0.53	531.52	110.05	0.21

Table 4.5: Summary of the results derived for the case studies on the glaciers in the selected regions in Norway.
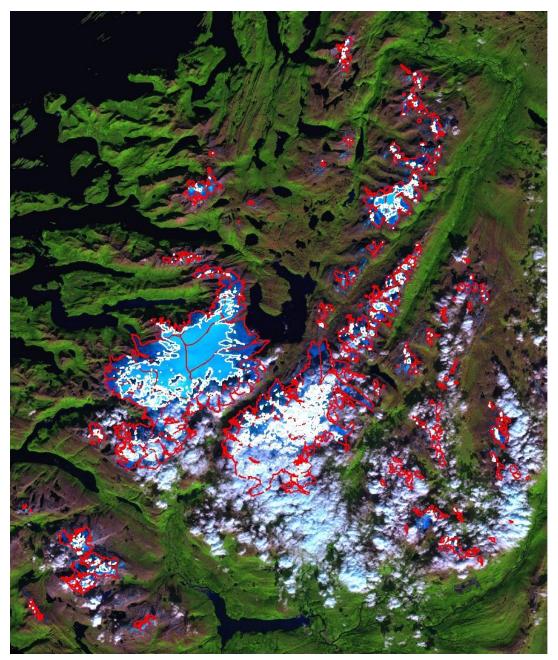
Figure 4.28: Outlines of the late summer snow areas (white) on the glaciers (red) of Svartisen and surrounding glaciers, derived from Landsat 7 ETM+ scene of 20 August 2001, applying the threshold 0.53. The national DEM is used for the processing line.

The associated area altitude distributions of the snow and glacier covered areas related to 100 m elevation intervals are illustrated in Figure 4.29 for glaciers in Blåmannsisen, and in Figure 4.30 for glaciers in Svartisen, respectively. The main derived late summer snow areas in both regions range between about 1100 m a.s.l. and 1300 m a.s.l., where also significant parts of the glacier areas are located in both regions. Table 4.5 summarizes the results for the selected regions in Norway.
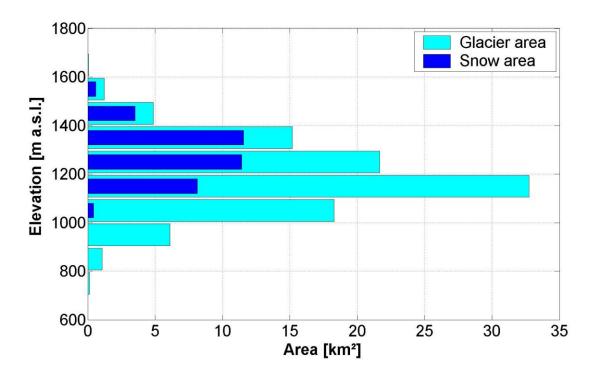
Figure 4.29: Area altitude distribution of summer snow areas and the glaciers of Blåmannsisen and surrounding glaciers, derived from national DEM and applying the threshold 0.53 on the Landsat 7 ETM+ scene of 20 August 2001. Areas are grouped into 100 m elevation intervals.
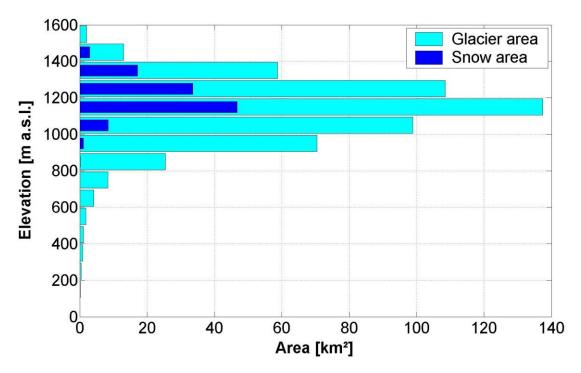
Figure 4.30: Area altitude distribution of snow and glacier areas of Svartisen and surrounding glaciers, derived from national DEM and Landsat 7 ETM+ scene of 20 August 2001 using the threshold 0.53. Areas are grouped into 100 m elevation intervals. Also snow areas on glaciers partly covered by clouds are included.

5. Analysis of spatial and temporal variations in snow area

5.1 Spatial variations of LSSIA extent in different glacier regions

Based on the investigations in the selected regions described in Chapter 4 the spatial distribution of the late summer snow and ice areas is investigated. The Landsat image acquisition dates in these regions range between 08th March 2000, for the North Patagonian Icefield in Chile, and 17th October 2001 for the Sagarmatha basin in Nepal. Further scenes of summer 2000 are taken in August over the Grewingk-Yalik Glacier Complex, Alaska, and in September over the Ötztal and Stubai Alps, Austria. In 2001, the earliest image acquisition date is the 03rd July, for the icecap Flade Isblink in Greenland. For the remaining five regions, Sargent and Harding Icefield in Alaska, Blåmannsisen and Svartisen in Norway, and for Barnes Icecap in the Canadian Arctic, satellite images acquired in August 2001 are available.

For some regions, the Landsat imagery was already acquired in high summer. In such cases, no late summer scenes were available. Nevertheless, some of these images were processed for two reasons: the first reason was to investigate, if the developed method is generally applicable to retrieve snow and ice areas on glaciers. The second reason was, that most of the glacier outlines used in this study were mapped based on satellite imagery acquired around the year 2000 +/- 3 years. Different to snow and ice areas on glaciers, which are sensitive to daily meteorological events, glacier areas have a longer response time to climatological changes, but annual changes in glacier areas are often negligible. The years 2000 and 2001 are used as reference to relate the retrieved late summer snow and ice areas to current glacier areas.

The comparison of late summer snow area ratios between different regions using data of a single year can be biased by the particular regional meteorological conditions during the mass balance year. Though detailed interpretation in terms of glacier behaviour is not possible, but this analysis is able to point out basic trends. On the other hand, the analysis of the pattern of LSSAR for glaciers within a given region is quite relevant also for data of a single year because it reveals important information on the impact of topography and glacier physiographic properties under similar meteorological conditions.

In order to avoid confusion, it is pointed out that the terminology late summer snow and ice area (LSSIA) is used throughout the discussion for the retrieved glacier surfaces, even if the Landsat scene used as data base was acquired in midsummer.

The highest overall LSSARs were found for the Harding Icefield (0.74) and the Grewingk-Yalik Glacier Complex (0.69), both located in the Kenai Mountains in Alaska. The lowest LSSAR was derived for Barnes Icecap (0.15) in the Canadian Arctic. The LSSAR obtained for the glaciers of Svartisen (0.21) underestimates the real snow area

extent due to cloud coverage over the eastern part of Svartisen. Assuming, that large parts at high elevation zones of this glacier area are also covered by snow, a LSSAR ranging between 0.33 and 0.35 can be estimated. This is in the same range as the LSSAR derived for the glaciers of Blåmannsisen. The Landsat images used for the investigations in the regions Harding and Sargent Icefield, Barnes Icecap, Svartisen and Blåmannsisen were acquired in August 2001 with a maximum delay of 9 days for the images of the Harding and the Sargent Icefield. Despite of the small delay in the image acquisition, the LSSAR of the glaciers on and around the Sargent Icefield, located northeast of the Harding Icefield, is significantly lower (0.54) compared to the LSSAR of the Harding Icefield.

Large differences in the LSSAR of glaciers in neighboured regions are also observed in other parts of the world. The LSSARs of the glaciers in the Stubai and Ötztal Alps in Austria differ by about 0.10, although the regions are in close vicinity, and were investigated by one satellite image using only one threshold.

On the icecap Flade Isblink more than half of the total glacier area is still snow covered in the beginning of July 2001. Decreasing the LSSAR of the icecap about 0.01 requires a reduction of the snow cover extent about 91 km². Considering that the Landsat image used for the investigation was acquired during the main melt season, it can be assumed that the LSSAR at the end of the summer 2001 was lower. Investigations of the snow cover extent on the Greenland Ice Sheet since the late 1970's described in the Arctic Climate Impact Assessment report (ACIA, 2005) indicate that the maximum melt extent on the ice sheet in the year 2001 was low compared to the maximum melt extents since the late 1970's, but this may be locally different for a small ice cap located at the northeast margin of the ice sheet.

Relating the accumulation area of a glacier (cf. Section 2.2.1) to its total area is defined as accumulation area ratio (AAR) (Meier and Post, 1962). The AAR can be used as a measure for the mass balance of a glacier. An AAR of 0.58 was reported as mean reference for glaciers in equilibrium by M. Dyurgerov et al. (2009) and Zemp et al. (2009) based on selected glaciers, where long-term mass balance measurements are available from the World Glacier Monitoring Service (WGMS). But the AAR for glaciers in equilibrium can vary with location and local climate. For Alpine glaciers, Gross et al. (1977) reported an AAR of 0.67 for glaciers in equilibrium. Meier and Post (1962) reported an AAR of 0.68 for the Harding Icefield in Alaska. For glaciers in the Himalaya, significantly lower values for the AAR of glaciers in equilibrium were reported. Kulkarni (1992) suggested an AAR of 0.44 for glaciers in equilibrium located in the western Himalaya, while Owen and Benn (2005) estimated an AAR of 0.54 for the Khumbu glacier, located in the investigated Sagarmatha basin in Nepal.

Assuming the LSSAR as proxy for the AAR, the retrieved values show in general a clear tendency to negative mass balances for the mean values of the selected total glacier regions, except for the glaciers of the Harding Icefield and the Grewingk-Yalik Glacier Complex in Alaska. But also for these glacier areas it can be assumed that the LSSAR

decreased further until the end of the ablation period, and the Landsat images were acquired around mid-August.

In the following discussion, the reported AARs ranging between 0.44 and 0.68 in different regions are used as reference LSSAR (LSSAR$_{ref}$), assuming an equilibrium state on the glaciers, although the equilibrium AAR of glaciers and icefields can be different, and there may also be systematic differences between different climate zones.

Region	Image acquisition date	Total glacier area [km²]	Applied threshold	LSSAR
Harding Icefield (HI), Alaska	12 August 2001	2012	0.48	0.74
Sargent Icefield (SI), Alaska	21 August 2001	2205	0.35	0.54
Grewingk-Yalik Glacier Complex, (GYGC) Alaska	09 August 2000	459	0.31	0.69
Stubai Alps (ST), Austria	15 September 2000	36	0.47	0.49
Ötztal Alps (OE), Austria	15 September 2000	157	0.47	0.39
Barnes Icecap (BI), Baffin Island, Canadian Arctic	08 August 2001	5899	0.26	0.15
North Patagonia Icefield (NPI), Chile	08 March 2000	4138	0.54	0.45
Flade Isblink (FI), Greenland	03 July 2001	9087	0.55	0.51
Sagarmatha (SA), Nepal	17 October 2001	355	0.41	0.33
Blåmannsisen (BL), Norway	20 August 2001	101	0.53	0.35
Svartisen (SV), Norway	20 August 2001	532	0.53	0.21

Table 5.1: Overview on the applied thresholds and the late summer snow area ratios derived from Landsat imagery of the summer seasons 2000/2001 for the glaciers in the selected regions.

Table 5.1 shows the applied thresholds and the derived late summer snow area ratios for the total glacier areas in the selected regions for the summer seasons 2000 and 2001 respectively, derived from Landsat imagery meeting the requirements described in Section 3.2.1. Figure 5.1 shows the locations of the glacier regions and the related LSSARs.

Additionally to the comparison of the overall LSSARs of the glaciers in the selected regions, the late summer snow areas on the individual glaciers were investigated, taking into account the individual glacier areas. The classes defined in Table 4.2 are used to

make the results for glaciers of different climate zones with similar areas comparable. Figure 5.2 shows a statistical overview on the glaciers and the LSSAR results for the summer 2000 and 2001, respectively, in the selected regions related to the glacier areas described by the glacier classes.

The retrieved late summer snow area ratios for glaciers smaller than 100 km² cover wide ranges in most of the selected regions. Also the mean LSSARs vary in most regions significantly with the glacier area, often with a tendency of higher values with increasing glacier sizes. Only for glaciers located in the Ötztal Alps in Austria and in the Sagarmatha basin in Nepal, the mean late summer snow area ratios are similar for all glacier classes.

In the Sagarmatha basin, glaciers of class 1 and 4 have a slightly lower mean LSSARs compared to glaciers of the size classes 2 and 3. Glaciers, belonging to the classes 2 and 3, have a mean LSSAR of approximately 0.33, which is also the LSSAR for all glaciers in the Sagarmatha basin.

The Harding and Sargent Icefield, and the North Patagonian Icefield have some glaciers larger than 100 km² (class 5). The late summer snow area ratios of these large glaciers are significantly higher, and the standard deviations are lower than for the smaller glaciers in these regions.

For the glaciers in the regions Harding and Sargent Icefield in Alaska, Svartisen and Blåmannsisen in Norway, and Stubai Alps in Austria, the mean LSSAR increases with increasing glacier size. The associated standard deviation is in most cases lower than 0.30. Only for glaciers smaller than 1 km² located at the Harding Icefield in Alaska the standard deviation of the LSSAR is slightly higher.

The polynomial curves described by the mean LSSARs and the standard deviations in dependence of the glacier class are different in all selected regions. The curve of the percentage of the number of glaciers is similar for the selected regions in Alaska, with a dominant number of glaciers of class 1, and decreasing percentages with increasing glacier area. In the selected regions in Nepal, Austria, and Norway, the highest percentage of the number of glaciers is observed for class 2, followed by glaciers of class 1, and further decreasing values with larger glacier areas. On the North Patagonian Icefield, small glaciers are merged into glacier groups by the analyst of the glacier outlines used in this study, resulting in no glacier outlines for glaciers belonging to class 1. Most of the investigated glaciers of the NPI belong to the glacier class 3, followed by glaciers of class 4. The numbers of smaller and larger glaciers are the same.
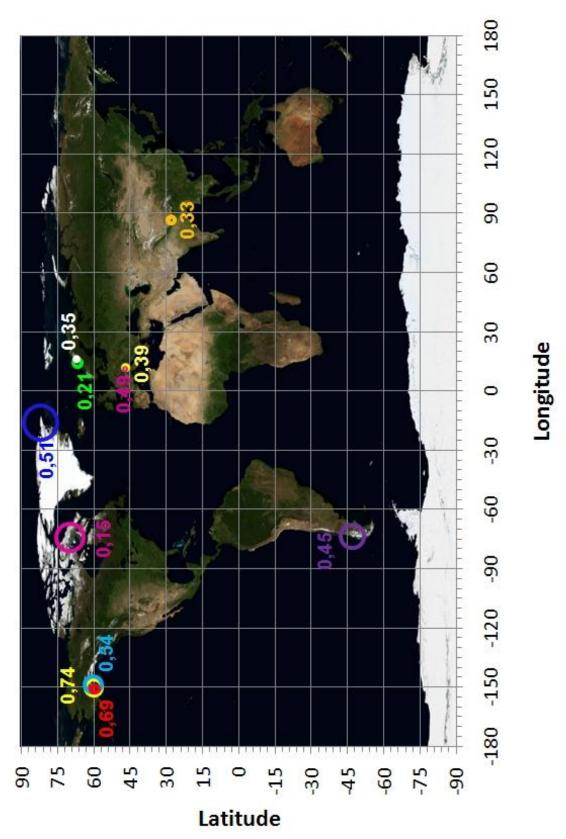
Figure 5.1: Coloured numbers are the late summer snow area ratios of the total glacier areas in the selected regions in 2000 and 2001, respectively. The sizes of the identically coloured circles indicate the total investigated glacier areas in the individual regions.

97
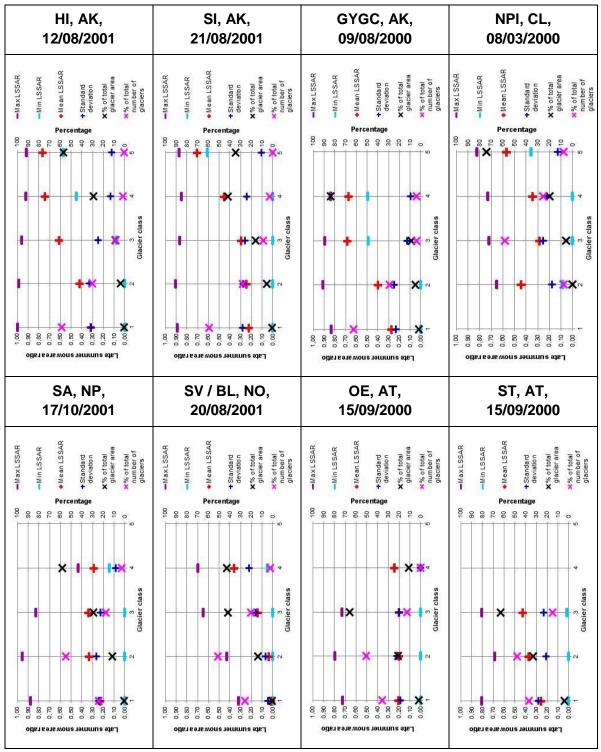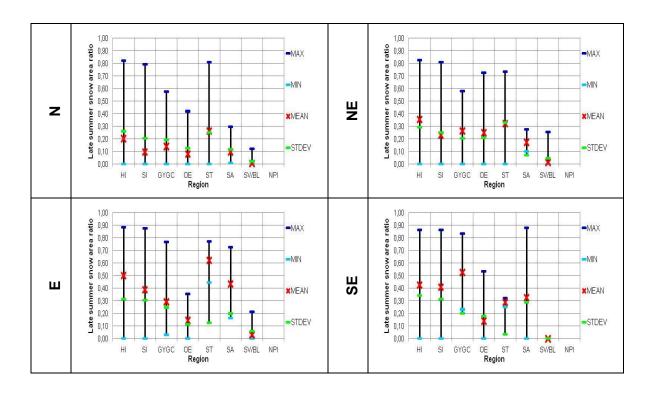
Figure 5.2: Maximum, minimum, mean late summer snow area ratios and associated standard deviation derived from Landsat data of 2000 and 2001, respectively, as well as the percentage of the total glacier area and of the number of glaciers per glacier class in the selected regions. The both icecaps Flade Isblink in Greenland and Barnes Icecap in the Canadian Arctic are excluded, because these icecaps are treated as single glaciers in this study, and the results are described in detail in the text. The data base for these graphics is presented in Appendix B.

The derived LSSARs in the selected regions were not only investigated in dependence of the glacier area, but additionally considering the glacier exposition. For glaciers with an area between 0.01 km² and 0.10 km², defined as glacier class 1, the mean LSSARs on north, northwest and west orientated glaciers in all regions show values ≤ 0.30, while the LSSARs of the individual glaciers cover a wide range (Figure 5.3). Glaciers of this class with a south or east component in the aspect in all regions have in most cases higher mean LSSARs, with also a wide range of the LSSAR values derived for individual glaciers. An exception is the only southwest orientated glacier of this class in the Ötztal Alps, Austria, where no snow remained on the glacier at the image acquisition date in the mid of September 2000. A reason for this difference between north and south facing glaciers in this year might be that the small south facing glaciers adapted faster to changing climate conditions than north facing glaciers.

Any of the LSSAR$_{ref}$ in the selected regions, assumed as measure for glaciers in equilibrium (M. Dyurgerov et al., 2009; Zemp et al., 2009; Gross et al., 1977; Kulkarni, 1992; Meier and Post, 1962) was reached by the mean LSSARs for the glaciers of class 1. But individual glaciers of all aspects in some of the regions have partly significantly higher LSSARs. In other cases, no snow remained on the glaciers at the image acquisition date, as previously mentioned for the example of the southwest orientated glacier in the Ötztal Alps in Austria. The same can be observed for south and southeast orientated glaciers in Svartisen / Blåmannsisen in Norway, and on west and northwest orientated glaciers in the Stubai Alps, Austria. The Stubai Alps in Austria have no southwest orientated glacier of this glacier class in 2003, when the glacier outlines were mapped based on ASTER data (Schicker, 2006).
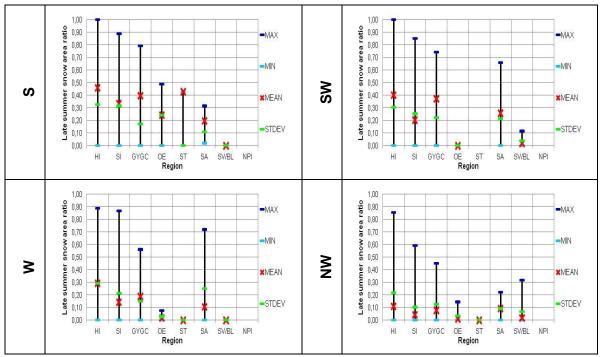
Figure 5.3: Mean, minimum, and maximum LSSAR as well as the standard deviation for glaciers of class 1 in all selected regions, considering the dominant glacier aspects.

For glaciers with an area between 0.10 km² and 1 km², belonging to class 2, only the northwest orientated glaciers in all regions have mean LSSARs lower than 0.30 (Figure 5.4). Compared to the mean LSSARs of northwest orientated glaciers of the class 1, the derived values for glaciers of class 2 with this aspect are in general slightly higher. For all other aspects, the mean LSSARs are partly significantly higher, but show strong variations for the individual expositions from region to region. Also no mean LSSAR values of 0.00 occur for this glacier class, although some of the mean LSSARs are very close to zero. On the other hand, for east, southeast, south, and southwest orientated glaciers of the Grewingk-Yalik Glacier Complex and additionally for northeast orientated glaciers of the Harding Icefield in Alaska, the mean LSSAR is partly significantly higher than the $LSSAR_{ref}$.

The lowest mean LSSARs of glaciers of class 1 and 2 for all aspects were found for the glaciers in Norway. For the glaciers in Norway belonging to class 1 and 2, a maximum LSSAR of 0.43 was derived for a southwest orientated glacier in the summer 2001. This is far below the maximum LSSAR of the glaciers of these classes in the other regions.
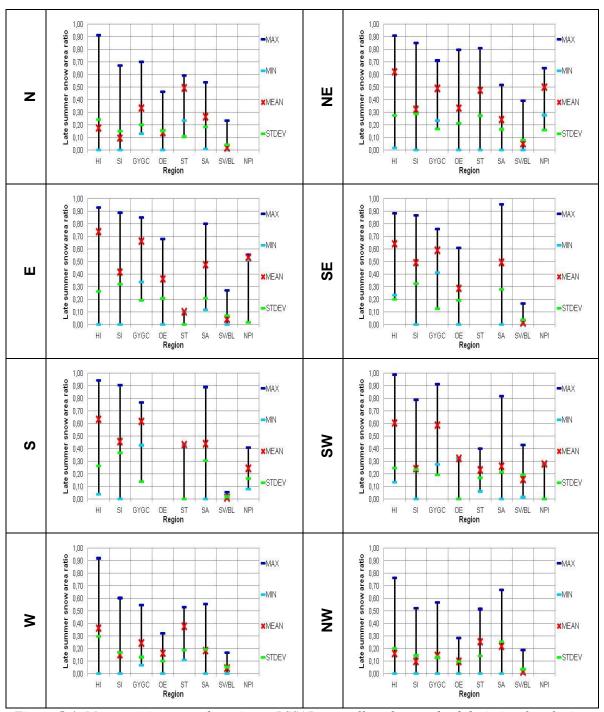
Figure 5.4: Mean, minimum, and maximum LSSAR, as well as the standard deviation for glaciers of class 2 in all selected regions, considering the dominant glacier aspects.

Of the glacier class 3 with an area between 1 km² and 10 km², only northeast and northwest orientated glaciers occur in all selected study regions. In the Austrian Alps the number of glaciers with areas larger than 1 km² is a minority. The Grewingk-Yalik Glacier Complex has no north orientated glacier belonging to this glacier class, and only one glacier with each, a northeast, south, southwest, and west orientation. The mean

LSSARs of east and southeast orientated glaciers are relatively high for the regions in Alaska, the Ötztal Alps in Austria, and Sagarmatha in Nepal.
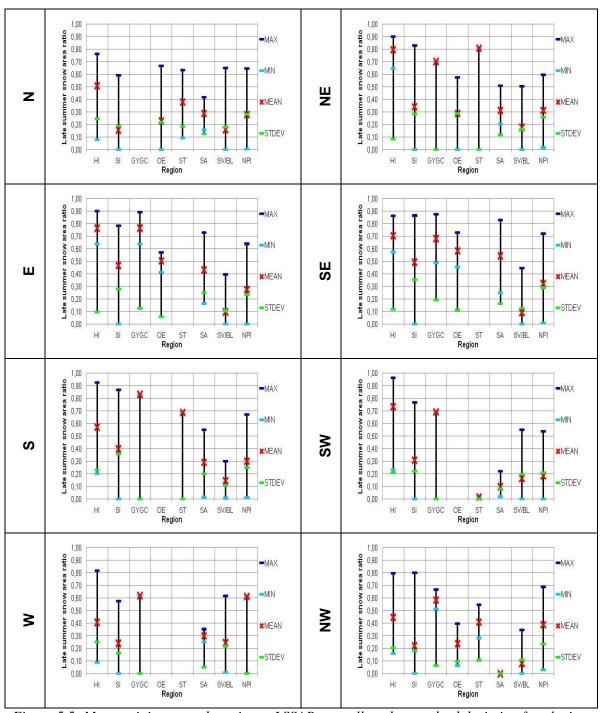
Figure 5.5: Mean, minimum, and maximum LSSAR, as well as the standard deviation for glaciers of class 3 in all selected regions, considering the dominant glacier aspects.

In the three neighboured regions in Alaska, the mean LSSAR for glaciers of all aspects are lowest for the glaciers of the Sargent Icefield, with partly significant differences. On the Sargent Icefield, on at least one glacier of each aspect, no snow remained at the image

acquisition date. This is different to the glaciers of the Harding Icefield and the Grewingk-Yalik Glacier Complex, where snow remained on all glaciers of this class. But some of the glaciers of the Sargent Icefield have very high LSSARs, meaning that large parts of these glaciers are still snow covered at the image acquisition date. On the southeast orientated Wolverine Glacier (60°24'N, 148°55'W) located on the Sargent Icefield, a LSSAR of 0.68 was derived from the Landsat scene of 2001. Van Beusekom et al. (2010) reported a specific annual mass balance of 0.45 m w.e. for the Wolverine Glacier in 2001, with a winter balance of 3.14 m w.e. and a summer balance of –2.69 m w.e..

In the Ötztal Alps, some north and northeast orientated glaciers of this glacier class had no snow remaining at the image acquisition date. But the range of the derived LSSARs is also largest for north orientated glaciers in this region. Nevertheless, the highest LSSAR, 0.73, is derived for a southeast orientated glacier.

For some glaciers in the Ötztal Alps belonging to this glacier class, long term mass balance measurements are available. Abermann et al. (2009) reported cumulative mass balances for three glaciers of this class referring to the cumulative mass balance since 1969, for the both southeast orientated glaciers Kesselwandferner (KWF) and Vernagtferner (VF), and the east orientated Hintereisferner (HEF). In 2000, the cumulative mass balances since 1969 of these glaciers were about – 2 m for KWF, about – 10 m for Vernagtferner, and about – 17 m for Hintereisferner. The LSSARs of these glaciers derived from the Landsat scene of 2000 are 0.73 for KWF, 0.46 for VF, and 0.41 for HEF, which represents in general the feature of the mass balances on the KWF and the VF, but not the strong difference in the mass balances of VF and HEF.

In the Stubai Alps, snow remained on all glaciers of this class, although the lowest LSSAR, derived for a southwest orientated glacier, is close to zero. The highest LSSAR was found for the only northeast orientated glacier of this class (0.81), followed by a significant difference for the only south orientated glacier of this class in this region with a LSSAR of 0.69. North and northwest orientated glaciers have mainly LSSARs lower than the LSSAR$_{ref}$.

The Norwegian glaciers of this class have higher mean LSSARs for all orientations than for smaller glaciers, with a maximum LSSAR of about 0.65 on a north orientated glacier. LSSARs higher than the LSSAR$_{ref}$ are only found for north and west orientated glaciers of this class in these two regions. But all aspects include glaciers where no snow remained at the image acquisition date.

On the NPI, the mean LSSARs are similar for glaciers with an east component in the orientation, and for north and south orientated glaciers, about 0.30 ± 0.02. Southwest orientated glaciers of the NPI have a mean LSSAR of 0.18, but the LSSARs of glaciers with this orientation range between 0.00 and 0.54. Northwest orientated glaciers of this glacier class on the NPI have higher mean LSSAR, about 0.39. But also for this orientation the LSSARs cover a broad range with values between 0.03 and 0.69. Only one

glacier with a west orientation occurs in this glacier class on the NPI, having a LSSAR of about 0.61, indicating, that this glacier is approximately in equilibrium at the image acquisition date.

Glaciers belonging to the glacier class 4 occur in all of the selected regions except in the Stubai Alps in Austria, but compared to the classes 1 to 3 the number of glaciers is significantly smaller. Except the Sargent Icefield and the North Patagonian Icefield, glaciers of this class occur only for selected aspects, partly with only a single glacier per exposition.

All but northwest orientated glaciers of the Harding Icefield in this glacier class have LSSARs higher than the LSSAR$_{ref}$, partly even a LSSAR above 0.90, indicating clearly positive mass balances on these glaciers at the image acquisition date. For the glaciers of the neighboured Sargent Icefield, the derived mean LSSARs are lower for all orientations. On some northeast, south, west, and northwest orientated glaciers no snow remained at the image acquisition date. But also several very high LSSARs are derived for north, northeast, and east orientated glaciers of the Sargent Icefield. South and west orientated glaciers of this class in this region have LSSARs indicating rather negative mass balances.

Also on the Grewingk-Yalik Glacier Complex all but one west orientated glacier have LSSARs close to or higher than the reference LSSAR$_{ref}$. The aspects northeast and southwest are not represented by glaciers, and the orientations north, south, and southeast are each represented by only one glacier of this class at the GYGC. The southeast orientated glacier has the highest LSSAR, followed by an east orientated glacier.

In the Ötztal Alps in Austria, only one north orientated glacier, the Gepatschferner, belongs to this glacier class. In mid of September 2000, the LSSAR on this glacier was 0.73, indicating a positive mass balance at this date.

In the Sagarmatha basin in Nepal, four south, and each one southeast and west orientated glaciers occur in this glacier class. All of these glaciers have LSSARs significantly lower than the LSSAR$_{ref}$, with the highest value (0.44) on a south orientated glacier, and the lowest LSSAR, 0.15, on the southeast orientated glacier.

In Norway, the derived LSSARs for three of 12 glaciers in this class are higher than the reference mean AAR for glaciers in equilibrium. Two of these glaciers are northwest orientated, and the third glacier is northeast orientated. For the northwest orientated Engabreen, an outlet glacier of the western part of Svartisen, a LSSAR of 0.59 is derived for the Landsat scene of 2001. As this scene was acquired on the 20th August, the ablation areas were not at a maximum, and the LSSARs at the end of summer were probably smaller. This is also in line with observations of Andreassen et al. (2005), who reported a significant mass loss on Norwegian glaciers since the beginning of the 21st century, especially for the years 2001 to 2003 due to low winter precipitation and high summer ablation.
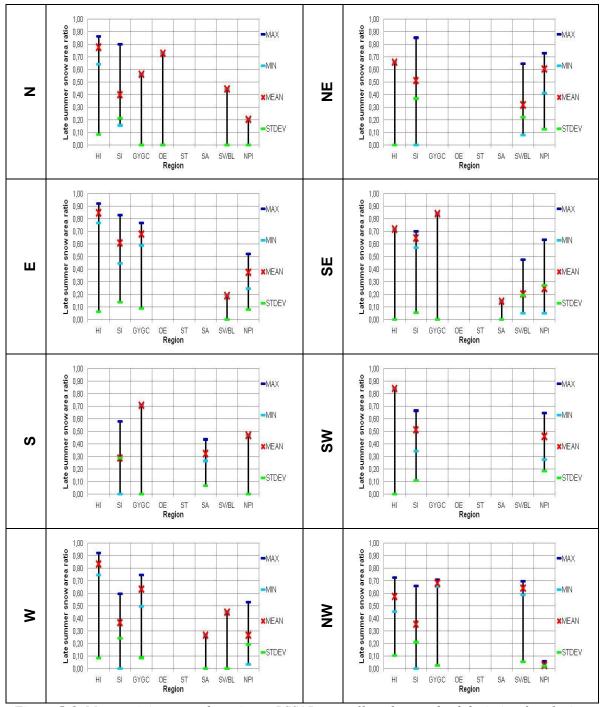
Figure 5.6: Mean, minimum, and maximum LSSAR, as well as the standard deviation for glaciers of class 4 in all selected regions, considering the dominant glacier aspects.

Glaciers belonging to class 5 in the selected regions occur only on the Harding and the Sargent Icefield in Alaska, and on the North Patagonian Icefield in Chile, so that statistical interpretation is not possible.

On the Harding Icefield, six glaciers have an area between 100 km² and 1000 km², described by the glacier class 5. All orientations except of northeast and south are

represented by glaciers of this class on the Harding Icefield. The LSSAR of these glaciers vary between 0.57 on the east orientated Bear Glacier, and 0.92 on the southeast orientated Northwestern Glacier and the northwest orientated glacier Harding Icefield.

Three of the four glacier of the Sargent Icefield belonging to glacier class 5 have a southern component in their aspect. The fourth glacier, the Chenega Glacier, which is also the largest glacier of this region, has an east orientation. On this glacier, the largest LSSAR (0.87) was found for the image acquisition date. For ´the southeast orientated Princeton Glacier a LSSAR of 0.72 was derived, and the other both large glaciers, the Excelsior Glacier and the Ellsworth Glacier each have a LSSAR of 0.61 on the 21 August 2001.

The LSSARs derived for the large glaciers in both regions, the Harding and the Sargent Icefield in Alaska indicate that the mass balances of these glaciers are at least close to equilibrium, and in most cases even positive at the image acquisition dates in August 2001.

The third region with glaciers belonging to glacier class 5 is the North Patagonian Icefield in Chile. Four of nine large glaciers are west orientated, and further three glaciers have a southwest orientation. The two other glaciers have northeast and east exposition, respectively. Both, the lowest and the highest LSSAR values for the image acquisition date on 08 March 2000 were found for two neighboured glaciers with west orientation. The lowest LSSAR, 0.36, was derived for the Gualas Glacier, and the highest LSSAR, 0.82, was derived for the San Rafael Glacier, which is also the only tidewater glacier on the North Patagonian Icefield and is located south of the Gualas Glacier (Aniya, 2007). The ice velocity at the glacier front is high so that the calving flux accounts for a significant part of the mass depletion. The two other west orientated glaciers of this class, the largest glacier of the NPI, the San Quintin Glacier, located south of the San Rafael Glacier, and the Benito Glacier, located south of the San Quintin Glacier, have LSSARs of 0.51 and 0.69, respectively. For the northeast orientated Colonia Glacier, a LSSAR of 0.54 was derived, and for the east orientated Nef Glacier a LSSAR of 0.50 was found for the image acquisition date. The LSSARs of the southwest orientated glaciers on the NPI range between 0.44 and 0.61 for the glacier HPN1, and the Acodado Glacier, respectively.

The results derived for the glaciers of the NPI indicate different behaviour of the mass balances of neighboured glaciers. . However, a clear interpretation of LSSAR in terms of mass balance is not possible for calving glaciers. Though the LSSAR of the San Rafael Glacier is high it is therefore unclear if the mass balance was positive. The low LSSARs of the Gualas Glacier and the HPN1 stand for significantly negative mass balances. Other glaciers, as for example the Colonia Glacier, have a LSSAR close to the AAR assumed for glaciers in equilibrium (0.58) (Dyurgerov et al., 2009). These results are also in line with glacier variations found by Aniya (2007) and reported for the glaciers of the NPI for several time intervals between 1944/45 and 2004/05.
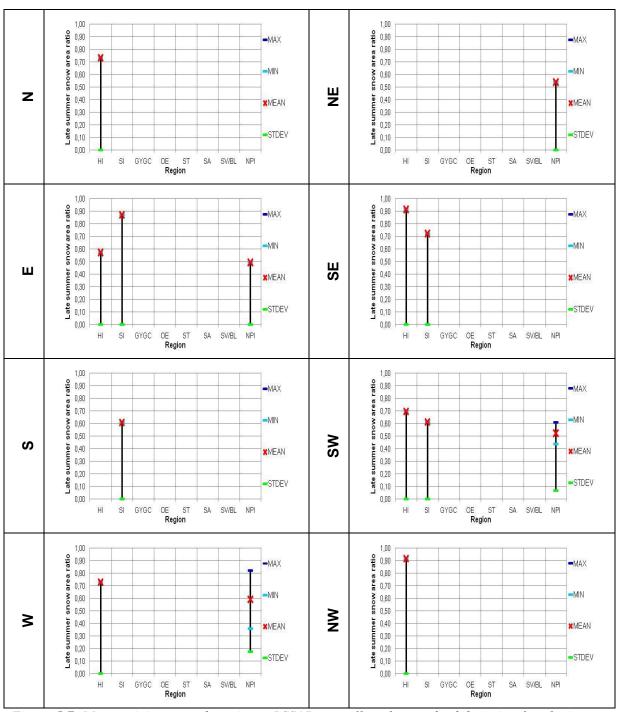
Figure 5.7: Mean, minimum, and maximum LSSAR, as well as the standard deviation for glaciers of class 5 in all selected regions, considering the dominant glacier aspects.

5.2 Temporal variations of LSSIA extent

For most of the selected regions, several Landsat images meeting the requirements described in Section 3.2.1 are available, and the late summer snow areas on glaciers are investigated for several years since the mid 1980's.

Time series have been calculated for 10 regions:

- Harding Icefield, Alaska

- Sargent Icefield, Alaska

- Grewingk-Yalik Glacier Complex, Alaska

- Stubai Alps, Austria

- Ötztal Alps, Austria

- Barnes Icecap, Canadian Arctic

- North Patagonian Icefield, Chile

- Sagarmatha, Nepal

- Blåmannsisen, Norway

- Svartisen, Norway

Since the mid of the 1980s, Landsat data of late summer are available for most of these regions. In the 1990's, the available Landsat data sets are limited, and only a few Landsat scenes of some of the selected regions meet the requirements (cf. Chapter 3.2).

In order to get a representative multi-annual data base for the investigation of snow and ice areas on glaciers, also some scenes acquired already in high summer were investigated. For simplification, during the following discussion the retrieved snow areas and the associated snow area ratios are in all cases denoted as late summer snow areas and late summer snow area ratios, respectively.

For some regions, several Landsat scenes meeting the requirements are available in a summer. These scenes were investigated in order to present the seasonal change of the late summer snow area extent on glaciers, and the overall results are shown in the discussion. Detailed studies on individual glaciers and area altitude distributions of the snow areas were only made based on the scene with the maximum extent of the ablation. For the North Patagonian Icefield in Chile and for the Ötztal Alps in Austria, some Landsat 7 ETM+ data with the SLC OFF mode were used for the investigation of late summer snow areas due to a lack of imagery meeting the requirements derived from Landsat 5 TM.

Table 5.2 summarizes the multi-annual acquisition dates of the Landsat images used for the retrieval of the late summer snow area ratios in the selected regions. Scenes of the Landsat 7 ETM+ with the SLC OFF mode are marked by SLC OFF in brackets. The selected regions in Austria and in Norway are each covered by one Landsat image.

YEAR	Sargent Icefield, AK	Harding Icefield, AK	Grewingk-Yalik Glacier Complex, AK	Ötztal / Stubai Alps, AT	Barnes Icecap, CA	Sagar-matha, NP	Svartisen / Blåmannsisen, NO	North Patagonian Icefield, CL
1984							09-30	
1985				08-13	07-28			03-07
1986	09-14	09-12	09-12	10-03				
1987								02-09
1988								
1989								
1990				08-03	08-18			
1991				08-30	07-20			
1992						09-22		
1993								
1994							07-31	
1995								
1996								
1997								
1998								
1999	09-26	09-08	09-08	09-13			08-15, 09-07, 10-02	
2000		08-09	08-09	09-15		10-30		03-08
2001	08-21	08-12			08-08	10-17	08-20	
2002	09-02	07-30	07-30			12-23	08-23	02-10
2003				07-30		01-24		05-20
2004				09-10 (SLC-OFF)		11-02		
2005	09-18			08-12 (SLC-OFF)		11-05		
2006	09-12	09-12		08-23, 09-24, 10-26			08-01, 08-26, 10-04	
2007		09-06	09-06					
2008								
2009	08-03	07-09	07-09	08-31		10-31		
2010					08-02, 08-09	01-19	08-05	02-16 (SLC-OFF), 03-04 (SLC-OFF)

Table 5.2: Overview on the acquisition dates (MM-DD) of Landsat imagery used for temporal investigation of the late summer snow / ice area extents in the selected regions.

The derived LSSARs of the glaciers of the Sargent Icefield in Alaska are in general lower than for the glaciers of the Harding Icefield, except in 1986, when the LSSAR of the Sargent Icefield was significantly higher. The LSSARs of the glaciers of the Grewingk-Yalik Glacier Complex of the late summers in 2000 and 2002 were similar to these of the Harding Icefield. In the other years, the LSSARs of the Harding Icefield were higher than these of the Grewingk-Yalik Glacier Complex, with the largest difference in 2009. In this year, the LSSAR of the Grewingk-Yalik Glacier Complex was also significantly lower than that derived for the glaciers of the Sargent Icefield, although the investigated scene showing the Sargent Icefield was acquired almost one month later than that one used for investigating the glaciers of the Harding Icefield and of the Grewingk-Yalik Glacier Complex.
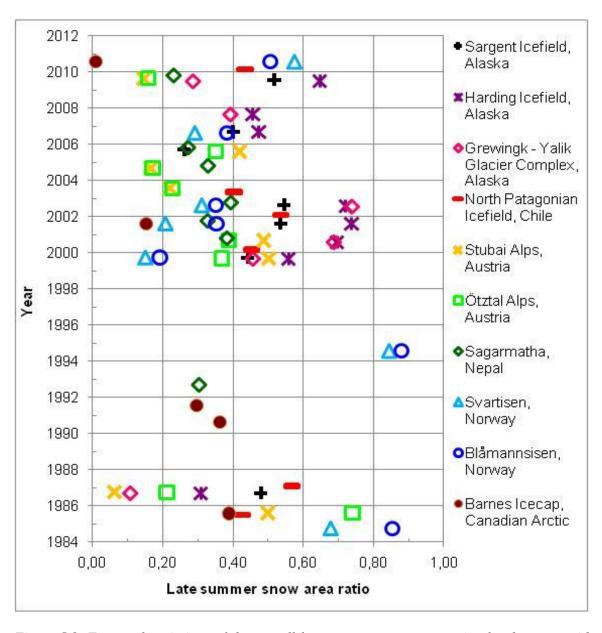
Figure 5.8: Temporal variations of the overall late summer snow area ratios for the years with available Landsat data in the selected study areas.

110

For the glaciers in the Austrian Alps, the derived LSSARs are similar in Stubai and Ötztal in the years 2003, 2004, and 2009. The investigated scene of 2003 was acquired already in July. The exceptionally warm temperatures in summer 2003 in the Alps resulting in significant snow melt on the Alpine glaciers occurred in the following months. In 1985 and 1986, the derived LSSARs of the Stubai Alps were significantly lower than that of the Ötztal Alps, but the retrieved LSSARs of the remaining years were higher for the Stubai Alps than for the Ötztal Alps.

The overall derived LSSARs for the glaciers of the Sagarmatha basin in Nepal and of the North Patagonian Icefield in Chile show the smallest variations during the investigated years. The maximum difference of the derived LSSARs for the glaciers of the Sagarmatha basin is 0.15, and for the glaciers of the NPI it is slightly higher with 0.17. In general, the derived LSSARs for the glaciers of the NPI are higher than for the glaciers of the Sagarmatha basin.

In Norway, the derived LSSAR for all glaciers is lower for the glaciers of Svartisen in all investigated years except in 2010. The derived LSSARs show strong variations in the investigated years, with maximum LSSARs for both regions in 1994, when the investigated Landsat scene was acquired at the end of July, and the lowest LSSARs in 1999, when the Landsat scene was acquired in beginning of October.

The derived LSSARs for the Barnes Icecap in the Canadian Arctic show the only continuous decrease of the late summer snow area extent since the mid 1980's to the present. In Figure 5.8 the late summer snow area ratios for all glaciers in the selected regions derived from these scenes are shown.

In the following sub-sections, the temporal variations of the late summer snow areas on the glaciers in the individual regions are investigated in more detail.

5.2.1 Kenai Mountains, Alaska

For the glaciers of the Harding Icefield Landsat images meeting the requirements are available since 1986. The late summer snow / ice area extent shows strong variations from year to year. This is partly caused by the image acquisition date, which was in some years already in high summer (1986, 2000, 2001, 2002, and 2009), as previously mentioned. But also for the years, when satellite images were acquired in late summer (1986, 1999, 2006, and 2007), the differences in the derived LSSARs are partly large. In the year 1999, an exceptional high LSSAR was retrieved compared to the other late summer scenes. For the years 2000, 2001, and 2002, the images were acquired at similar dates. The derived LSSARs are very similar for all three years. Compared to these snow area extents, the snow area derived from the high summer scene of 2009 is significantly lower.

The snow area extents derived for 1986 from both, the high and the late summer image, are significantly smaller than in all other years. The scenes acquired in 2006 and 2007 show a similar extent of the late summer snow area on the Harding Icefield, which is also indicated by the derived LSSARs. Assuming an AAR of 0.68 for the Harding Icefield in equilibrium, as reported by Adalgeirsdóttir et al. (1998), reveal that only the scenes acquired between 2000 and 2002 have snow area extents on the glaciers indicating a mass balance in equilibrium or even slightly positive at the image acquisition date.

Sensor	Path / Row	Image acquisition date	DEM	Applied threshold	Snow covered area [km²]	Glacier area [km²]	LSSAR
L5 TM	069 / 018	09/07/2009	USGS DEM	0.45	1302.8337	2011.77	0.65
L5 TM	069 / 018	06/09/2007	USGS DEM	0.50	917.4951	2011.77	0.46
L5 TM	068 / 018	12/09/2006	USGS DEM	0.49	952.3521	2011.77	0.47
L7 ETM+	069 / 018	30/07/2002	USGS DEM	0.27	1449.8739	2011.77	0.72
L7 ETM+	069 / 018	12/08/2001	USGS DEM	0.48	1482.4863	2011.77	0.74
L7 ETM+	069 / 018	09/08/2000	USGS DEM	0.31	1400.301	2011.77	0.70
L7 ETM+	069 / 018	08/09/1999	USGS DEM	0.50	1122.6519	2011.77	0.56
L5 TM	069 / 018	12/09/1986	USGS DEM	0.52	621.0216	2011.77	0.31
L5 TM	068 / 018	19/07/1986	USGS DEM	0.57	484.1505	2011.77	0.24

Table 5.3: Overview on the multi-annual investigation of the late summer snow areas and the associated late summer snow area ratios of the glaciers on and around the Harding Icefield, Alaska, derived from Landsat imagery and the USGS DEM.

If the glacier areas of the Harding Icefield including the surrounding glaciers reported by Giffen et al. (2007) for the years 1986 (1935.03 km²) and 2000 (1902.79 km²) are used as reference glacier areas for the retrieval of the LSSARs, the retrieved LSSARs for the years 2000 to 2002 indicate slightly positive mass balances. For the reported glacier area of 1986, the LSSARs increase about 0.01 for both, the scene acquired in September, and that acquired in July. Relating the late summer snow areas derived from the Landsat images acquired between 1999 and 2002 to the reported glacier area of 2000 result in increases of the LSSARs of 0.03 in 1999 and 0.04 in the other three years.
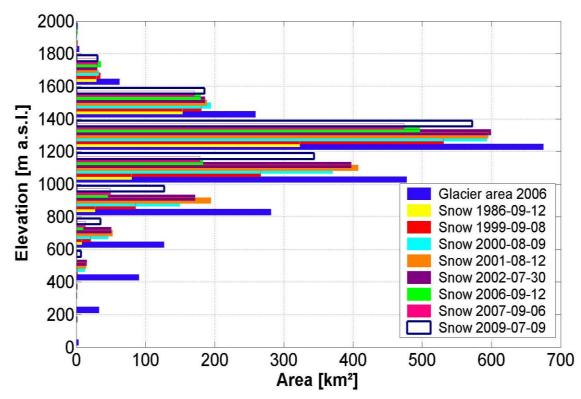
Figure 5.9: Area altitude distribution of the snow covered areas derived from Landsat imagery of several years between 1986 and 2009 and the area altitude distribution of the total glacier areas of the Harding Icefield, Alaska. Elevations are derived from the USGS DEM, and areas are grouped into 200 m elevation intervals.

The largest year to year differences for the snow covered area extents on the glaciers of the Harding Icefield are found for elevations between 600 and 1400 m a.s.l., where also the largest glacier areas are located. Above 1400 m a.s.l., the snow area extents are very similar for most of the years, with the only significantly smaller snow area extent in 1986. The snow area extents for the years 2000, 2001, and 2002 are similar for all elevation intervals. In 2002, the snow area was about 30 km² smaller than in 2001, corresponding to a decrease of the LSSAR of 0.02. This difference is mainly caused by less snow covered areas between 800 and 1200 m a.s.l. in the year 2002. The same can be observed for the years 2000 and 2002. The retrieved snow area is about 50 km² larger in 2002 than in 2000, resulting also in a difference in the LSSAR of 0.02, mainly due to less snow covered area between 800 and 1200 m a.s.l. in the year 2000.

The largest snow area extent derived from a scene acquired in late summer is observed in 1999. In 2006, when the next late summer scene was available, the retrieved snow area extent is about 620 km² smaller than in 1999, with the largest differences between 800 and 1400 m a.s.l.. The difference of the snow area extent in 2006 and 2007 is about 35 km², corresponding to a decrease of the LSSAR of 0.02.

The NCEP / NCAR Reanalysis data between 1981 and 2010 (U.S. Department of Commerce, 2011) are used to investigate the derived snow areas in relation to anomalies

of the air temperature and the surface precipitation rate from the long-term means. Temperature reanalysis data in °C are selected for two ground pressure levels, 1000 mb and 850 mb as proxies for sea level and about 1500 m a.s.l., respectively, in order to investigate the meteorological and seasonal conditions at the low and high elevations of the selected glacier regions in Alaska. The long term mean air temperatures in 1000 mb and 850 mb and the mean surface precipitation rates for the months July to September are illustrated in the graphics of Table 5.4. The shown subset in southern Alaska covers the region between 55°N – 65°N, 140°W – 160°W, with the Kenai Peninsula located approximately in the centre. The investigated glacier regions, the Sargent Icefield, the Harding Icefield and the Grewingk-Yalik Glacier Complex, are located along the east coast of the Kenai Peninsula.
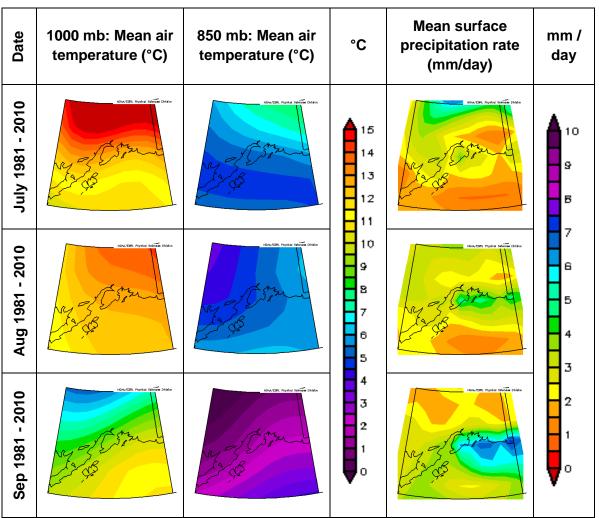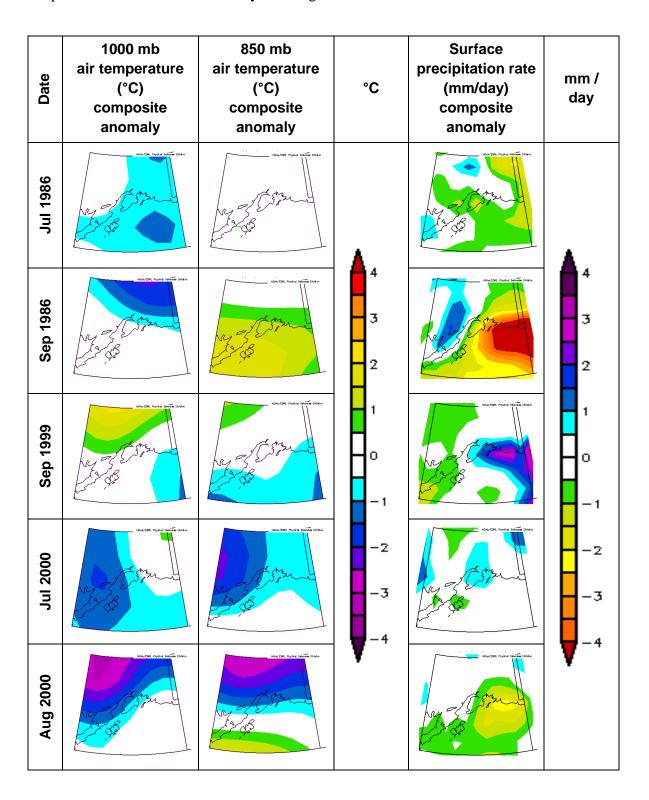
Table 5.4: Long term (1981 – 2010) mean monthly air temperature in °C on the ground pressure levels 1000 mb (left) and 850 mb (middle), approximating the lowest and the highest elevation zone of the glaciers in Alaska, and mean monthly surface precipitation rate in mm/day (right) for July to September from the NCEP / NCAR Reanalysis (U.S. Department of Commerce, 2011).

The long term mean air temperatures in both ground pressure levels on the Kenai Peninsula are positive in all summer months. At the pressure level 1000 mb, the long-term mean air temperature ranges between about 8.5°C in September and about 13°C in July. At 850 mb, the long-term mean air temperature ranges between about 1°C in September and about 5.5°C in July and August.

Date	1000 mb air temperature (°C) composite anomaly	850 mb air temperature (°C) composite anomaly	°C	Surface precipitation rate (mm/day) composite anomaly	mm / day
Jul 1986					
Sep 1986					
Sep 1999					
Jul 2000					
Aug 2000					
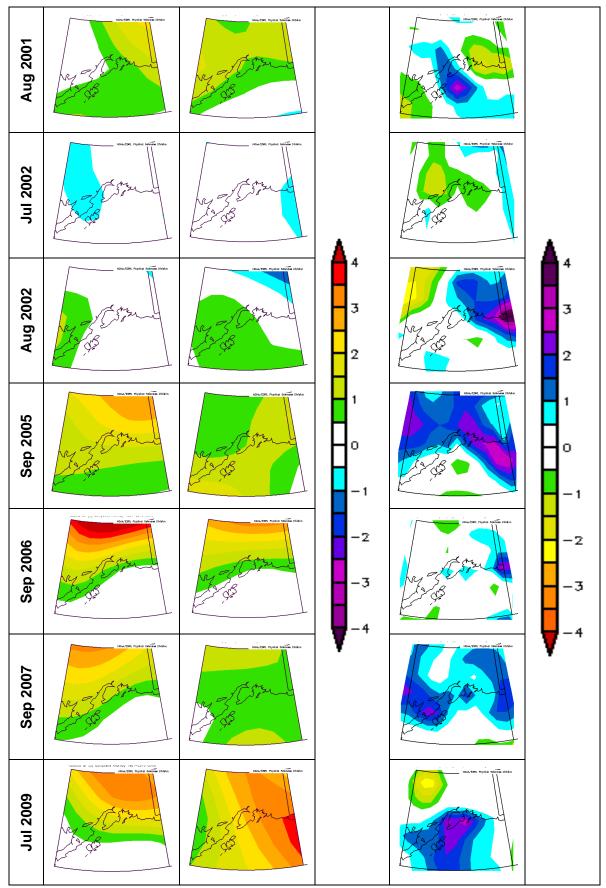
Table 5.5: Air temperature (°C) anomalies on the ground pressure levels 1000 mb and 850 mb, approximating the low and high elevation zones of the glaciers in Alaska, and

surface precipitation rate (mm/day) anomalies for the months when Landsat images were investigated. Graphics from the NCEP / NCAR Reanalysis (U.S. Department of Commerce, 2011).

Precipitation events occurs in all summer month, with the lowest long term mean of the daily precipitation rate on the Kenai Peninsula in July, and the highest in September along the coast of southern Alaska. Monthly anomalies from the mean temperatures at 1000 mb and 850 mb pressure levels, and of the surface precipitation rate for the months when Landsat images were analysed are listed in Table 5.5.

Anomalies in the surface precipitation rate on the Kenai Peninsula occur in most of the months when Landsat images were investigated. The precipitation anomalies in July 1985, August 2002 and September 2006 on investigated regions on the Kenai Peninsula are within ±0.5 mm/day. Negative surface precipitation rate anomalies were observed in July and September 1986 and in August 2000, while the anomalies in the other investigated months were positive. The most negative anomaly in the surface precipitation rate was found in September 1986, the most positive in July 2009. In this month also the highest positive temperature anomalies were found on the Kenai Peninsula at the two ground pressure levels 1000 mb and 850 mb. The most negative temperature anomalies were found in July 2000 at 1000 mb and in August 2000 at 850 mb.

Considering that the scene in 2002 was acquired in high summer, the ablation area extent at the end of summer might have been significantly larger. The difference in the snow covered areas in 1986 and 2007 can be explained by the larger positive temperature anomaly at 1000 mb in 2007, although the temperature anomaly at 850 mb was more positive in 1986. The long-term mean air temperature at this elevation zone is between 1.5°C and 2°C, and the effect of a positive temperature anomaly between 1°C and 1.5°C might be large. Although the temperature anomalies in July 2009 are positive at both ground pressure levels, the snow areas extents are relatively large in all elevation intervals. This can be mainly be explained by the early image acquisition date in this year.

On the glaciers of the Sargent Icefield, the temporal distribution of the late summer snow areas, summarized in Table 5.6, is in some years significantly different to that of the Harding Icefield.

The temperature anomalies of the NCEP / NCAR Reanalysis (U.S. Department of Commerce, 2011) are also reflected by the snow area extents on the glaciers of and around the Sargent Icefield. The lowest snow area extent was derived for September 2005, which shows positive deviations of the air temperatures between 1°C and 2°C at the two ground pressure levels from the long-term mean. In 2002, when the image acquisition date is only two weeks earlier, the derived snow area extent is about twice the derived late summer snow area of 2005. The temperatures in July 2002 are within ±0.5°C at the two ground pressure levels, and at 1000 mb also in August 2002. At 850 mb the air

temperature in August 2002 deviates between about 0.5°C to 1°C from the long-term mean. Also the anomalies of the surface precipitation rates in these two months are within ±0.5 mm/day over large areas on the Kenai Peninsula. The year 2002 is also the year with the highest derived LSSAR, and correspondingly the largest snow area extent, but with only minor difference to the snow area extent in 2001, when the image was acquired about two weeks earlier. In August 2001, a positive temperature anomaly of 1°C at 1000 mb and 850 mb can be observed over large areas of the Kenai Peninsula. Positive anomalies of the surface precipitation rate between 0.5 mm/day and 2 mm/day occur rather in the southern part of the peninsula, and are thus not relevant for the Sargent Icefield, which is located in the northern part of the Kenai Peninsula. The end of summer snow area extents in 2001 and also in 2009, when the investigated Landsat image was acquired in the beginning of August, might have been significantly smaller than measured at the image acquisition dates. Monthly temperature and precipitation anomalies are also reflected by the LSSARs in the other investigated years.

Sensor	Path / Row	Image acquisition date	DEM	Applied threshold	Snow covered area [km²]	Glacier area [km²]	LSSAR
L5 TM	068 / 018	03/08/2009	USGS DEM	0.50	1141.69	2204.51	0.52
L5 TM	068 / 018	12/09/2006	USGS DEM	0.49	884.04	2204.51	0.40
L5 TM	067 / 018	18/09/2005	USGS DEM	0.50	574.14	2204.51	0.26
L7 ETM+	067 / 018	02/09/2002	USGS DEM	0.26	1200.97	2204.51	0.55
L7 ETM+	068 / 018	21/08/2001	USGS DEM	0.35	1178.16	2204.51	0.54
L7 ETM+	067 / 018	26/09/1999	USGS DEM	0.52	973.56	2204.51	0.44
L5 TM	067 / 018	14/09/1986	USGS DEM	0.46	1055.25	2204.51	0.48
L5 TM	068 / 018	19/07/1986	USGS DEM	0.57	1100.91	2204.51	0.50

Table 5.6: Overview on the multi-annual investigation of the late summer snow areas and the associated late summer snow area ratios of the glaciers on and around the Sargent Icefield, Alaska, derived from Landsat imagery and the USGS DEM.

Major differences in the derived LSSARs of glaciers on and around the Sargent Icefield are reflected at elevations below 1400 m a.s.l. (Figure 5.10). In the uppermost 400 m, the differences in the derived snow area extents are negligible in all years. For the years

1986, 1999, and 2001 the snow area extents between 1200 m a.s.l. and 1400 m a.s.l. were about equal. For the years 1986 and 1999 about equal snow areas are derived for the elevation interval 1000 m a.s.l. to 1200 m a.s.l.. Below 1000 m a.s.l., the snow area extent per elevation interval for these years is largest in the year 2001 and lowest for the year 1999. An interesting observation can be made for the area altitude distribution of the snow area derived in 2005. In this late summer with low LSSAR, the maximum snow area was located between 1200 m a.s.l. and 1400 m a.s.l., while in the other years, the maximum snow area extent was found between 800 m a.s.l. and 1000 m a.s.l..
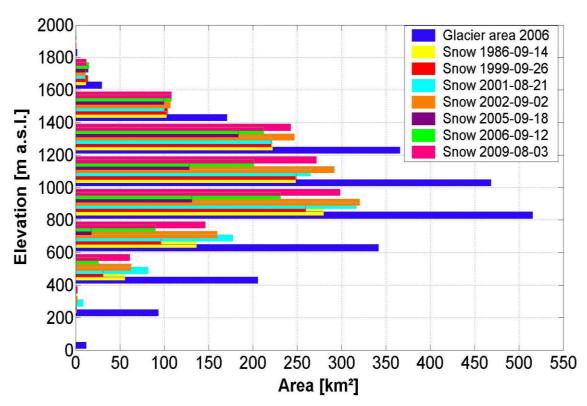
*Figure 5.10: Area altitude distribution of the snow covered areas derived from Landsat imagery of several years, and the area altitude distribution of the total glacier areas of the Sargent Icefield, Alaska. Elevations are derived from the USGS DEM, and areas are grouped into 200 m elevation intervals.*

Also on the glaciers of the Grewingk-Yalik Glacier Complex, the LSSAR derived for the year 2002 is the highest of the investigated dates. This scene was acquired end of July which showed temperature and precipitation anomalies of only ±0.5 from the long-term means. The late summer snow area ratio at the date with the maximum extent of the ablation area was probably significantly lower. A similar pattern can be observed for the year 2000, when the image acquisition date was about 10 days later than in 2002, resulting also in a high LSSAR. Additionally, negative temperature anomalies between 0.5°C and 1°C can be observed at the two ground pressure levels 1000 mb and 850 mb in August 2000. The scenes acquired in late summer, in the years 1986, 1999, and 2007,

show indeed significantly lower LSSARs. The temperature anomalies were significantly positive at the ground pressure level 850 mb in September 1986 and at 1000 mb and 850 mb in September 2007. But the anomalies of the surface precipitation rate were different for these two years. In September 1986 a negative anomaly between about 1 mm/day to 2 mm/day can be observed, while the anomaly in the same precipitation rate range was positive in September 2007. The investigated scene of 2009 was already acquired in the mid of July, but already at this time the snow covered area extent was strikingly small compared to the LSSARs of the previous 10 years, which is in line with the observed positive temperature anomalies in this month, although also the surface precipitation rate shows a significantly positive anomaly between 2 mm/day to 3 mm/day on the southern part of the Kenai Peninsula.

Relating the derived snow covered areas to glacier areas of the Grewingk-Yalik Glacier Complex and surrounding glaciers reported by Giffen et al. (2007) for the years 1986 (444.81 km²) and 2000 (424.32 km²) results in no changes of the LSSARs retrieved from both scenes of 1986. But all LSSARs derived for the years 1999 to 2002 increase, in 1999 by about 0.03, by about 0.05 in 2000 and by about 0.06 in 2002.

Sensor	Path / Row	Image acquisition date	DEM	Applied threshold	Snow covered area [km²]	Glacier area [km²]	LSSAR
L5 TM	069 / 018	09/07/2009	USGS DEM	0.45	131.22	458.52	0.29
L5 TM	069 / 018	06/09/2007	USGS DEM	0.50	179.91	458.52	0.39
L5 TM	068 / 018	12/09/2006	USGS DEM	0.49	136.03	458.52	0.30
L7 ETM+	069 / 018	30/07/2002	USGS DEM	0.27	337.85	458.52	0.74
L7 ETM+	069 / 018	09/08/2000	USGS DEM	0.31	314.54	458.52	0.69
L7 ETM+	069 / 018	08/09/1999	USGS DEM	0.50	209.10	458.52	0.46
L5 TM	069 / 018	12/09/1986	USGS DEM	0.52	49.60	458.52	0.11
L5 TM	068 / 018	19/07/1986	USGS DEM	0.57	81.13	458.52	0.18

Table 5.7: Overview on the multi-annual investigation of the late summer snow areas and the associated late summer snow area ratios of the glacier on and around the Grewingk-Yalik Glacier Complex, Alaska, derived from Landsat imagery and the USGS DEM.

A clear indicator that a scene was acquired still in the midsummer is some remnant snow between 400 m a.s.l. and 600 m a.s.l., while the snow area in this elevation range derived from late summer scenes is either small or does not exist (Figure 5.11).

The LSSAR derived from Landsat scenes actually acquired in the late summer is largest in September 1999. Over the southern part of the Kenai Peninsula, this month shows temperature anomalies from the long-term mean of about ±0.5°C at 1000 mb and 850 mb and precipitation anomalies of about ±0.5 mm/day. The snow area extents in the years 1986 and 2007 show significant differences, especially at altitudes between 600 m a.s.l. and 1400 m a.s.l., although the images were acquired around the same date. The previously described temperature anomalies at the two ground pressure levels and the different anomalies in the surface precipitation rate for these two years might explain the differences in the snow area extents.
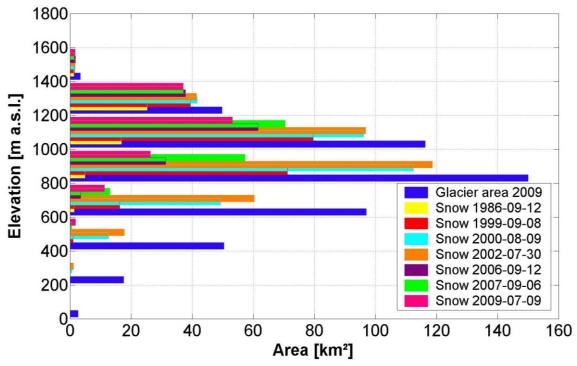
Figure 5.11: Area altitude distribution of the snow covered areas derived from Landsat imagery of several years, and the area altitude distribution of the total glacier areas of the Grewingk-Yalik Glacier Complex, Alaska. Elevations are derived from the USGS DEM, and areas are grouped into 200 m elevation intervals.

Considering also the other investigated years, major differences in the snow area extents can be observed in elevations between 400 m a.s.l. and 1200 m a.s.l., while the differences in the snow area extents above 1200 m a.s.l. are rather small.

In Figure 5.12 the overall LSSARs derived for glaciers of the three selected regions in Alaska since 1986 are summarized, reflecting the previously presented results.
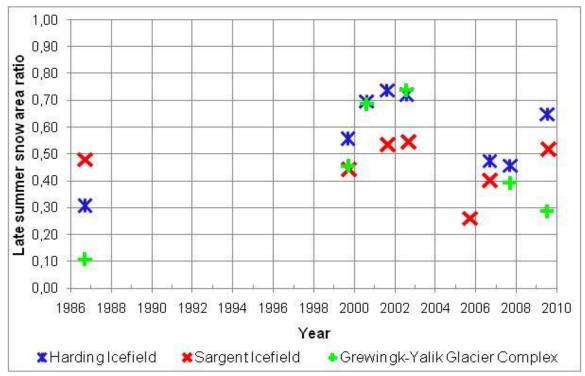
Figure 5.12: Temporal variation of the late summer snow area ratios on the Harding and the Sargent Icefield, and the Grewingk-Yalik Glacier Complex, derived from Landsat imagery between 1986 and 2009. Only the blue marked dates of Table 5.3, Table 5.6, and Table 5.7 are used in this graphic.

In Alaska, only the glaciers of the Harding Icefield and of the Grewingk-Yalik Glacier Complex are investigated considering the glacier exposition.
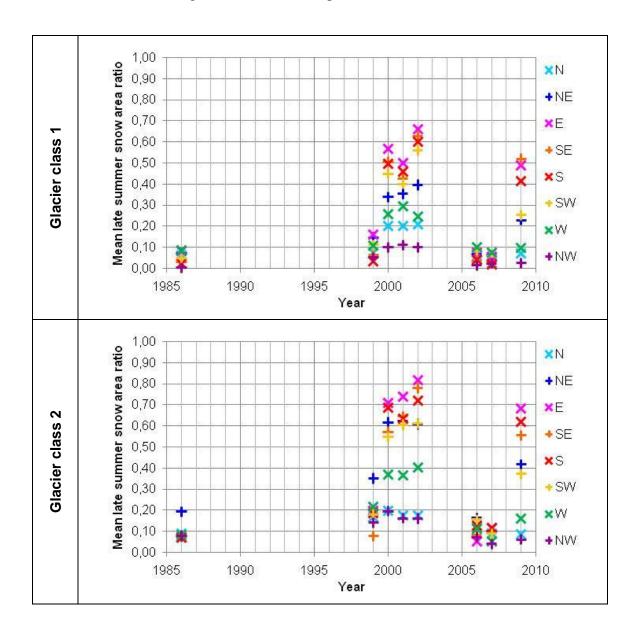
On the Harding Icefield, all aspects are present by glaciers smaller than 10 km², belonging to the glacier classes 1 to 3. South orientated glaciers larger than 10 km² do not occur on the Harding Icefield. Glaciers larger than 100 km² have additionally no representative with a northeast orientation. Six glaciers on the Harding Icefield with different expositions have a total area larger than 100 km², represented by the glacier class 5.

The graphics in Figure 5.13 illustrate the temporal variations of the mean LSSARs, considering the total area and the dominant aspect of the individual glaciers on and around the Harding Icefield. In order to be consistent with the labelling of the graphics, the derived LSSARs for glaciers of class 5 are illustrated as mean LSSARs, although each aspect is only represented by one glacier in this class.

For the investigated time series, the highest mean LSSARs for glaciers of the Harding Icefield are found for the southeast orientated Northwestern Glacier, belonging to the glacier class 5 with a total area of 161 km². The northwest orientated glacier Harding Icefield, belonging to the same glacier class with a total area of 206 km² has in most of the years already significantly lower LSSARs, except in 2001, when the derived LSSARs

for both glaciers are about equal. The lowest LSSARs in this glacier class are derived for the north orientated Skilak Glacier (125.5 km²) and the east orientated Bear Glacier (149 km²), while the LSSARs of the west orientated Tustumena Glacier (336.5 km²) and the southwest orientated McCarty Glacier (119 km²) are among them.

Southeast orientated glaciers smaller than 100 km² have only low to medium LSSAR values in the investigated years, but the highest mean ratios in the classes 1 to 4 are found for east orientated glaciers in most of the years. Northwest orientated glaciers smaller than 100 km² have often the lowest LSSARs. In some years indeed, the lowest mean LSSARs are derived for glaciers with other expositions.
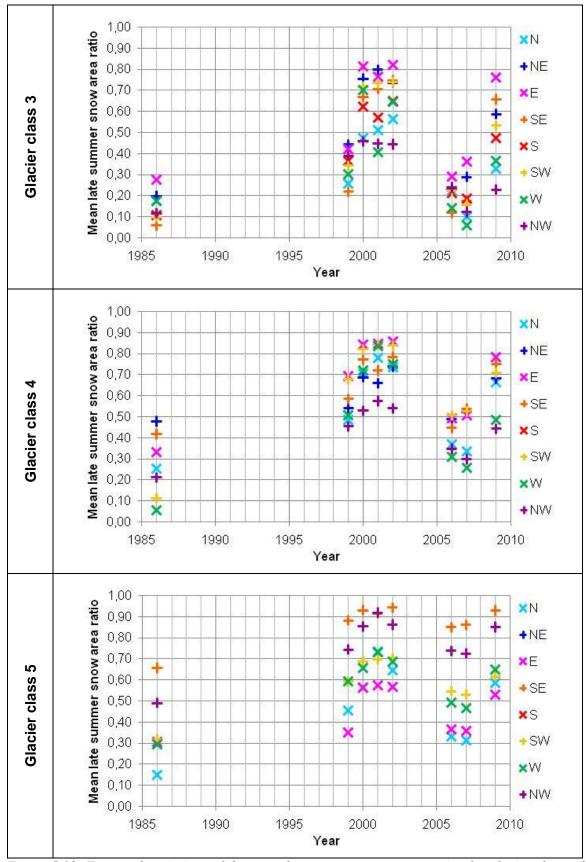
Figure 5.13: Temporal variations of the mean late summer snow area ratios for glaciers located at the Harding Icefield, Alaska, considering the glacier areas and the main glacier aspects.

For glaciers smaller than 100 km² the general variations of the mean LSSARs in the investigated years are similar, with low mean LSSARs for glaciers of all aspects in 1986, 1999, 2006, and 2007, and higher mean LSSARs in the other years. For the years with low mean LSSARs, the differences of the mean LSSARs with the glacier exposition for glaciers smaller than 1 km² range between 0.06 for glaciers of class 1 in 2007 and 0.21 for glaciers of class 2 in 1999. In the other years, the ranges of the LSSARs for glaciers with different orientations are larger, between 0.39 for glaciers of class 1 in 2001, and 0.66 for glaciers of class 2 in 2002. The latter is also the maximum difference of the derived mean LSSARs during the investigated time series, and occurs between east and northwest orientated glaciers. For glaciers of class 3 and 4 with different aspects the ranges of the derived LSSARs are between 0.17 in 2006 and 0.53 in 2009, both extremes found for glaciers of class 3.

The smallest variations in the investigated years are found for north and northwest orientated glaciers of the classes 1 and 2, the largest are found for east orientated glaciers smaller than 100 km². Southwest and northeast orientated glaciers of all classes have often similar mean LSSARs, but show partly also significant differences, for example in 1986 for glaciers of class 4. West orientated glaciers of the classes 1, 2 and 5 have mean LSSARs in the mid of the derived LSSAR ranges in the investigated years, but show large variations for glaciers of the classes 3 and 4. South orientated glaciers of class 1 and 2 have in most of the years relatively high mean LSSARs, while the values for the glaciers of class 3 are ranging in the central part of the derived LSSAR range.

With increasing glacier size, also the derived mean LSSARs are higher in the investigated years. A general temporal trend for glaciers with a specific aspect cannot be observed for the glaciers on and around the Harding Icefield in the investigated years.
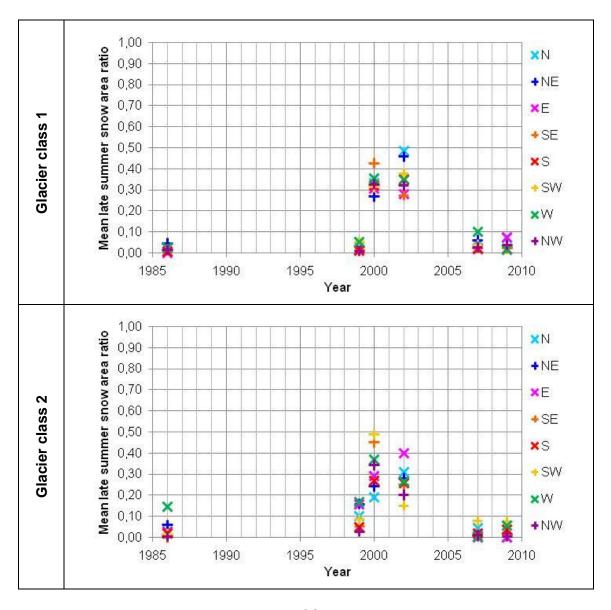
On the Grewingk-Yalik Glacier Complex only glaciers smaller than 1 km² are represented by each aspect. In glacier class 3, no north and northeast orientated glaciers occur, and in glacier class 4, the southwest orientation is not represented. Glaciers larger than 100 km² do not occur in this region.

The largest glaciers of the GYGC have not only the largest mean LSSARs for some aspects, but show also the largest variations for north and southeast orientated glaciers in the investigated time series. Northeast orientated glaciers of class 4 show an increase of the derived mean LSSARs since 2000, while the mean LSSARs on glaciers with other aspects have no obvious trends. In the years 2002, 2007 and 2009, north, northwest, and south orientated glaciers of glacier class 4 have mean LSSARs close to or equal zero. In 2007, also all others except the northeast orientated glaciers of this class have mean LSSARs close to or equal zero. Considering all investigated years, the variations are large for glaciers of all aspects in this class.

Also the glaciers smaller than 10 km² show low mean LSSARs in the years 1986, 2007 and 2009 for glaciers of all occurring aspects. The highest mean LSSARs are found in 2000 and 2002 for glaciers of all classes, but for different aspects per class and year. This

is the same pattern as observed for the glaciers of the Harding Icefield, except for 2009, when the derived mean LSSARs of all aspects are significantly lower for the glaciers of the GYGC compared to these of the Harding Icefield.

The ranges of the derived mean LSSARs for the individual aspects are smaller than these derived for the glaciers of the Harding Icefield. The minimum range of the mean LSSAR is 0.02 occurring for glaciers of class 3 in 2009. The maximum derived range of the mean LSSAR is 0.76 for glaciers of class 4 in 2002, and decrease with decreasing glacier areas to 0.21 for glaciers of class 1 in 2002. The derived mean LSSARs show significant variations per glacier area and aspect in the investigated years. A decrease of the mean LSSARs can be observed for glaciers of class 3 since 1999 for south orientated glaciers, since 2000 for northwest orientated glaciers, and since 2002 for glaciers of all orientations. The distributions of the mean LSSARs derived for glaciers smaller than 1 km² have no clear trend for any aspect. But the derived mean LSSARs for these classes are in general low except in 2000 and 2002.
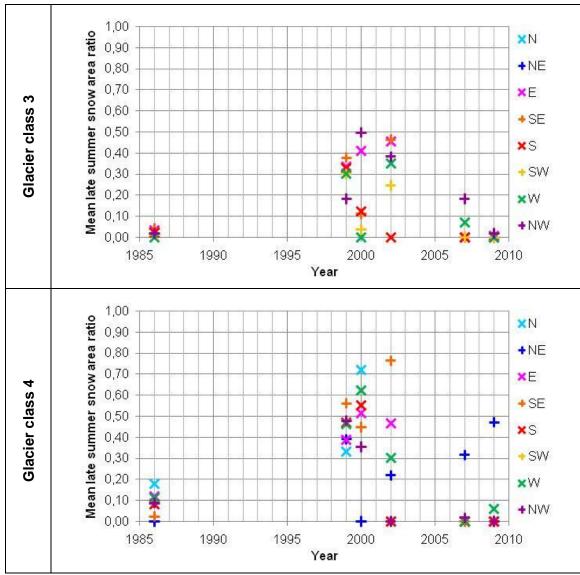
Figure 5.14: Temporal variations of the mean late summer snow area ratios for glaciers located at the Grewingk-Yalik Glacier Complex, Alaska, considering the glacier areas and the main glacier aspects.

5.2.2 Stubai and Ötztal Alps, Austria

For the Stubai and the Ötztal Alps in Austria, Landsat imagery since 1985 was investigated to retrieve time series of the late summer snow areas on the glaciers. For the Stubai Alps, glacier outlines are available mapped in Landsat data of 1985, used as reference for the snow areas derived from the Landsat scenes of the 1980's, and outlines mapped in ASTER imagery of 2003, used as reference for the snow areas derived from Landsat imagery since 1999. Both outline sets of the Stubai Alps were mapped by Schicker (2006), and are made available via the GLIMS data base. For the Ötztal Alps, glacier outlines based on orthophotos acquired between 1996 and 1999 (Lambrecht and Kuhn, 2007) are used as reference.

Both regions are covered by one Landsat scene, and the late summer snow areas on the glaciers in both regions were derived by the main processing line using only one threshold for each scene.

Image acquisition date	DEM	Applied threshold	Ötztal		Stubai	
			Late summer snow area [km²]	LSSAR	Late summer snow area [km²]	LSSAR
31/08/2009	National	0.43	25.0578	0.16	5.3262	0.15
26/10/2006	National	0.67	29.8989	0.19	5.2578	0.15
24/09/2006	National	0.46	32.6727	0.21	7.7274	0.21
23/08/2006	National	0.43	89.7282	0.57	24.273	0.67
12/08/2005	National	0.37	55.1313	0.35	15.2424	0.42
10/09/2004	National	0.48	26.964	0.17	6.0606	0.17
30/07/2003	National	0.45	35.7246	0.23	8.01	0.22
15/09/2000	National	0.47	61.0677	0.39	17.7147	0.49
13/09/1999	National	0.38	57.8943	0.37	18.2556	0.50
03/10/1986	National	0.53	33.3675	0.21	3.8322	0.06
03/10/1986	National	0.53			3.8322	0.11[*]
13/08/1985	National	0.49	116.4528	0.74	31.0851	0.50
13/08/1985	National	0.49			31.0851	0.86[*]

*Table 5.8: Overview on the investigation of the late summer snow in several years on the glaciers in the Ötztal and Stubai Alps, derived from Landsat imagery (Path 193 / Row 027) and the National DEM by the standard processing line. The used total glacier area of the Ötztal Alps is 157.40km². *) For the glaciers in the Stubai Alps the LSSARs since 1999 are referenced to the glacier area of 2003 (36.35 km²). For the former years, the LSSARs are derived using the glacier area extent of 1985 (62.28 km²) (Schicker, 2006), but the LSSARs using the glacier area extent of 2003 are also presented in this table, marked by a different colour, and in Figure 5.16. Former information regarding the glacier areas of the Stubai Alps in 1985 and 2003 are given in the text and in Section 4.2.2.*

For three glaciers of the Ötztal Alps, Hintereisferner (HEF), Kesselwandferner (KWF) and Vernagtferner (VF), where long-term mass balance measurements are available,

Zemp et al. (2009) reported equilibrium AARs between 0.66 and 0.70. This is close to the steady state AAR of 0.67 proposed by Gross et al. (1977) for alpine glaciers. Relating the derived overall LSSARs in all years to these values indicate strong negative mass balances since the mid 1980's, except in 1985, when the retrieved LSSAR related to the glacier areas of 1998 is slightly higher. The general decreasing mass balance trend since 1985 reported by Abermann et al. (2009) for the glaciers HEF, KWF and VF is also reflected by the LSSARs derived from the investigated Landsat images.

In both regions, the derived LSSARs for the years 1999 and 2000 are similar, with general higher values in the Stubai Alps. Both scenes were acquired at about the same date, in mid of September. In 2003, an exceptionally warm summer occurred in the Austrian Alps with positive temperature anomalies between 3.5°C and 4.5°C (cf. Table 5.10). This is already reflected in the reduced snow area extents on the glaciers of both regions in the end of July. At the Hintereisferner in the Ötztal Alps, where annual mass balances are measured since the beginning of the 1950's, no accumulation area remained at the end of the hydrological year (Fischer, 2010).

For the years 2004 and 2005, only Landsat 7 ETM+ SLC OFF scenes are available. The Ötztal Alps are not affected by data gaps, as these glaciers are fully located in the centre of the scenes. But glaciers of the Stubai Alps are partly affected by the data gaps due to the mission scan line corrector. Thus, the derived LSSARs of the glaciers of the Stubai Alps in these both years might be slightly underestimated. Although the derived LSSAR in both regions indicate strong negative glacier mass balances, the overall situation in both years is not as drastic as in the year 2003.

In 2006, three Landsat scenes meeting the requirements are available. All scenes were investigated, and the overall results for these dates, and also for all other investigated scenes, are presented in Table 5.8 for the Ötztal and Stubai Alps. The strong decrease of the LSSAR between end of August and end of September in both regions indicates the fast response of the snow covered areas on glaciers to meteorological conditions. Assuming the LSSAR as proxy for the AAR, the LSSAR derived for end of August 2006 in the Stubai Alps would indicate an overall balanced state of the glaciers at this date.

The graphics in Table 5.9 show the long term mean of the air temperatures at 850 mb and 700 mb ground pressure levels approximating the low and high elevations of the study regions in Austria, as well as the mean surface precipitation rate in mm/day for the months July to October 1981 to 2010. The shown subset covers the area between 46°N – 48.5°N, 9.3°E – 13°E, with the investigated regions Ötztal and Stubai Alps located approximately in the centre of this subset.

The long-term mean monthly temperatures at 850 mb, approximating about 1500 m a.s.l., are positive between July and October. At the ground pressure level 700 mb approximating an altitude of about 3000 m a.s.l. the long-term mean monthly temperatures are positive from July to September, but slightly negative in October. Similar spatial temperature distributions can be observed in July and August. Long-term

monthly surface precipitation rates range between 3 mm/day to 4 mm/day in July and August, and between 1 mm/day and 2 mm/day in September and October.
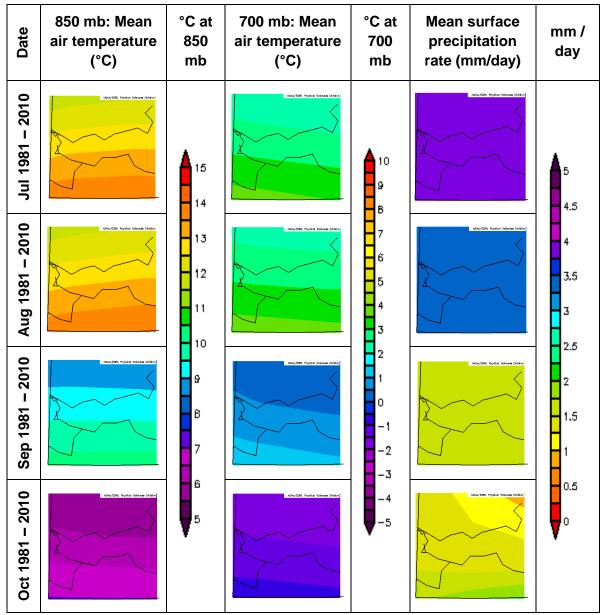
Table 5.9: Long term (1981 – 2010) mean monthly air temperature in °C on the ground pressure levels 850 mb and 700 mb, approximating the lowest and the highest elevation zone of the investigated glaciers in Austria, and mean surface precipitation rates in mm/day for July to October from the NCEP / NCAR Reanalysis (U.S. Department of Commerce, 2011).

Anomalies of the monthly mean temperatures and surface precipitation rates for the month when Landsat images were investigated are listed in Table 5.10.
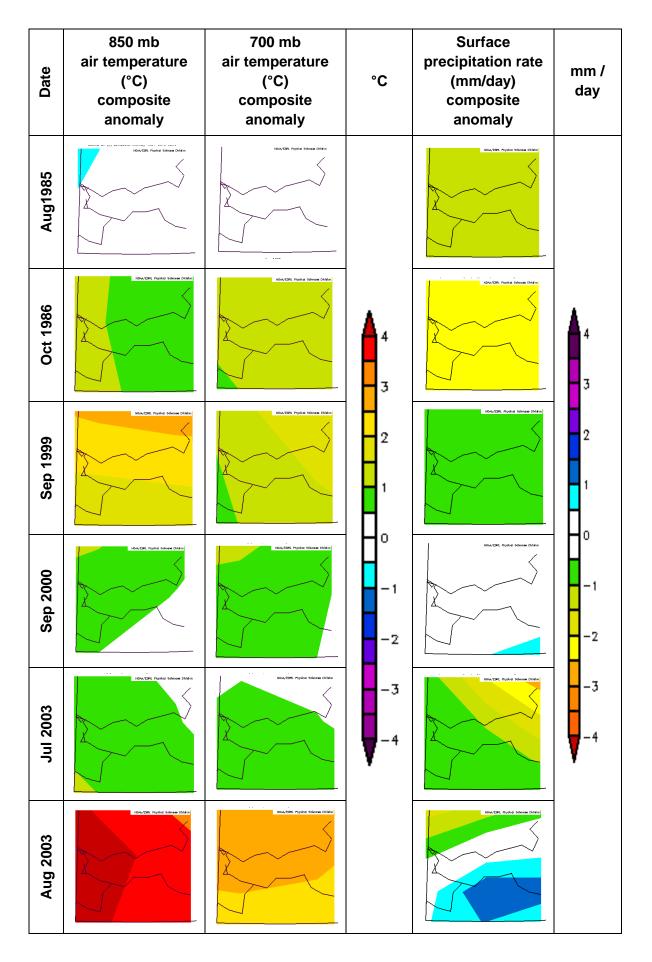
Temperature anomalies occurred in most of the investigated months at the two ground pressure levels, with minor anomalies in August 1985 in both elevation zones, and in September 2004 at 850 mb. Surface precipitation rate anomalies are in most of the investigated months larger than 0.5 mm/day except in September 2000, August 2005, and August and October 2006.

The most negative anomaly from the long-term mean air temperature occurred in August 2006 in the Stubai and Ötztal Alps. This month was at the two ground pressure levels 850 mb and 700 mb about 2.5°C to 3.5°C colder than the long-term average temperature. But in September and October 2006, a strong positive departure of the mean temperature of about 2.5°C to 3.5°C compared to the long-term average was measured. The decreases of the LSSARs in both regions from August 2006 to September 2006 clearly reflect this positive temperature anomaly and the negative surface precipitation rate in September 2006. In the beginning of October 2006, a cold front resulted in a significant temperature decrease and strong precipitation events in form of snow down to 1800 m a.s.l. (http://zamg.ac.at/klima/klima_monat/wetterlagen/). This means also full snow coverage on the glaciers in both regions in Austria. The second half of this month was indeed continuously warmer than the long-term average temperature, resulting in significantly positive anomalies of the air temperatures at 850 mb and 700 mb. This explains the reduced LSSARs in both regions at the end of October 2006 compared to the end of September scene of this year.

The negative temperature anomaly in August 2005 is also clearly reflected by the derived LSSARs in the Stubai and Ötztal Alps. In all other investigated months the temperature anomalies were positive, while the surface precipitation rate anomalies were in most cases negative.

In 2009, the August was by far the warmest month of the year, but the surface precipitation rate was slightly negative compared to the long-term mean. Especially in the second half of the month on most of the days the mean daily temperature was about 4°C to 5°C warmer than the long-term average temperature, attended by partly strong thunderstorms. This phase was only interrupted by a fast cold front (http://zamg.ac.at/klima/klima_monat/wetterlagen/).

A warm September 2009 indicates that the maximum extent of the ablation area was reached later than on the image acquisition date. Based on the already low LSSARs at the end of August in both regions in Austria, it can be assumed that the AAR at the date with the maximum extent of the ablation area might have been in the range of the values at the end of the hydrological year in 2003.

Date	850 mb air temperature (°C) composite anomaly	700 mb air temperature (°C) composite anomaly	°C	Surface precipitation rate (mm/day) composite anomaly	mm / day
Aug1985					
Oct 1986					
Sep 1999					
Sep 2000					
Jul 2003					
Aug 2003					
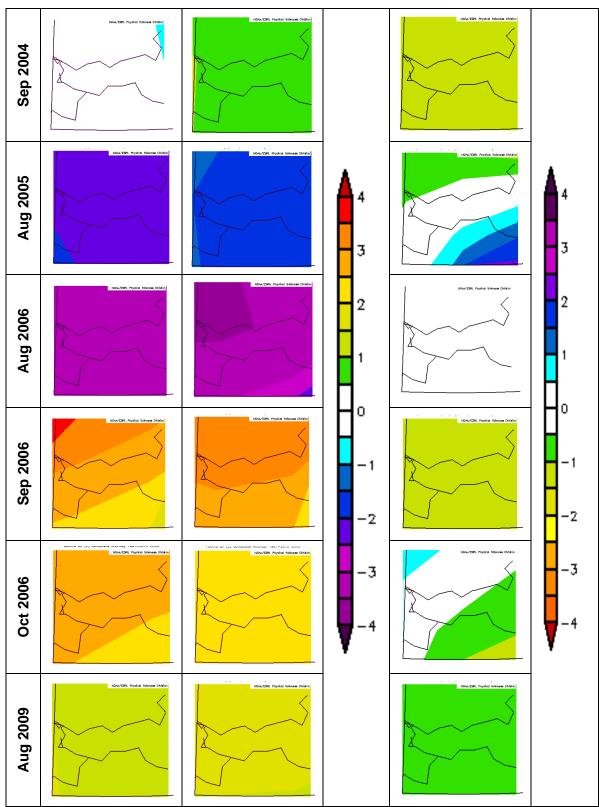
Table 5.10: Air temperature (°C) anomalies on the ground pressure levels 850 mb and 700 mb, approximating the lowest and the highest elevation zone of the glaciers in Austria, and surface precipitation rate (mm/day) anomalies for the months when Landsat images were investigated. Graphics are from the NCEP / NCAR Reanalysis (U.S. Department of Commerce, 2011).

Comparing the derived LSSARs of Vernagtferner with accumulation area ratios derived from field measurements done by members of the Kommission für Glaziologie of the Bayerischen Akademie der Wissenschaft (BAdW) shows in most of the investigated years good agreements (cf. Figure 5.15). The comparatively high LSSARs in 1985, 2003 and 2005 are due to the early Landsat image acquisition date, while the mass balance measurements were done at the end of the mass balance years. An ASTER scene of 23 August 2003 was used to map the snow area on the Vernagtferner at a later date in this exceptionally warm summer. Due to extensive cloud coverage on several glaciers not the full ASTER scene was analysed. The derived snow area ratio for the Vernagtferner from this scene is already significantly lower compared to the LSSAR of end of July, but the maximum extent of the ablation area was still not reached. At the end of the mass balance year no snow remained at the Vernagtferner.
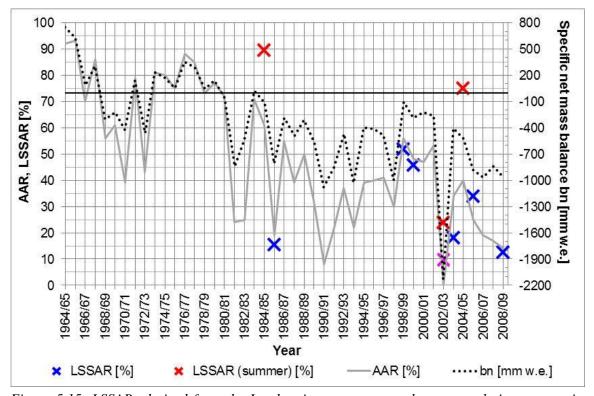
Figure 5.15: LSSARs derived from the Landsat imagery compared to accumulation area ratios and specific net balance bn in mm w.e. derived from field measurements on the Vernagtferner in the Ötztal Alps, Austria. Red crosses indicate the Landsat image acquisition date was in end of July (2003) or mid of August (1985 and 2005). The pink cross in 2003 shows the LSSAR derived from mapping snow areas from an ASTER scene of 23 August 2003. Annual values of the AAR and the specific net mass balance are from mass balance measurements done by members of the Kommission für Glaziologie of the Bayerische Akademie der Wissenschaft (BAdW), München (Kommission für Glaziologie der BAdW, 2010). The black line indicates the mass balance of the Vernagtferner in equilibrium.

In Figure 5.16 the temporal variations of the derived LSSARs are summarized for both regions in Austria. For the Stubai Alps, the snow areas derived from the Landsat images of the mid 1980's are additionally related to the glacier areas of 1980's, as previously mentioned. This results in significantly lower LSSARs for this reference glacier area, as illustrated in the graphic. For the Stubai Alps, an almost continuously decrease of the derived late summer snow area can be observed since the mid 1980's, with exceptions in 1986 and in 2005. The snow area ratios in 2003 at the end of the mass balance year were in both regions close to zero, as also illustrated on the example of the Vernagtferner in Figure 5.15, but the investigated Landsat scene used for the retrieval of the LSSARs was already acquired in end of July. For the Ötztal Alps, the derived LSSARs show more fluctuations in both directions.
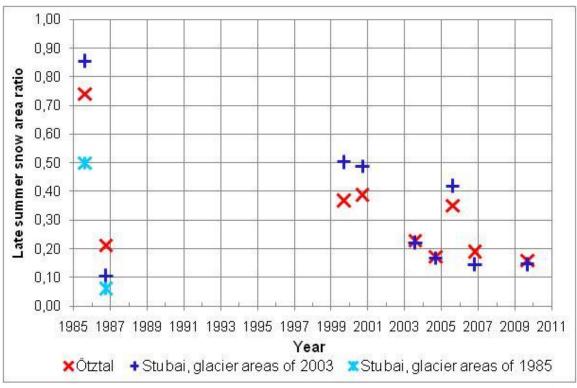
Figure 5.16: Temporal variation of late summer snow area ratios of glaciers in Stubai and Ötztal Alps, derived from Landsat imagery between 1985 and 2009. Only the blue and cyan marked data of Table 5.8 are used for this graphic.

Relating the retrieved late summer snow areas in the Stubai Alps to discrete elevation intervals show the largest differences between 2900 m a.s.l. and 3300 m a.s.l., where also the largest glacier areas are found. Above 3300 m a.s.l., the derived snow areas are similar for the years 1985, 1999, 2000, 2003, and 2005, while the snow covered areas in the other years are generally smaller, but also with similar extent at this elevation zone. The high LSSAR derived for 1985 is mainly reflected in additional snow areas between 2700 m a.s.l. and 3100 m a.s.l. compared to the snow coverage of the other years. The

minor snow covered area in 1986 builds a strong contrast in all elevation intervals. The distribution of the snow area in 1999 and 2000 related to the altitude intervals is different, although the derived LSSAR for both years is almost equal. In 1999, the main snow area was located between 3100 m a.s.l. and 3300 m a.s.l., while in 2000, the main snow area was found 200 m lower, between 2900 m a.s.l. and 3100 m a.s.l.. In the year 2000 also at lower elevations down to 2700 m a.s.l. more snow remained compared to 1999. In 2003, the derived snow area extents in the discrete elevation intervals are relatively large compared to the snow area extents of 2009. But as previously mentioned, the snow areas in 2003 were derived from an end of July scene, in the middle of the strong melting period, while the image of 2009 was acquired one month later. In 2004 and 2005, the derived snow areas are partly underestimated due to data gaps in the basic Landsat scene. The real snow area extent in 2004 might thus have been slightly larger. The scene in 2005 was already acquired in mid of August, when the melting period was still on-going, although the mean daily temperatures strongly varied in this month and were often far below the long-term average temperature. Though the derived snow area at this date is underestimated due to gaps in the Landsat scene, the final snow area extent at the end of the summer might have been smaller.
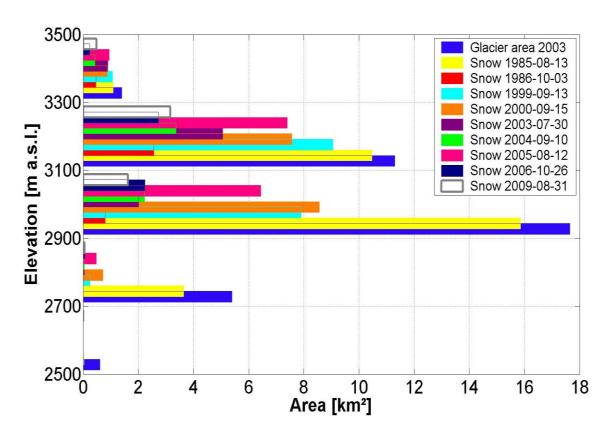
Figure 5.17: Area altitude distribution of snow areas in several years between 1985 and 2009 and the total glacier area of 2003 of the Stubai Alps, Austria. Elevations are derived from the national DEM, and areas are grouped into 200 m elevation intervals.

As previously already described in detail, the late summer snow area extent in 2006 was very small due to several weeks with high temperatures. The largest snow areas for this year are found between 3100 m a.s.l. and 3300 m a.s.l., which are in the range of the snow extent in 1986 in this elevation interval. The larger overall LSSAR derived in 2006 compared to 1986 is due to larger snow covered area between 2900 m a.s.l. and 3100 m a.s.l.. The largest late summer snow areas on the glaciers of the Ötztal Alps are found in all years between 3100 and 3300 m a.s.l., where the largest glacier areas are located, as also reported by Abermann et al. (2009).

In 1985, the largest snow covered areas are located between 2900 m a.s.l. and 3300 m a.s.l., which is in the same elevation range as in the Stubai Alps. The general pattern of the snow distribution in the individual years is similar to that of the Stubai Alps, but the glaciers cover a broader elevation range, and thus, also the snow areas are partly found at other elevations as in the Stubai Alps. The main changes in the year to year distribution of the snow covered area are between 2900 m a.s.l. and 3500 m a.s.l.. Above 3500 m a.s.l., again the years 1985, 1999, 2000, 2003 and 2005 have similar snow cover extents, while the snow areas in the other years are smaller, similar to the observation made at the highest elevations in the Stubai Alps.
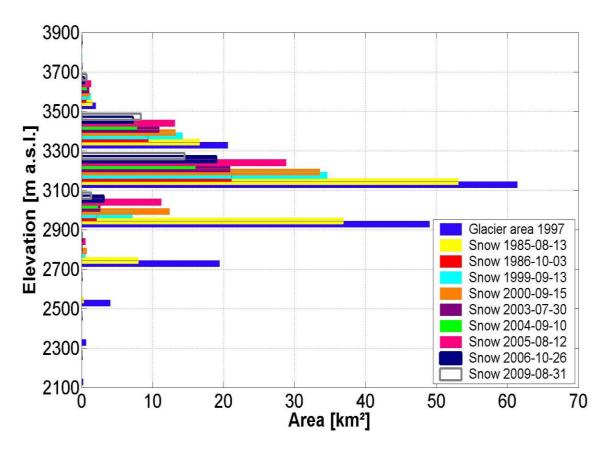
Figure 5.18: Area altitude distribution of snow areas in several years between 1985 and 2009 and the total glacier area of the Ötztal Alps, Austria. Elevations are derived from the national DEM, and areas are grouped into 200 m elevation intervals.
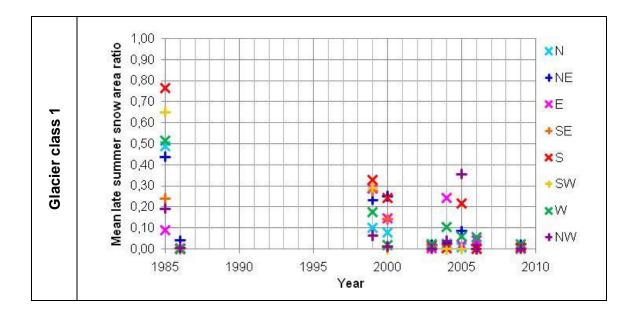
The retrieved late summer snow area extent in 1986 is in many elevation intervals similar to that derived in end of July in 2003. The difference to the late summer snow area extent in 1986 compared to 1985 is thus large, but not that large as in the Stubai Alps.

The major difference compared to the snow area extents of the Stubai Alps might be observed for the years 2004 and 2005, when the snow area extents derived for the Ötztal Alps are not affected by data gaps of the used Landsat scene. The derived late summer snow areas in the discrete elevation intervals in 2004 are similar to these derived in 2006, with one larger difference in the extents between 3100 m a.s.l. and 3300 m a.s.l.. In this elevation interval also the major difference is found for the snow areas retrieved from the scene of 2005, which shows in the other elevation intervals similarities to the snow area extent derived for the year 2000.

The other annual changes are in principle the same as for the Stubai Alps, and are thus not repeated here, while the presented area altitude distribution reflects the results.

The graphics in Figure 5.19 show the time series of the mean LSSAR on glaciers in the Ötztal Alps, Austria, in dependence of the individual glacier sizes and the main glacier aspects. The individual LSSARs for glaciers of class 1 and 2 of all orientations cover in most of the years a broad range of the snow area ratios. But the temporal variation of the mean LSSAR for glaciers with different orientations reflects in most cases the temporal distribution of the overall LSSAR for the Ötztal Alps. Only one glacier, the north orientated Gepatschferner, belongs to glacier class 4. The snow area ratios in 1985, 2003 and 2005 reflect the early image acquisition dates of the Landsat scenes. As previously mentioned, the snow areas in the end of the summer in these years were significantly smaller, especially in 2003.

Comparatively high mean snow area ratios were found for southwest orientated glaciers of class 2 and southeast orientated glaciers of class 3 in many of the investigated years.
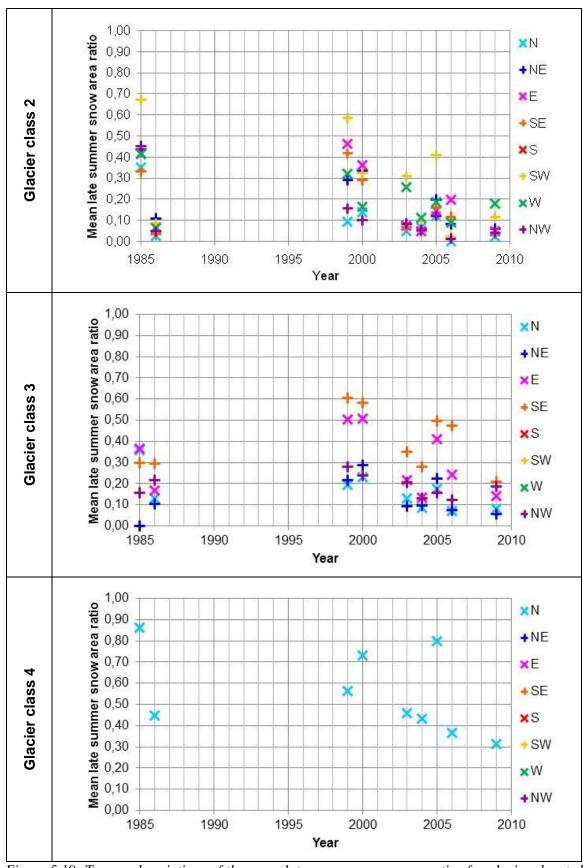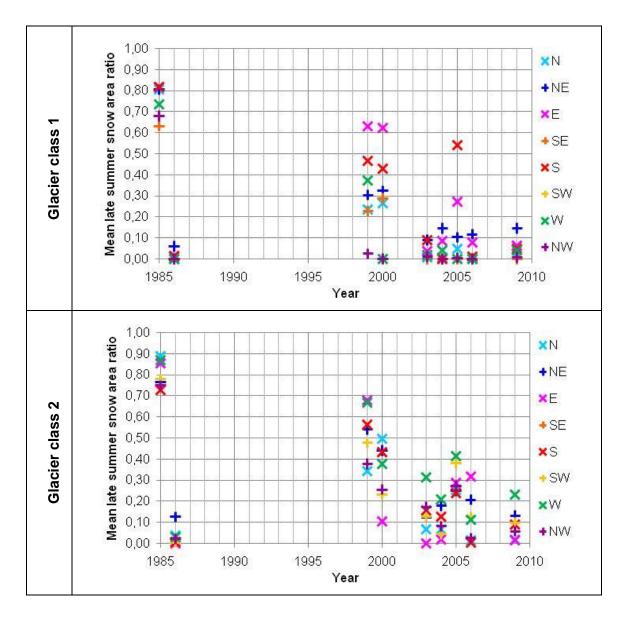
Figure 5.19: Temporal variations of the mean late summer snow area ratios for glaciers located in the Ötztal Alps, Austria, considering the glacier areas and the main glacier aspects.

The graphics in Figure 5.20 show the mean late summer snow area ratios for glaciers in the Stubai Alps with different orientations and sizes. Also for the glaciers in the Stubai Alps the general trend of the LSSAR can be observed in the mean LSSARs of glaciers with different orientations, although the individual LSSARs of glaciers belonging to class 1 and 2 cover a broad value range in most of the years. It might be surprising that southern orientated glaciers of all classes have relatively high LSSARs in most of the investigated years. Low mean snow area ratios were found for southwest orientated glaciers of class 3, while these of class 2 are in some years relatively high compared to those of glaciers with other orientations. Since 2003, also north and northwest orientated glaciers of class 3 have low mean snow area ratios. The mean LSSARs of northeast orientated glaciers in this class are comparatively high. Southeast orientated glaciers only occur in glacier class 1 in the Stubai Alps and have in most of the investigated years low snow area ratios. East and west orientated glaciers in the Stubai Alps occur in the glacier classes 1 and 2, showing large variations of the mean LSSARs in the investigated years.
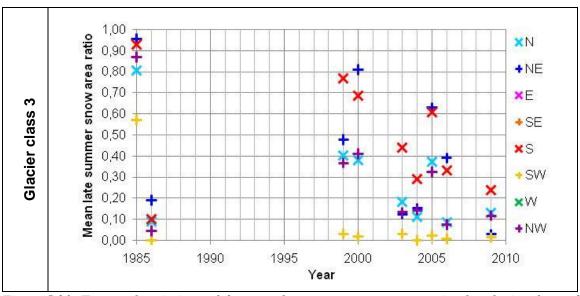
Figure 5.20: Temporal variations of the mean late summer snow area ratios for glaciers located in the Stubai Alps, Austria, considering the glacier areas and the main glacier aspects.

5.2.3 Barnes Icecap, Canadian Arctic

Although some long-term mass balance records exist in the western Canadian Arctic, there were no systematic observations of glacier mass balances (ACIA, 2005).

Sensor	Path / Row	Image acquisition date	DEM	Applied threshold	Late summer snow area [km²]	Glacier area [km²]	LSSAR
L5 TM	025 / 011	09/08/2010	GETASSE	0.42	51.79	5899.22	0.01
L5 TM	024 / 011	02/08/2010	GETASSE	0.58	404.04	5899.22	0.07
L7 ETM+	025 / 011	08/08/2001	GETASSE	0.26	904.02	5899.22	0.15
L5 TM	025 / 011	20/07/1991	GETASSE	0.47	1743.41	5899.22	0.30
L5 TM	025 / 011	18/08/1990	GETASSE	0.54	2142.37	5899.22	0.36
L5 TM	024 / 011	28/07/1985	GETASSE	0.40	2288.91	5899.22	0.39

Table 5.11: Investigation of late summer snow areas on the Barnes Icecap in several years between 1985 and 2010 based on Landsat imagery and using GETASSE DEM for the processing line.

As records of mass balances are based on point measurements, the derived summer snow area extents from the Landsat data enable the observation of the surface of the total icecap for selected years since 1985. The results are summarized in Table 5.11.

At the Barnes Icecap a continuous decrease of the derived LSSARs can be observed for the investigated years. Between 1991 and 2001, the derived LSSAR halved. Between 2001 and 2010, about the same loss of the derived late summer snow area can be observed, as occurred between 1991 and 2001. In 2010, two scenes meeting the requirements are available, acquired with only one week delay. Within this week, the derived snow area was reduced by about 350 km², which corresponds to a decrease in the LSSAR of 0.06.
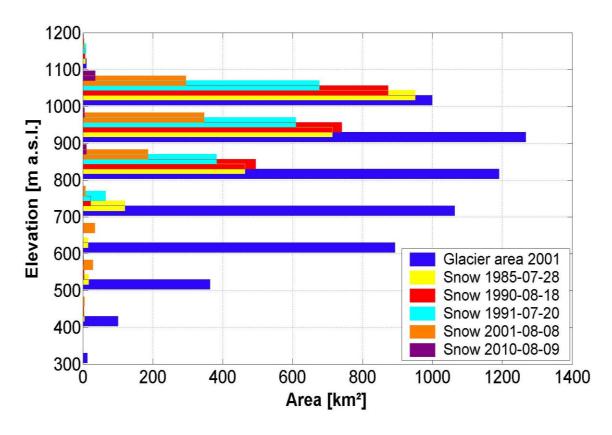

Figure 5.21: Area altitude distribution of snow areas of several years between 1985 and 2010 and the glacier area of the Barnes Icecap. Elevations are derived from the GETASSE DEM, and areas are grouped into 100 m elevation intervals.

The drastic reduction of the snow areas compared to that derived in 1985 started in 1990 at elevations above 1000 m a.s.l., while the snow area extents between 800 m a.s.l. and 1000 m a.s.l. were still larger in 1990 than in 1985. Between 1990 and 1991, the largest differences in the snow area extents occurred in elevations between 800 m a.s.l. and 1100 m a.s.l., where the snow area of 1991 was significantly smaller than in 1990, although the scene of 1991 was already acquired about a month earlier compared to that of 1990. This

fact is only visible between 700 m a.s.l. to 800 m a.s.l., where the snow area in 1991 was larger than in 1990. In 2001, some snow areas remained below 700 m a.s.l., which also was observed only in 1985, and for a few very small areas in 1990. The snow area between 700 m a.s.l. and 800 m a.s.l. indeed was almost the lowest of the selected years. Only in 2010 no snow remained in this elevation interval. Between 800 m a.s.l. and 1000 m a.s.l., the derived snow area in 2001 were cut in halve compared to 1991, and above the area loss was even larger. The small remaining snow covered areas in 2010 are found between 900 m a.s.l. and 1200 m a.s.l., with the main part between 1000 m a.s.l. and 1100 m a.s.l..

While some results about geospatial and elevation changes on the Barnes Icecap were published during the last years, e.g. by Abdalati et al. (2004), the investigation of the glacier surface over a longer temporal scale is new. The reported elevation changes on the icecap are largest on the margins, but occur at all elevations (Armenakis, 2008). The derived time series of the late summer snow area extent confirms the conclusions drawn from the observed and measured thinning of the icecap since mid of the 1980's at all elevations, as reported by Sneed et al. (2008). The snow mass reserves on the dome of the icecap saving the glacier ice beneath are almost gone in late summer 2010 (cf. Figure 5.22). If the reduction of the snow area on the centre of the icecap continues, increased melting of the glacier ice can also occur on the dome of the Barnes Icecap. Figure 5.22 illustrates the decrease of the derived late summer snow area ratios on the Barnes Icecap since 1985 using the blue marked data of Table 5.11.
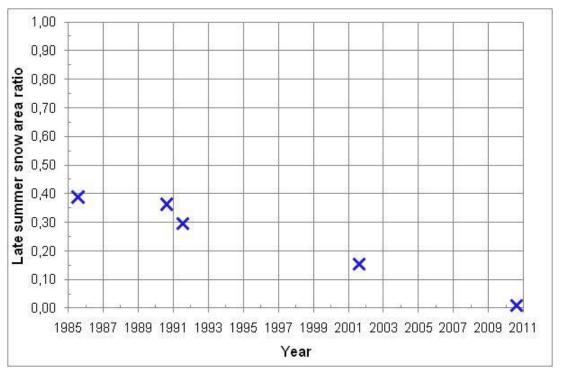
Figure 5.22: Variation of the late summer snow area ratio on the Barnes Icecap, Canadian Arctic, between 1985 and 2010 derived by the standard processing line from Landsat imagery. Only the blue marked dates of Table 5.11 are used in this graphic.

The long-term mean and monthly anomalies of the reanalysis air temperature data and the surface precipitation rate of the NCEP / NCAR were used to find relations between the derived LSSAR and meteorological and climatological conditions, respectively. Air temperatures of the ground pressure levels 1000 mb and 925 mb are used in order to approximate the low and high elevation zones of the Barnes Icecap. The subset shown in Table 5.12 covers the area between 68°N – 73°N, 67°W – 77°W, including the central part of the Baffin Island. The investigated Barnes Icecap is located approximately in the centre of this subset. Landsat scenes of the Barnes Icecap meeting the requirements were only acquired in July and August. The mean monthly temperatures at sea level, approximated by the 1000 mb ground pressure level, range between about 4°C and 6°C, with slightly warmer mean temperatures in July. The ground pressure level 925 mb was used to approximate the high elevation zone of the Barnes Icecap. The long-term mean temperatures in this elevation zone range between 4°C and 5°C in July and between 2°C and 3°C in August. The long-term mean surface precipitation rates are small in both month, with values between 0.75 mm/day and 1.25 mm/day.
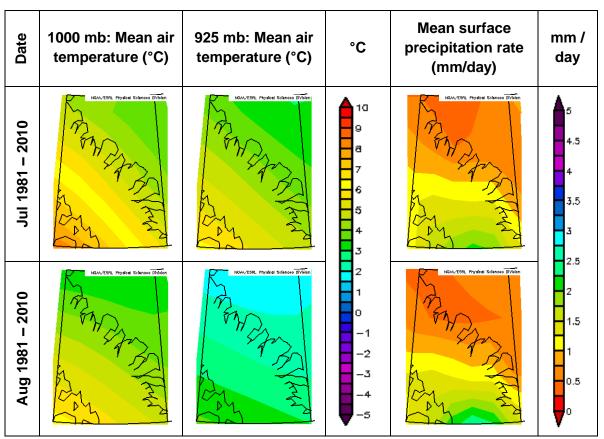
Table 5.12: Long term (1981 – 2010) mean monthly air temperature in °C on the ground pressure levels 1000 mb and 925 mb, approximating the lowest and the highest elevation zone of the Barnes Icecap in the Canadian Arctic, and mean surface precipitation rates in mm/day for July and August from the NCEP / NCAR Reanalysis (U.S. Department of Commerce, 2011).

The graphics in Table 5.13 show the anomalies of the air temperature in °C at the ground pressure levels 1000 mb and 925 mb, as well as of the surface precipitation rate in mm/day.

Date	1000 mb air temperature (°C) composite anomaly	925 mb air temperature (°C) composite anomaly	°C	Surface precipitation rate (mm/day) composite anomaly	mm / day
Jul 1985					
Aug 1990					
Jul 1991					
Aug 2001					
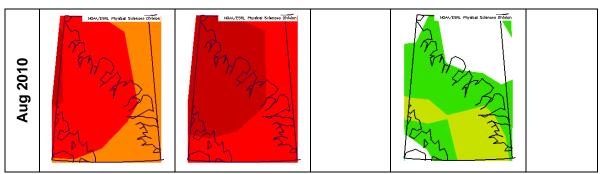
Table 5.13: Air temperature (°C) anomalies on the ground pressure levels 1000 mb and 925 mb, approximating the lowest and the highest elevation zone of the Barnes Icecap on the Baffin Island in the Canadian Arctic, and surface precipitation rate (mm/day) anomalies for the months when Landsat images were investigated. Graphics are from the NCEP / NCAR Reanalysis (U.S. Department of Commerce, 2011).

The surface precipitation rate anomalies are for all investigated months slightly negative at the location of the Barnes Icecap. The temperature anomalies on both ground pressure levels are positive in all investigated months except in August 1990. Since August 1990, the temperature anomalies in the investigated months continuously increased in both pressure levels. In August 2010 positive temperature anomalies of 3.5°C to more than 4°C were measured at both elevation ranges on the Barnes Icecap. These temperature anomalies are clearly reflected in the derived LSSARs.

5.2.4 North Patagonian Icefield, Chile

The late summer snow area extents derived for the North Patagonian Icefield in Chile since 1985 show variations in the investigated years, but no clear trend, as illustrated in Figure 5.23. This is in contrast to the previously discussed results for the Barnes Icecap in the Canadian Arctic.

In three of the investigated years, in 1985, 2000 and 2010, the scenes were acquired at about the same date in March, and the derived LSSARs for these scenes are very similar, between 0.43 and 0.45. This pattern can also be observed for scenes acquired in mid of February in the years 1987, 2002, and 2010, but with generally higher values for the LSSAR. Both scenes acquired in 2010 have indeed some data gaps due to the failure of the scan line corrector of the Landsat 7 ETM+ sensor. For the investigation of the snow and the glacier area, only valid pixels of these scenes are used. Thus, the derived snow area extents are underestimated for both dates in 2010. The error in the LSSAR due to the missing data in March 2010 is about 0.02.

The only scene acquired in mid of May is available in 2003. The derived LSSAR for this scene is not significantly lower than those derived from scenes acquired in March.

In Table 5.14 the derived snow area extents and the associated LSSARs are summarized. For both scenes of 2010, glacier and snow areas obscured by data gaps due to the SLC OFF modus are not included. The derived LSSARs can thus not directly be compared to these derived for the other years.

Sensor	Path / Row	Image acquisition date	DEM	Applied threshold	Snow covered area [km²]	Glacier area [km²]	LSSAR
L7 ETM+ (SLC OFF)	232 / 092 & 093	04/03/2010	SRTM	0.34	1736.19	4001.46	0.43
L7 ETM+ (SLC OFF)	232 / 092 & 093	16/02/2010	SRTM	0.36	2408.37	4003.96	0.60
L7 ETM+	232 / 092 & 093	20/05/2003	SRTM	0.54	1666.95	4138.26	0.40
L7 ETM+	232 / 092 & 093	10/02/2002	SRTM	0.70	2221.80	4138.26	0.54
L7 ETM+	232 / 092 & 093	08/03/2000	SRTM	0.54	1877.79	4138.26	0.45
L5 TM	232 / 092 & 093	09/02/1987	SRTM	0.58	2349.66	4138.26	0.57
L5 TM	232 / 092 & 093	07/03/1985	SRTM	0.58	1766.88	4138.26	0.43

Table 5.14: Temporal variation of the late summer snow areas and the associated late summer snow area ratios on the North Patagonian Icefield, Chile, derived from Landsat imagery and the DEM of SRTM. The images of 2010 are affected by data gaps in the Landsat images due to the failure of the scan line corrector, resulting in reduced extents of both the glacier area and snow covered area.

Indeed, an averaged AAR of 0.68 for all glaciers of the North Patagonian Icefield as estimated by Rivera et al. (2007) based on a Landsat 7 ETM+ scene of March 2001 was not derived in any of the investigated years. Rasmussen et al. (2007) investigated the influences of upper air conditions on the Patagonian Icefields between 1960 and 1999 based on data of the NCEP-NCAR project (Kalnay, 1996). For the years 1985 and 1987 Rasmussen et al. (2007) reported summer temperatures of about 2°C at 850 mb at 50°S, 75°W, while the summer temperature in 1986 at this level was significantly lower with only about 0.5°C. This might explain the higher LSSAR in 1987, when more snow

remained from the previous winter and also from summer snowfall, abating the melting process. During the period 1984 to 1999, the reported summer temperatures at 850 mb for this location varied around 2°C with a root mean square of 0.6°C.

These reported temperatures are about in the middle of the NCEP / NCAR Reanalysis temperature data at 1000 mb and 700 mb, shown in Table 5.15. The graphics in Table 5.15 show the long-term (1981 – 2010) mean air temperatures and mean surface precipitation rates in February, March and May. The shown subset covers the area between 42°S – 53°S, 65°W – 80°W. The investigated North Patagonian Icefield is located approximately in the centre of this subset. The long-term mean air temperatures range between about 15°C at 1000 mb in February and March and -9°C at 700 mb in May. Mean surface precipitation rates between 6 mm/day and 9 mm/day are found along the coast of Chile, reducing slightly further inwards, where the NPI is located.

| Date	1000 mb: Mean air temperature (°C)	700 mb: Mean air temperature (°C)	°C	Mean surface precipitation rate in mm/day	mm / day
Feb 1981 – 2010					
Mar 1981 – 2010					
May 1981 – 2010					
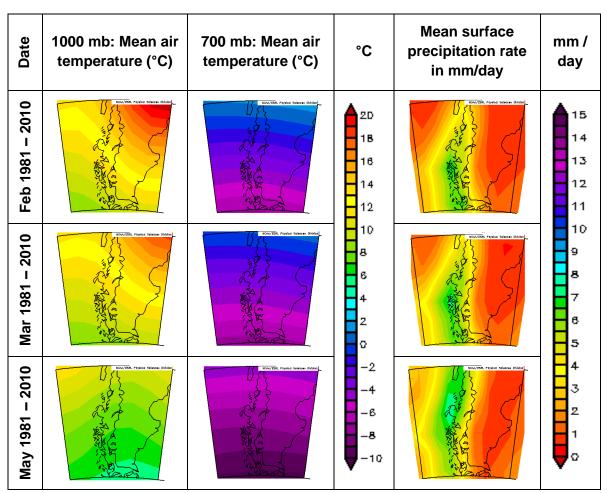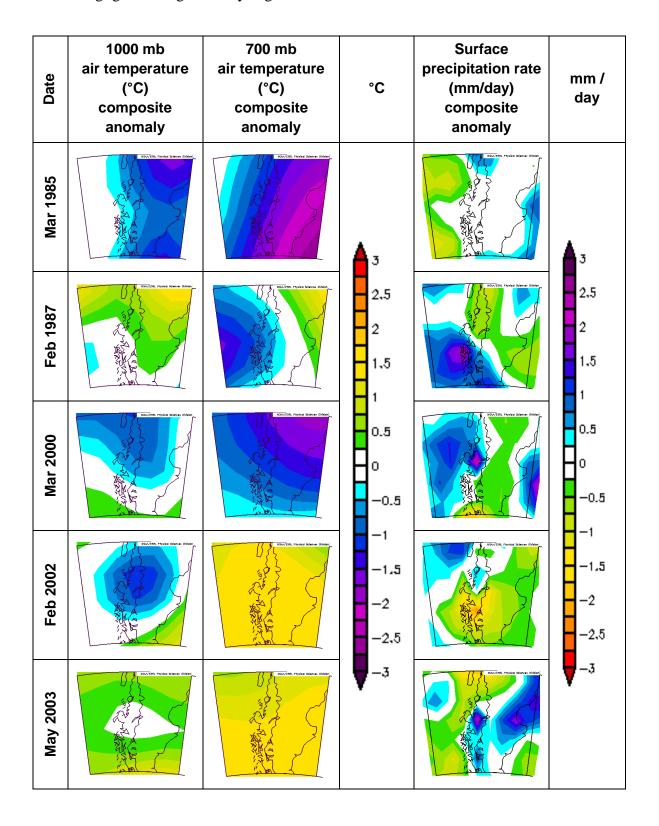
Table 5.15: Long term (1981 – 2010) mean monthly air temperature in °C on the ground pressure levels 1000 mb and 700 mb, approximating the lowest and the highest elevation zone of the North Patagonian Icefield in Chile, and mean surface precipitation rates in mm/day for July and August from the NCEP / NCAR Reanalysis (U.S. Department of Commerce, 2011).

In Table 5.16 the anomalies of the long-term mean air temperatures at 1000 mb and 700 mb and of the surface precipitation rate are listed. Positive temperature anomalies are observed for February 2002, May 2003 and March 2010 at the ground pressure level 700 mb. At 1000 mb and in the other investigated months, the temperature anomalies are either negligible or significantly negative.

| Date	1000 mb air temperature (°C) composite anomaly	700 mb air temperature (°C) composite anomaly	°C	Surface precipitation rate (mm/day) composite anomaly	mm / day
Mar 1985					
Feb 1987					
Mar 2000					
Feb 2002					
May 2003					
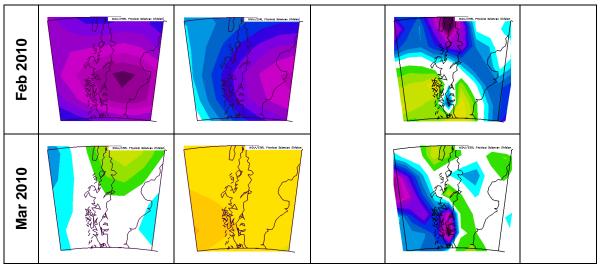
Table 5.16: Air temperature (°C) anomalies on the ground pressure levels 1000 mb and 700 mb, approximating the lowest and the highest elevation zone of glaciers of the North Patagonian Icefield in Chile, and surface precipitation rate (mm/day) anomalies for the months when Landsat images were investigated. Graphics are from the NCEP / NCAR Reanalysis (U.S. Department of Commerce, 2011).

The early image acquisition dates in 1987, 2002 and February 2010, combined with negative temperature anomalies in 1987 and 2010 are reflected in the high values of the derived snow areas. The warm temperature anomaly in March 2010 might be partly compensated by a large positive surface precipitation rate anomaly in this month. The retrieved snow area ratio for this month is in the same range as these of the other scenes acquired in March. Figure 5.23 shows the derived LSSARs of the investigated years since 1985.

For the South Patagonian Icefield (SPI), with the northernmost glacier located about 80 km south of the NPI, generally higher AARs are reported in the literature. Aniya et al. (1996) reported an AAR of 0.75 for the SPI, while De Angelis et al. (2007) found almost the same value, an AAR of 0.74, based on a Landsat image of March 2001. These values indicate no significant change of the late summer snow area extent at the image acquisition dates, and in general larger snow covered areas related to the total glacier area on the SPI compared to the NPI. However, direct interpretation in terms of mass balance is not possible, because SPI has an even higher percentage of calving glaciers than NPI.

The distribution of the late summer snow area extents per altitude interval are similar for the February, as well as for the March and the May scenes, respectively. The area altitude distribution of the late summer snow and the glacier areas per 200 m are illustrated in Figure 5.24. The largest differences for the February scenes are at elevations between 800 m a.s.l. and 1400 m a.s.l.. In this elevation range, the snow area extent in 1987 is significantly larger than that in 2002, when the used Landsat image was acquired at about the same date. Between 1400 m a.s.l. and 1600 m a.s.l. the late summer snow area extent

is about equal in both years. Between 1600 m a.s.l. and 2400 m a.s.l. the late summer snow area extent is larger in 2002 than in 1987. Above 2400 m a.s.l. the derived late summer snow area extents per elevation interval are about equal in both years.
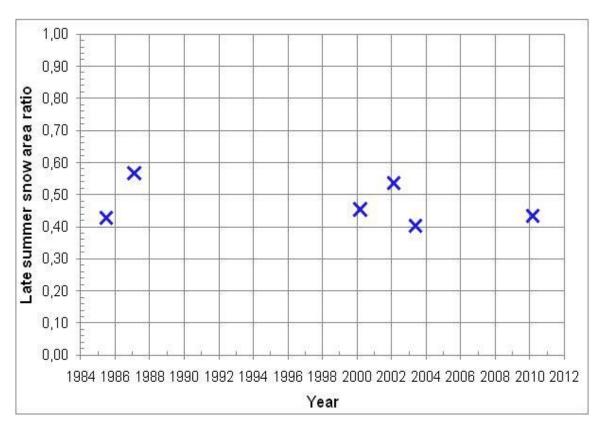
Figure 5.23: Late summer snow area ratios derived from Landsat imagery from mid-1980's to 2010 for the North Patagonia Icefield. The late summer snow area ratio value of 2010 is related to a smaller glacier area (ca. 4001 km²) due to gaps in the Landsat scene caused by the failure of the Scan Line Corrector. Only the blue marked dates of Table 5.14 are used for this graphic.

The inter-annual differences for the March scenes are larger, and occur in a broader elevation range, mainly between 800 m a.s.l. and 2800 m a.s.l.. In March 1985 and 2010, equal LSSARs were derived. But considering, that the late summer snow area extent derived from the 2010 scene is underestimated due to the data gaps caused by the SLC failure, these both values cannot directly be compared. This is also obvious in the late summer snow area altitude distribution in 1985 and 2010, which shows significant differences between 800 m a.s.l. and 2200 m a.s.l.. In 2010, relatively large areas below 1200 m a.s.l. are still covered by snow, while in 1985 more snow remained above 1200 m a.s.l. compared to 2010. The late summer snow area extent in 2003 is in most elevation intervals between the snow area extents of March 1985 and 2010, while the snow area extent in 2000 is lower below 1200 m a.s.l., but also partly significantly higher at higher elevations.

151
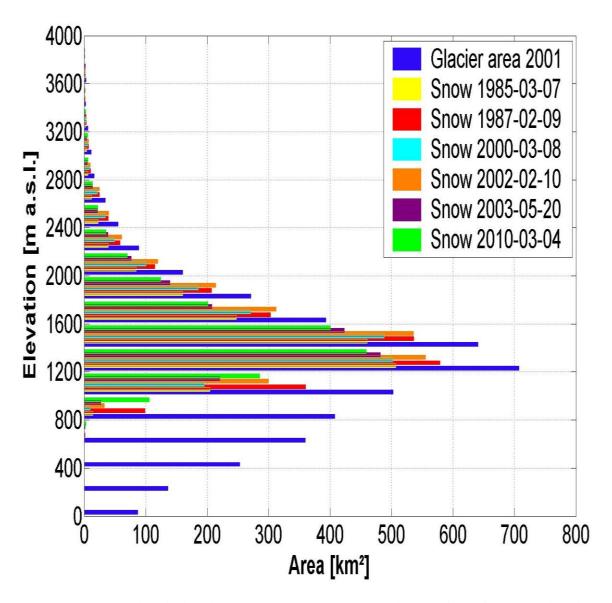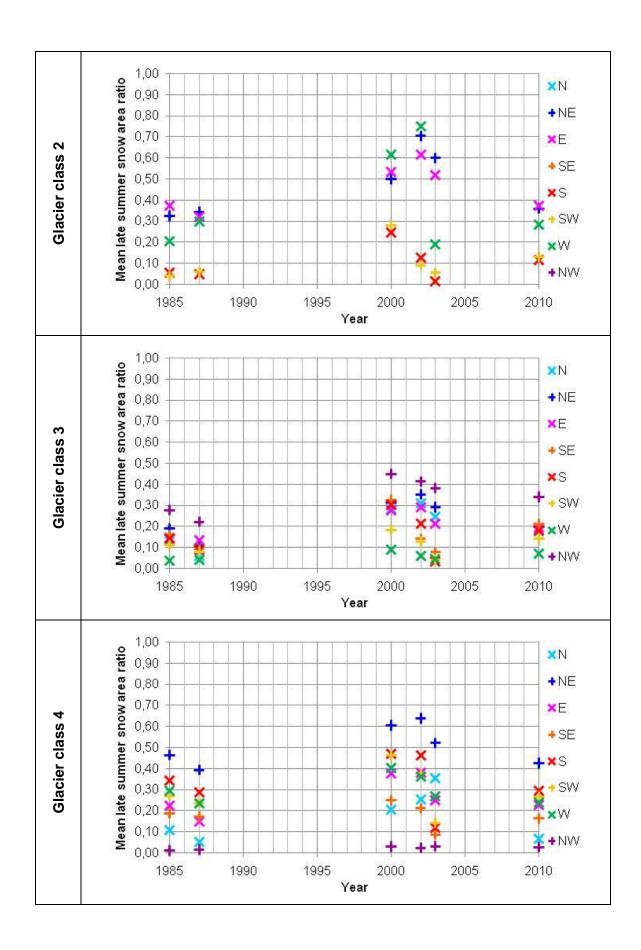
Figure 5.24: Area altitude distributions of snow areas of several years, derived from Landsat data from 1985 to 2010, and the glaciers of the North Patagonian Icefield. Elevations are derived from the DEM of SRTM, and areas are grouped into 200 m elevation intervals.

Based on a Landsat 7 ETM+ scene of 2001, Rivera et al. (2007) reported an average AAR of 0.68 for all glaciers of the North Patagonian Icefield, with higher AAR values for east orientated glaciers on the North Patagonian Icefield, and smaller values for north orientated glaciers. The individual AARs vary thereby between 0.41 for the north orientated Bayo glacier, and 0.90 for the eastward orientated glacier U-7. These results cannot be confirmed by the investigation of the individual glaciers of the North Patagonian Icefield since 1985 in dependence of the glacier area and the glacier exposition. But west and northeast orientated glaciers of the classes 2, 4 and 5, and northwest orientated glaciers of class 3 have rather high mean snow area ratios in many of the investigated years, as illustrated in Figure 5.25.
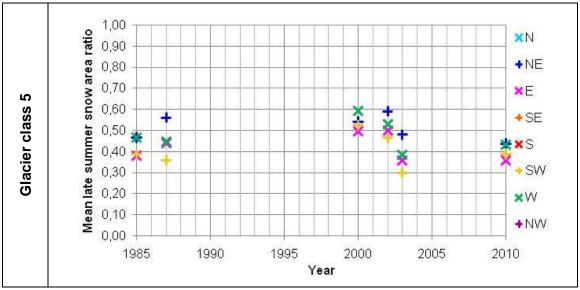
Figure 5.25: Temporal variations of the mean late summer snow area ratios for glaciers located on the North Patagonian Icefield, Chile, considering the glacier areas and the main glacier aspects.

5.2.5 Sagarmatha, Nepal

For the glaciers in the Sagarmatha basin in Nepal, most of the scenes selected for the investigation of the snow area extent between summer and winter monsoon in several years were acquired within 2 ½ weeks, from the end of October till the beginning of November. In 1992, only a scene acquired in September was available meeting the requirements. Due to the different climatic conditions in the Himalaya compared to the other selected regions, several additional scenes were processed, and the overall LSSARs were calculated. These results are listed in Table 5.17, and illustrated as red dots in Figure 5.26.

For the detailed studies on glaciers located in the Sagarmatha basin, only scenes taken between summer and winter monsoon are used, which are blue marked in Table 5.17.

Beside the scene of 1992, another scene was acquired end of September in the year 2000. The derived late summer snow area ratios indicate no significant change of the snow area extent between 1992 and 2000. The same can be observed for scenes acquired in mid of September in 2000 and 2009, showing very similar snow area extents in both years.

Comparing the marked scenes, a decrease of the snow area can be observed between 2002 and 2009, as also illustrated in Figure 5.26. The overall snow area extent in 2001 is about the same as in 2004, when the image was acquired about two weeks later in the year. Also for the scenes of 2000 and 2002, when the images were acquired with a delay of 10 days, very similar overall snow extents were derived.

Sensor	Image acquisition date	DEM	Applied threshold	Snow covered area [km²]	Glacier area [km²]	LSSAR
L5 TM	25/04/2010	VIEWFINDER	0.68	51.97	355.09	0.15
L5 TM	09/04/2010	VIEWFINDER	0.70	27.01	355.09	0.08
L5 TM	20/02/2010	VIEWFINDER	0.59	126.71	355.09	0.36
L5 TM	04/02/2010	VIEWFINDER	0.47	101.00	355.09	0.28
L5 TM	31/10/2009	VIEWFINDER	0.56	81.93	355.09	0.23
L5 TM	13/09/2009	VIEWFINDER	0.66	96.62	355.09	0.27
L5 TM	05/11/2005	VIEWFINDER	0.53	96.49	355.09	0.27
L5 TM	02/11/2004	VIEWFINDER	0.56	116.65	355.09	0.33
L7 ETM+	23/12/2002	VIEWFINDER	0.29	128.37	355.09	0.36
L7 ETM+	20/10/2002	VIEWFINDER	0.39	139.73	355.09	0.39
L7 ETM+	04/10/2002	VIEWFINDER	0.36	153.31	355.09	0.43
L7 ETM+	20/12/2001	VIEWFINDER	0.27	129.05	355.09	0.36
L7 ETM+	17/10/2001	VIEWFINDER	0.41	116.26	355.09	0.33
L7 ETM+	30/10/2000	VIEWFINDER	0.38	135.77	355.09	0.38
L7 ETM+	14/10/2000	VIEWFINDER	0.42	95.96	355.09	0.27
L7 ETM+	28/09/2000	VIEWFINDER	0.45	102.08	355.09	0.29
L7 ETM+	12/09/2000	VIEWFINDER	0.47	93.32	355.09	0.26
L4 TM	22/09/1992	VIEWFINDER	0.60	107.64	355.09	0.30

Table 5.17: Time series of snow area extent during pre- and post-monsoon ablation periods and associated snow area ratios for all glaciers in the Sagarmatha basin, Nepal, derived from Landsat imagery (Path 140 / Row 041). Blue coloured rows are used for the illustration of late summer snow area ratios in Figure 5.26.

The additionally investigated scenes illustrate the strong dependence of the late summer snow area extent on meteorological conditions. The scenes acquired in 2010 show the variation of the snow area extent between winter and summer monsoon, with a strong melting period between mid of February and mid of April. Two scenes acquired in the beginning of the winter monsoon in 2001 and 2002 show almost equal snow area extents.
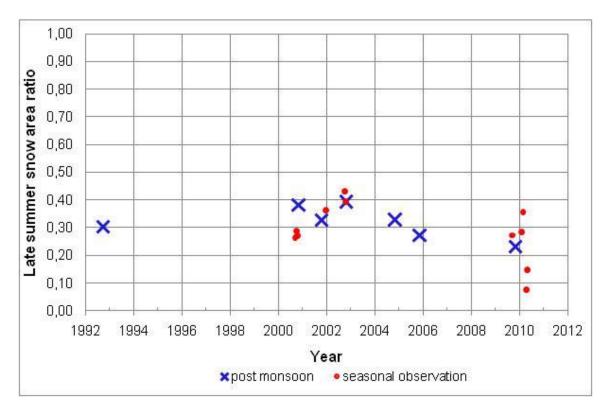
Figure 5.26: Temporal variation of the snow area ratios on the glaciers in the Sagarmatha basin, derived by the standard processing line from Landsat imagery between 1992 and 2009. The blue marked dates of Table 5.17 are illustrated as blue crosses, the additionally derived LSSARs showing seasonal variations are printed as red dots in this graphic.

Analysing the snow area ratios of the selected years on the largest glaciers of the Sagarmatha basin, with total areas between 10 km² and 100 km², results in partly different variations in some of the years, as shown in Figure 5.27. The derived snow area ratios between summer and winter monsoon for the Khumbu glacier vary between 0.20 and 0.39 and for the Imja glacier between 0.19 and 0.27, with a significant decrease in the snow area between 2002 and 2009. These values are significantly lower than the equilibrium AARs of 0.54 and 0.55 suggested by Owen and Benn (2005) for the Khumbu and the Imja glacier, respectively. Also the time series of the other LSSARs of glaciers of this class in the Sagarmatha basin indicate a clearly negative mass balance trend. The Melung glacier, with the lowest snow area ratios in all years, is southeast orientated, and the Imja glacier, with also relatively low snow area ratios compared to the other glaciers, has a west exposition. All other glaciers of this class in the Sagarmatha basin are south orientated. The Ngojumba glacier is the largest glacier in this basin, and has also the highest values of the snow area ratios in this glacier class in all investigated years. The overall trend to smaller snow areas between summer and winter monsoon is clearly represented by all of these glaciers.
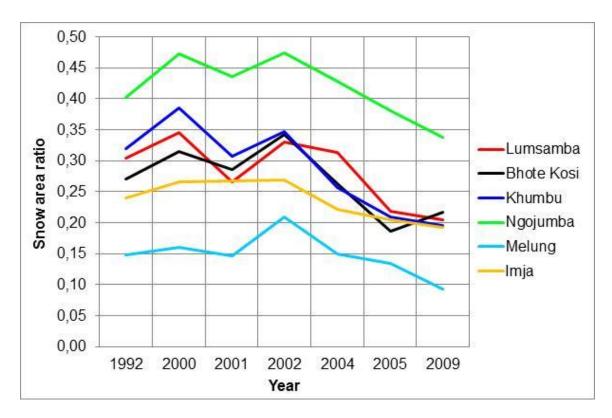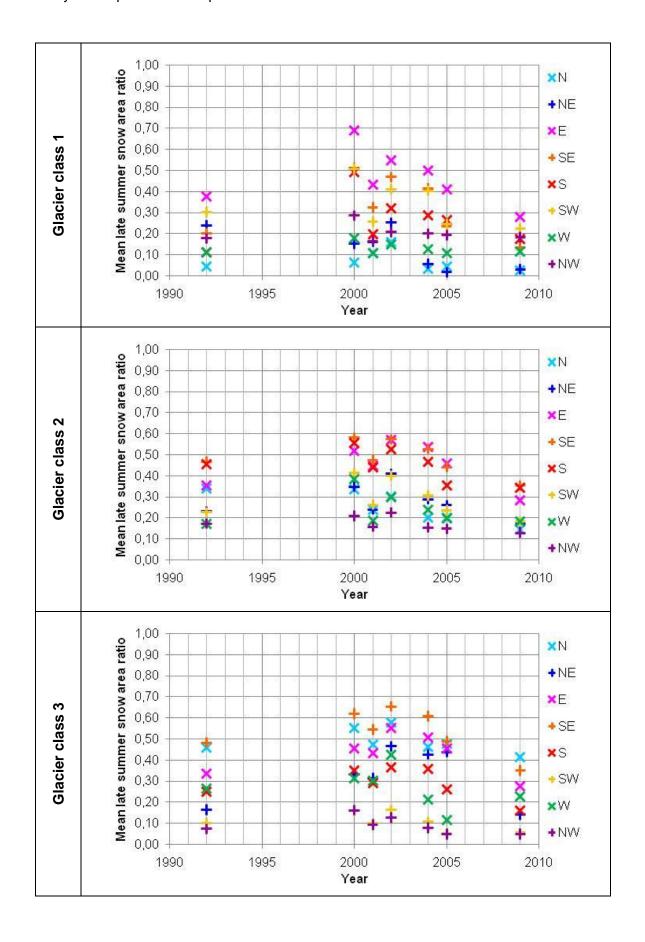
Figure 5.27: Temporal variation of the snow area ratios between summer and winter monsoon for glaciers with a total area between 10 km² and 100 km² located in the Sagarmatha basin.

Investigations of the mean snow area ratios between summer and winter monsoon in these years for glaciers of different sizes and aspects result also in the trend of smaller snow areas since 2002 in all glacier classes, as illustrated by the graphics in Table 5.18. The aspect with the largest snow areas varies with the glacier size. For glaciers of classes 1, 2 and 3 east and southeast orientated glaciers have the largest remaining snow areas in most of the years. Southwest orientated glaciers of class 1 and south orientated glaciers of class 2 have also relatively high mean LSSARs on the investigated dates. Two north orientated glaciers of class 3 have relatively large remaining snow areas in all investigated years, while smaller north orientated glaciers have rather low snow area ratios. Northwest orientated glaciers of class 2 and 3 have small remaining snow areas, and west orientated glaciers of all classes have relatively low snow area ratios. Northeast orientated glaciers of class 1 have low snow area ratios in most of the years, especially since 2004, while glaciers of class 2 and 3 have relatively large remaining snow areas compared to glaciers with other aspects. The southeast and the west orientated glaciers of class 4 are illustrated in Figure 5.27, and are already discussed in detail. Also the mean LSSARs of the south orientated glaciers of this class are higher than the snow area ratios of the other two glaciers.
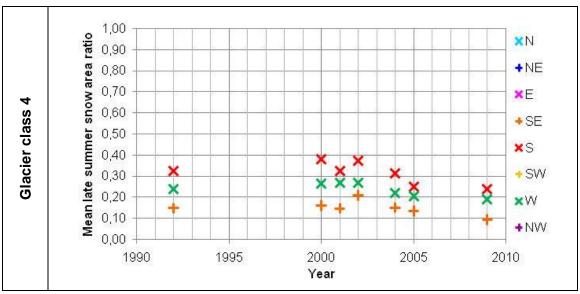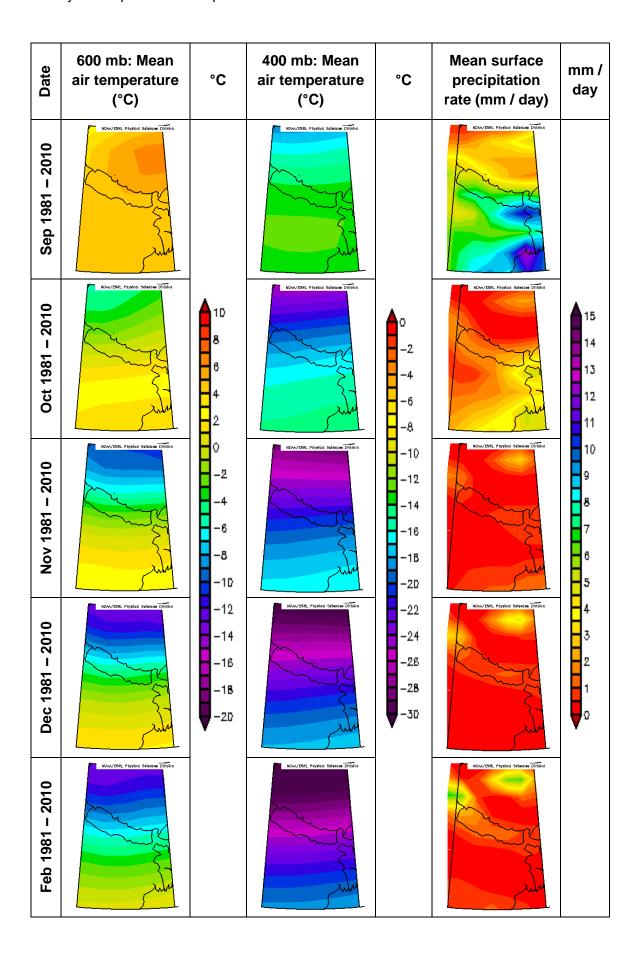
Table 5.18: Temporal variations of mean snow area ratios between summer and winter monsoon for glaciers located in the Sagarmatha basin, Nepal, considering the glacier areas and the main glacier aspects.

The NCEP / NCAR Reanalysis data of the mean air temperature at 600 mb and 400 mb are used to approximate the temperatures at the low and high elevation zones of the glaciers in the Sagarmatha basin (Table 5.19). The shown subset covers the area between 20°N – 35°N, 80°E – 90°E. The investigated Sagarmatha basin is located close to the northeast corner of Nepal, approximately in the centre of this subset. The long-term mean air temperatures and surface precipitation rates are shown for all months when Landsat images were investigated, including also February and April to cover the month between winter and summer monsoon. A clearly positive long-term mean air temperature can only be observed in September at the 600 mb ground pressure level. In October and April the long-term mean is around zero degree. Temperature anomalies at this elevation zone in these months might thus have the largest influences on the snow areas on the glaciers. In the remaining months, the mean temperatures are clearly negative. At the ground pressure level 400 mb, the observed long-term mean temperatures range between about -13°C and -26°C. Small positive temperature anomalies at this level might not have relevant effects on snow melt. Mean surface precipitation rates for these months show the largest rates in September with values up to 8 mm/day, rates between 3 mm/day and 4 mm/day in October and April, and rates smaller than 2 mm/day in the remaining months.

Anomalies of these long-term mean values for the investigated months are presented in Table 5.20. In September 1992 and 2000 slightly negative temperature anomalies were found at 600 mb, together with partly significantly negative precipitation rate anomalies. The temperature anomaly in September 2009 is slightly positive, but the negative precipitation rate anomaly was also found in this year. This explains the similar LSSARs derived from Landsat scenes acquired in September of several years.

Date	600 mb: Mean air temperature (°C)	°C	400 mb: Mean air temperature (°C)	°C	Mean surface precipitation rate (mm / day)	mm / day
Sep 1981 – 2010						
Oct 1981 – 2010						
Nov 1981 – 2010						
Dec 1981 – 2010						
Feb 1981 – 2010						

	Apr 1981 – 2010		
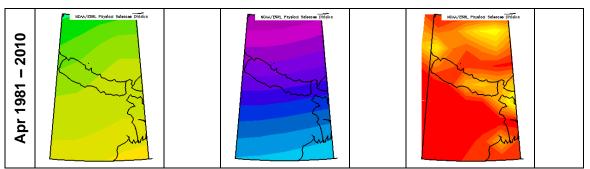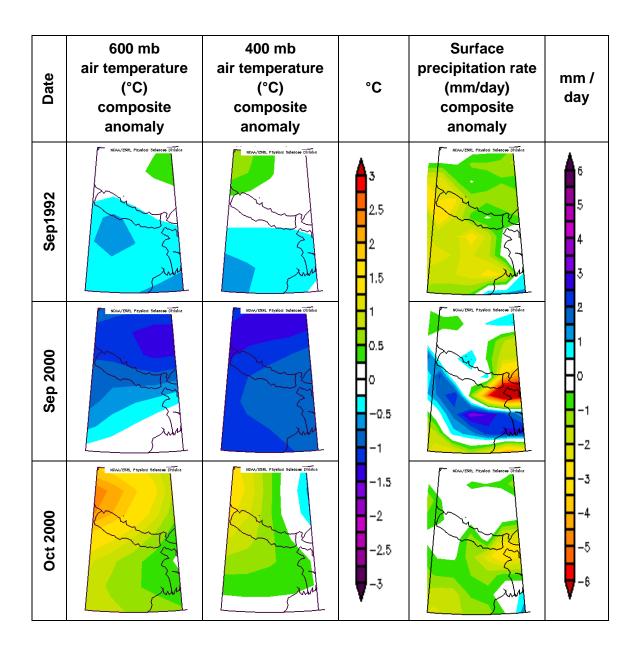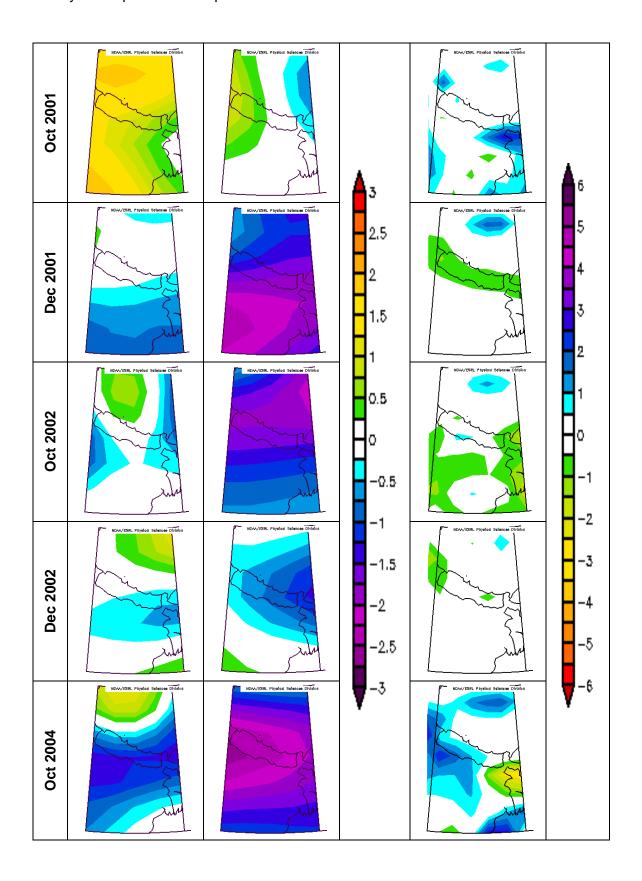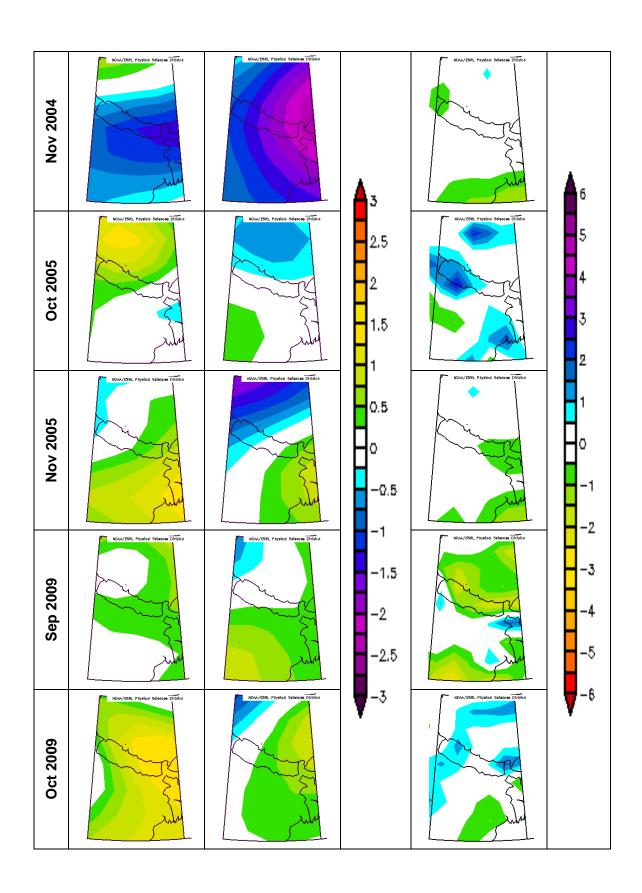
Table 5.19: Long term (1981 – 2010) mean monthly air temperature in °C on the ground pressure levels 600 mb and 400 mb, approximating the lowest and the highest elevation zone of the glaciers located in the Sagarmatha basin in Nepal, and mean surface precipitation rates in mm/day for September to December, February and April from the NCEP / NCAR Reanalysis (U.S. Department of Commerce, 2011).

Date	600 mb air temperature (°C) composite anomaly	400 mb air temperature (°C) composite anomaly	°C	Surface precipitation rate (mm/day) composite anomaly	mm / day
Sep1992					
Sep 2000					
Oct 2000					

Analysis of spatial and temporal variations in snow area
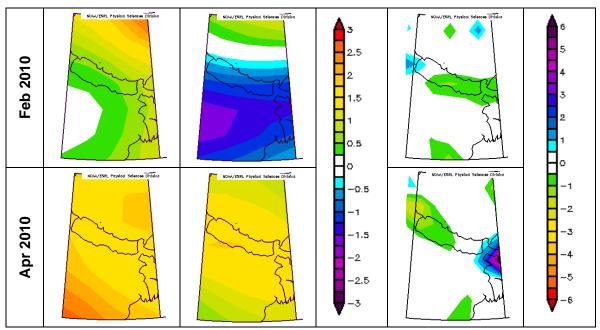
Table 5.20: Air temperature (°C) anomalies on the ground pressure levels 600 mb and 400 mb, approximating the lowest and the highest elevation zone of glaciers of the Sagarmatha basin in Nepal, and surface precipitation rate (mm/day) anomalies for the months when Landsat images were investigated. Graphics are from the NCEP / NCAR Reanalysis (U.S. Department of Commerce, 2011).

In October, the temperature anomalies over the Sagarmatha basin at 600 mb vary between about ±2°C. Precipitation anomalies of the investigated years when Landsat images were acquired in October were rather small. Since 2004, the temperatures anomalies at 600 mb in October of the investigated years became warmer. This is also reflected by the derived snow area ratios derived for scenes acquired in October or beginning of November. Temperature anomalies at 600 mb and precipitation anomalies in December 2001 and 2002 are in the same range between about -0.25° and -0.5°C, which also explains the equal snow area ratios retrieved for these two months.

In February and April 2010 positive temperature anomalies are found at 600 mb. Also the largest positive temperature anomaly at 400 mb was observed in April 2010 with about 1.5°C.

The area altitude distribution of the selected scenes presented in Figure 5.28 shows a continuously slight decrease of the late summer snow area extent above 6600 m a.s.l. per elevation interval since 2000. Between 5600 m a.s.l. and 6600 m a.s.l., the late summer snow area extents per elevation interval in 2001 are very similar to these of 2004. For the other years since 2000, the same decrease as in upper elevation intervals can be observed. The late summer snow area extents of 1992 in these elevation intervals are only slightly lower compared to these of 2001 and 2004. Below 5600 m a.s.l., the maximum late summer snow areas remained in the year 2002, which were about twice the late summer

snow area extent derived for the scene of 2009. Between 5400 m a.s.l. and 5600 m a.s.l. the largest late summer snow areas are found for the investigated scenes, while the peak in glacier area in the Sagarmatha basin is found between 5000 m a.s.l. and 5400 m a.s.l..

2004 is the only year, when late summer snow remained within the lowest elevation interval, between 4200 m a.s.l. and 4400 m a.s.l..
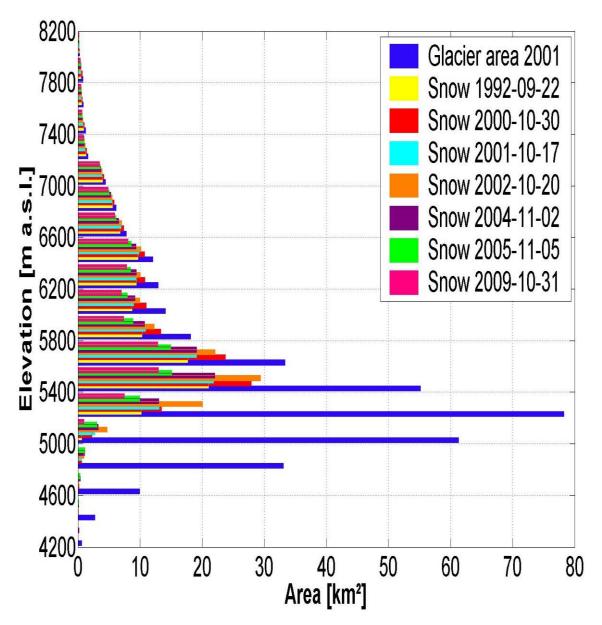
Figure 5.28: Area altitude distribution of snow areas in several years between 1992 and 2009 and the total glacier area in the Sagarmatha basin. Elevations are derived from the VIEWFINDER DEM, and areas are grouped into 200 m elevation intervals.

5.2.6 Svartisen and Blåmannsisen, Norway

The both regions Svartisen and Blåmannsisen are covered by one Landsat scene, but are influenced by different climate conditions. The glaciers of Svartisen are characterized by a maritime climate, while the climate at Blåmannsisen is more continental (Andreassen et al., 2005). Landsat images since the mid 1980's covering both regions were investigated. The individual results are presented in Table 5.21 for the glaciers on and around Svartisen, and in Table 5.22 on and around Blåmannsisen.

Region	Path / Row	Image acquisition date	DEM	Applied threshold	Late summer snow area [km²]	Glacier area [km²]	LSSAR
Svartisen	198 / 013	05/08/2010	National	0.44	305.24	531.52	0.57
	199 / 013	04/10/2006	National	0.47	114.73	531.52	0.22
	198 / 013	26/08/2006	National	0.45	154.53	531.52	0.29
	198 / 013	23/08/2002	National	0.33	165.09	531.52	0.31
	198 / 013	20/08/2001	National	0.53	110.05	531.52	0.21
	198 / 013	02/10/1999	National	0.62	79.66	531.52	0.15
	198 / 013	07/09/1999	National	0.51	191.35	531.52	0.36
	198 / 013	15/08/1999	National	0.48	349.26	531.52	0.66
	199 / 013	31/07/1994	National	0.42	448.61	531.52	0.84
	198 / 013	30/09/1984	National	0.50	360.12	531.52	0.68

Table 5.21: Overview on the investigations of late summer snow areas in several years between 1984 and 2010 on the glaciers in Svartisen derived from Landsat imagery, using the National DEM (25 m) for the processing line.

The overall derived LSSARs are higher for the glaciers of Blåmannsisen than for the glaciers on and around Svartisen, except in 2010. For three of the investigated scenes, acquired in 1994, 1999, and 2002, very similar LSSARs were derived for both regions, with each 0.04 higher LSSARs for Blåmannsisen compared to Svartisen. These scenes were acquired at different dates, from end of July in 1994 to beginning of October in

1999. In 2010, when the LSSAR for the glaciers of Svartisen was higher than for these of Blåmannsisen, the difference between the derived LSSARs for both regions is 0.06. In the other investigated years, the differences were significantly larger, with the derived LSSARs of Blåmannsisen being 0.16 to 0.17 higher than in Svartisen.

Region	Path / Row	Image acquisition date	DEM	Applied threshold	Late summer snow area [km²]	Glacier area [km²]	LSSAR
Blåmannsisen	198 / 013	05/08/2010	National	0.44	51.32	101.34	0.51
	199 / 013	04/10/2006	National	0.47	38.85	101.34	0.38
	198 / 013	26/08/2006	National	0.45	33.28	101.34	0.33
	198 / 013	23/08/2002	National	0.33	35.63	101.34	0.35
	198 / 013	20/08/2001	National	0.53	35.72	101.34	0.35
	198 / 013	02/10/1999	National	0.62	19.39	101.34	0.19
	198 / 013	07/09/1999	National	0.51	30.30	101.34	0.30
	198 / 013	15/08/1999	National	0.48	55.83	101.34	0.55
	199 / 013	31/07/1994	National	0.42	89.15	101.34	0.88
	198 / 013	30/09/1984	National	0.50	86.47	101.34	0.85

Table 5.22: Overview on the investigations of late summer snow areas for several years between 1984 and 2010 on the glaciers in Blåmannsisen derived from Landsat imagery, using the National DEM (25 m) for the processing line.

For the year 1999, three scenes with a time interval of three weeks between the acquisition dates, starting in the mid of August, were investigated. In both regions, the late summer snow area decreased significantly from date to date. In Svartisen, the snow area decreased to about a quarter of the snow area in the first image within six weeks. The decrease of the snow area between the image of September and October was slightly larger compared to that between August and September.

In Blåmannsisen the snow area decreased within six weeks to about a third of the area derived for the scene of mid of August. Different from Svartisen, the decrease of the

snow area on the glaciers of Blåmannsisen was significantly larger between the scenes of August and September than between September and October.

Also in 2006, two Landsat scenes acquired with a delay of five weeks were investigated. While the derived LSSARs were similar for the first scene in 2006 in both regions, the change to the LSSARs retrieved from the second image was different. In Svartisen, the snow area derived from the second scene was significantly lower than that retrieved from the earlier image. In Blåmannsisen, the scene of October showed a larger snow area than that of August, indicating, that a summer snow fall event occurred in this region between the image acquisition dates. These results illustrate the different meteorological influences on the glaciers of both regions, as well as the problem in obtaining the maximum snow depletion if only one image covering several glacier regions is available.

In Figure 5.29 the derived late summer snow area ratios of both regions in Norway are illustrated based on the blue marked cells of Table 5.21 and Table 5.22.
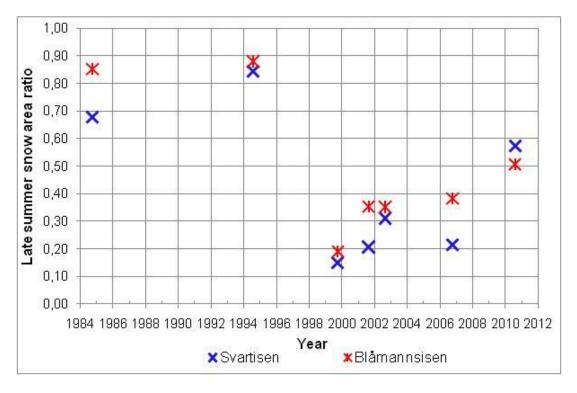
Figure 5.29: Temporal variations of the late summer snow area ratios for glaciers in Svartisen and Blåmannsisen, derived from Landsat imagery between 1984 and 2010. Only the blue marked dates of the Table 5.22 are used in this graphic.

In Table 5.23 the long-term mean monthly air temperatures for July to October at 1000 mb and 850 mb and the mean surface precipitation rates for these months are listed. The shown subset covers the region between 64°N – 70°N, 10°E – 20°E in northern Norway. The two regions Svartisen and Blåmannsisen are located approximately in the centre of this subset. Long-term mean temperatures at 1000 mb range between about 3°C and

14°C, while these at 850 mb range between about -3°C and 6°C, with the warmest month being July. Surface precipitation rates are similar in all months with about 1.5 mm/day to 2 mm/day.
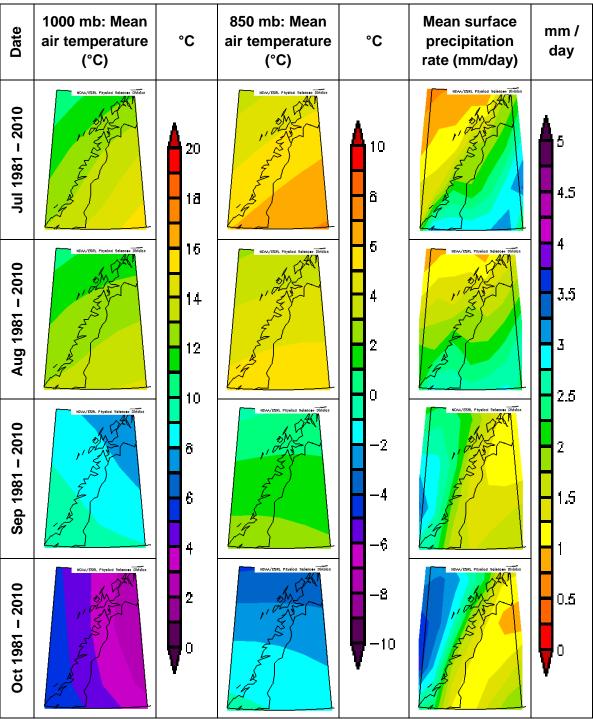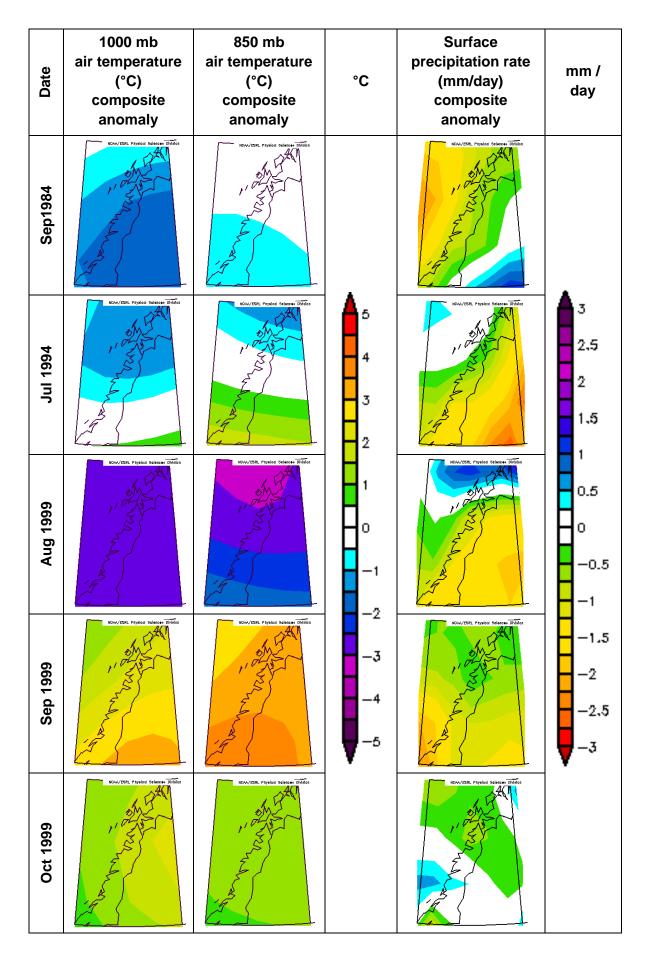
Table 5.23: Long term (1981 – 2010) mean monthly air temperature in °C on the ground pressure levels 1000 mb (left) and 850 mb (right), approximating the lowest and the highest elevation zone of the glaciers in northern Norway, and mean surface precipitation rates in mm/day for July to October from the NCEP / NCAR Reanalysis (U.S. Department of Commerce, 2011).
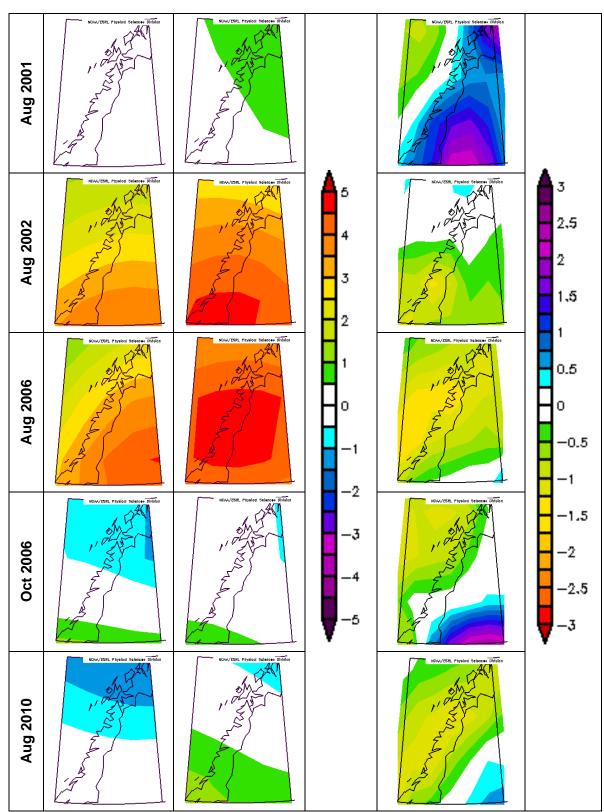
Table 5.24: Air temperature (°C) anomalies on the ground pressure levels 1000 mb and 850 mb, approximating the lowest and the highest elevation zone of glaciers of the two regions in northern Norway, and surface precipitation rate (mm/day) anomalies for the months when Landsat images were investigated. Graphics are from the NCEP / NCAR Reanalysis (U.S. Department of Commerce, 2011).

The graphics in Table 5.24 show the anomalies of the long-term means of the air temperature and the surface precipitation rate for the months when Landsat images were investigated. The largest positive temperature anomaly was observed in August 2006 with more than 3°C at 1000 mb and even more than 4.5°C at 850 mb, combined with a negative precipitation anomaly. In October 2006 the differences to the long-term means were negligible. Minor temperature deviations at the two ground pressure levels can be observed for September 1984, July 1994, August 2001 and August 2010. But relevant anomalies of the surface precipitation rate occur in most of the investigated months, except in October 1999.

The temporal variations of the derived LSSARs in both regions are also represented in the area altitude distributions of the snow areas on the investigated dates, illustrated in Figure 5.30 for the glaciers of the region Svartisen and in Figure 5.31 for the glaciers of Blåmannsisen.
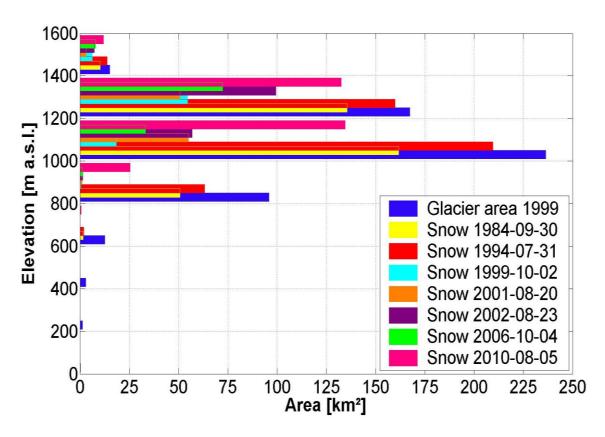
Figure 5.30: Area altitude distribution of snow areas of several years between 1984 and 2010 and area of all glaciers of and around Svartisen, Norway. Elevations are derived from the national DEM, and areas are grouped into 200 m elevation intervals.

The glacier areas of Svartisen are situated at slightly lower elevations than those of Blåmannsisen, ranging between sea level and about 1600 m a.s.l., with the main glacier area between 1000 m a.s.l. and 1400 m a.s.l.. In this elevation range also the main snow

covered areas are observed at all investigated dates. Below 800 m a.s.l., only in 1984, and in the two years with image acquisitions during midsummer, in 1994 and 2010, snow was observed. The snow areas derived for the years 2001 and 2002, when the investigated images were acquired on about the same date, are similar for the elevation interval 1000 m a.s.l. to 1200 m a.s.l., but show large differences between 1200 m a.s.l. and 1400 m a.s.l. with about twice the snow extent in 2002 compared to 2001 in this elevation interval. This might partly be caused by some cloud coverage on the eastern part of Svartisen in 2001 (cf. Section 4.2.7). The scenes acquired in the beginning of October, in 1999 and 2006, show also the largest differences between 1000 m a.s.l. and 1400 m a.s.l.. Below 1000 m a.s.l., the snow areas are negligible in these years. The described variations of the late summer snow area extents on the glaciers of Svartisen in the individual years are also valid for elevations above 1400 m a.s.l., but on a minor scale.
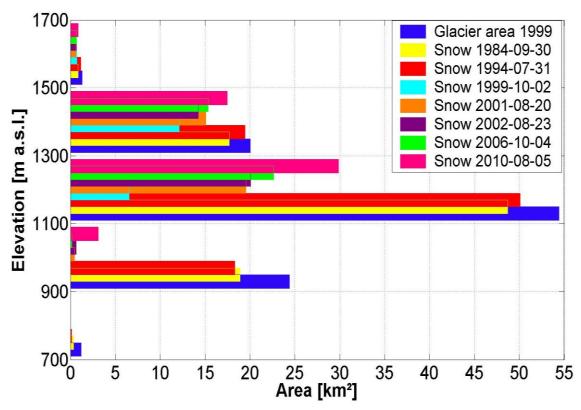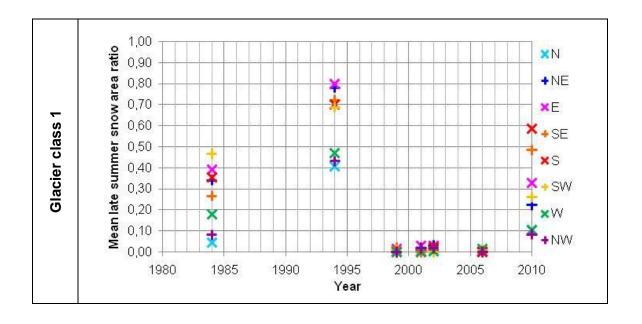
Figure 5.31: Area altitude distribution of snow areas in several years between 1984 and 2010 and the total area of the glaciers on and around Blåmannsisen, Norway. Elevations are derived from the national DEM, and areas are grouped into 200 m elevation intervals.

The glaciers of and around Blåmannsisen are located at higher elevations, between about 700 m a.s.l. and 1700 m a.s.l., with the main glacier area between 1100 m a.s.l. and 1300 m a.s.l.. The previously described annual distribution of the late summer snow area extents can also be observed for Blåmannsisen, with a few differences. In 1984, the late summer snow area extent between 700 m a.s.l. and 1100 m a.s.l. was slightly larger

compared to that of 1994, and above 1100 m a.s.l. the late summer snow area extents were similar in both years with slightly smaller area in 1984. Only in these two years late summer snow areas were derived for elevations lower than 900 m a.s.l.. The derived late summer snow area extents for the years 2001 and 2002 are very similar in all elevation intervals. The differences between the derived snow extents for the years 1999 and 2006 are indeed partly significant, especially in the elevation interval between 1100 m a.s.l. and 1300 m a.s.l.. Above 1500 m a.s.l. the derived snow extents are similar for all investigated years.

Investigating the mean LSSAR of individual glaciers in dependence of the glacier size and the orientation shows in many years the trend of the derived LSSARs for the total glacier areas. The temporal changes of the mean LSSARs vary significantly even for glaciers with a specific orientation and glacier size. The largest glaciers show the smallest variations in most of the investigated years. The individual LSSARs of glaciers belonging to class 1 and 2 cover almost the full possible range of the snow area ratio, but the highest mean LSSARs in these glacier classes were derived for east and southwest orientated glaciers in many of the investigated years. North and northwest orientated glaciers of class 1, 2 and 3 have comparatively small mean snow area ratios in most of the investigated years. South and southeast orientated glaciers of class 1 and 2 have in most of the investigated years mean LSSARs in the medium part of the LSSAR ranges. In glacier class 3 high mean LSSARs were derived for glaciers with these orientations, but west orientated glaciers of class 3 have the largest mean LSSARs in the investigated years between 1999 and 2006. In the other years, and also for smaller west orientated glaciers the derived mean LSSAR are rather in the medium part of the value ranges. In glacier class 4, the highest mean LSSARs were derived for north, west, and northwest orientated glaciers, while these of north, east and southeast orientated glaciers are rather small.
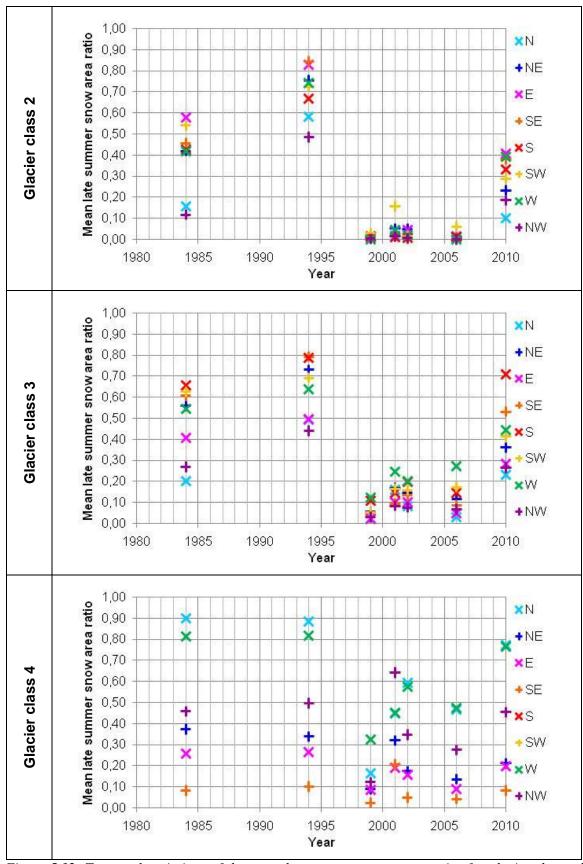
Figure 5.32: Temporal variations of the mean late summer snow area ratios for glaciers located in Svartisen and Blåmannsisen, Norway, considering the glacier areas and the main glacier aspects.

6. Summary and conclusions

A semi-automated algorithm was developed for the retrieval of snow areas on glaciers and icecaps in different climate regions. Multispectral optical satellite images (e.g. by Landsat) acquired close to the end of summer, without cloud coverage on the glaciers of interest and the surroundings, digital elevation data and glacier outlines, preferably meeting the GLIMS standards, are required as input. The algorithm can be split into three parts:

1. Data preparation, radiometric calibration, topographic correction and data overlay.

2. Threshold selection in the topographically corrected reflectance image and mapping of snow and ice areas on glaciers.

3. Statistical analysis of the derived snow and ice areas.

The first and the last step can each be executed automatically. The second part requires some visual controlling with auxiliary maps and human expertise to find the best threshold for separating snow and ice areas on all glaciers covered by one scene.

The processing line is based on the near infrared band of Landsat. Several methods to correct the Landsat imagery for illumination effects and partly also atmospheric propagation were tested. Additionally, an atmospheric correction scheme using the radiative transfer model 6S was tested on a Landsat scene over the Ötztal Alps, Austria. The results of all tested correction methods were compared. The Ekstrand correction was finally selected as standard topographic correction for the processing line.

The snow and ice areas on glaciers derived by the processing line from Landsat images were validated against snow and ice area extents that were manually mapped from orthophotos of selected glaciers in Austria and Norway. To be suitable for the validation of the snow and ice areas on glaciers, the Landsat scene and the orthophoto have to be acquired ideally on the same date or within a time difference of only a few days. This significantly reduces the data available for validation purposes. In order to check the effects of topographic data on quality of the retrieved LSSIA, the impact of using different DEMs for topographic correction was investigated. In addition, the impact of changing the threshold for the segmentation of LSSIA was tested.

The processing line was applied to map snow and ice areas on glaciers located in Alaska, Austria, Norway, Chile, Nepal, and on icecaps on the Baffin Island in the Canadian Arctic and in northeast Greenland. To investigate the spatial variability, Landsat scenes of the summers 2000 and 2001, depending on the availability of images meeting the requirements, were investigated in the selected regions. The snow areas covered comparatively large parts of the glaciers of the Harding Icefield and the Grewingk-Yalik Glacier Complex in Alaska. In those years, about half of the glacier areas were covered by snow on the Sargent Icefield in Alaska, in the Stubai Alps in Austria, on the North

Patagonian Icefield in Chile and on the Flade Isblink in Greenland. In all other regions the derived ratios of snow area to total glacier area were significantly smaller, with the lowest ratio on the Barnes Icecap.

As such a snapshot does not necessarily represent the long-term behaviour of snow and ice areas on glaciers, temporal variations between the mid-1980s and 2010 were investigated for glaciers in all study regions except northeast Greenland, where no further Landsat images meeting the requirements were available. Digital elevation models were combined with LSSIA maps to investigate the snow area altitude distributions in different years. The temporal variations of the snow areas were not only analysed for the total glacier area in each region, but also for individual glaciers in dependence of glacier size and glacier orientation. The derived snow areas are related to the areas of all glaciers in a region, and of individual glaciers to derive the late summer snow area ratio (LSSAR) as proxy for the accumulation area ratio (AAR), a measure for a glacier's mass balance. For some glaciers mean values or even time series of the AAR are reported in the literature. If such data is available, the derived snow area ratios were compared to these values. In order to search for relations between the temporal variations of the snow areas and climatic trends, the results were investigated considering the associated monthly temperature and precipitation anomalies from NCEP / NCAR Reanalysis data.

In all investigated regions a trend to a decrease of snow areas on glaciers in late summer can be observed over the investigation period. Considering the total glacier area in each region, the derived overall snow area ratios are in most of the years lower than the typical AAR for glaciers in equilibrium. The main retreat of the snow areas occurs in the elevation ranges where also the main glacier areas can be found, while the changes are small in the uppermost elevations. Although the glaciers in different climate zones extend over different elevation ranges, the percental distributions of the glacier area with the altitude are similar for the glacier regions in Norway and the Alps, and for the North Patagonian Icefield in Chile and glaciers of the Sagarmatha basin in Nepal. All investigated glacier regions on the Kenai Peninsula in Alaska have similar glacier area altitude distributions, with the maximum glacier area being highest for glaciers on and around the Harding Icefield and lowest for glaciers on and around the Sargent Icefield. The two icecaps in the Canadian Arctic and Greenland have completely different altitude distributions of the glacier areas.

The long-term investigation of snow areas suggests that glaciers extending over a large elevation range, such as the North Patagonian Icefield in Chile or the glaciers of the Sagarmatha basin in Nepal, are less sensitive to climate changes than glaciers extending only over a few hundred meters, as for example the Barnes Icecap in the Canadian Arctic. On the North Patagonian Icefield and on the glaciers in the Sagarmatha basin the multi–year variations of summer snow areas were significantly smaller than in the other glacier regions. But a tendency to smaller snow areas since 2002 is obvious for glaciers in all regions. On the Barnes Icecap, the lowest overall LSSAR derived from the Landsat

imagery was found in 2010 with only 1 % remaining snow cover in mid of August on the total icecap. It can be assumed that at the end of the melting season no winter snow remained on the icecap. In regions with large elevation ranges the changes in the accumulation areas in the uppermost glacier regions are negligible. For the investigated regions the Harding Icefield shows the highest LSSARs in many of the investigated years. On the neighboured Sargent Icefield and the Grewingk-Yalik Glacier Complex the derived LSSARs are in some years similar to these of the Harding Icefield, but show large differences in other years. Rather similar LSSARs in neighboured areas can be observed for the glaciers regions in Austria and in Norway in some years, but this observation cannot be generalised.

Investigations of the snow areas in relation to the glacier size and the glacier exposition showed that small glaciers of all aspects are very sensitive to annual changes in temperature and precipitation. But the influences of strong annual temperature or precipitation anomalies can also be observed on larger glaciers. The preferred glacier aspects for preserving snow areas depend on the local topography of each region and the local meteorological conditions.

The thesis reports on an investigation of late summer snow areas on glaciers in different geographic regions and over a time span of many years, exploiting a potential of high resolution optical satellite data for glacier studies which so far has received little attention. The derived results point out the large potential of satellite data to regularly deliver basic key features for mass balance investigations on glaciers worldwide. Remote sensing data thereby enables the observation of glaciers from local to global scale. For Landsat imagery used in this study, the revisit time of 16 days and frequent cloud coverage over glaciated areas are the main limiting factors for regular observations of glacier surfaces. For mapping snow areas as mass balances indicators, the image has to be acquired near the end of a mass balance year, which in the Alps is about end of September.

In order to obtain comprehensive information on glacier response to changing climate, it is recommended to extend the time range and geographic coverage of satellite data analysis.

The available archives of satellite data enable retrospective analysis of glaciers including summer snow areas. This includes not only direct glaciological observations, but also the observation of melting glaciers contributing to the sea level rise.

Future satellites with high resolution optical sensors, such as the European Sentinel-2 satellite with the launch of the first satellite scheduled in 2013, will enable systematic image acquisitions within 10 days revisit time, improving to 5 days when two Sentinels are launched (Martimort et al., 2007). An additional advantage of the Sentinel-2 is the regular image acquisition over specific areas for extended time periods, which improves the chance of obtaining suitable images on glaciers in late summer. The aim in such a case is, to acquire the images within one to three days. The developed method might be

used after some adaptions also for further optical sensors to derive snow areas on glaciers, as this future Sentinel-2, or already available high resolution sensors working in the near infrared spectral range.

Additionally to glaciological observations, regular monitoring of snow area extent can support validation and improvement of weather and climate models regarding the parameterization of hydrospheric and cryospheric processes. In particular, for the validation of climate models estimating glacier mass balance, as for example the $REMO_{glacier}$ model presented by Kotlarski et al. (2010), the snow areas on glaciers should be useful, as these areas are governed by rather direct response to meteorological forcing, different to total glacier area, which typically has climatic response times of several years to decades.

Appendix A – Spectral ranges of optical sensors

Spectral range	Landsat 4/5 TM	Landsat 7 ETM +	ASTER	SPOT 1 - 5	Ikonos	Quickbird
Blue	0.45 - 0.52	0.45 - 0.515	-	-	0.445 - 0.516	0.45 - 0.52
Green	0.52 - 0.60	0.525 - 0.605	0.52 - 0.60	0.50 - 0.59	0.506 - 0.595	0.52 - 0.60
Red	0.63 - 0.69	0.63 - 0.69	0.63 - 0.69	0.61 - 0.68	0.632 - 0.698	0.63 - 0.69
NIR	0.76 - 0.90	0.78 - 0.90	0.78 - 0.86	0.78 - 0.89	0.757 - 0.853	0.76 - 0.90
SWIR	1.55 - 1.75	1.55 - 1.75	1.60 - 1.70	*4/5:* 1.58 - 1.75	-	-
SWIR	2.08 - 2.35	2.09 - 2.35	2.145 - 2.43	-	-	-
TIR	10.4 - 12.5	10.4 - 12.5	5 bands	-	-	-
Pan	-	0.52 - 0.90	-	*1-3:* 0.50 - 0.73	0.45 - 0.90	0.45 - 0.90
				4: 0.61 - 0.68		
				5: 0.48 - 0.71		

Table A.1: Spectral ranges of optical sensors: TM (Landsat 4/5), ETM+ (Landsat 7), ASTER (Terra), SPOT 1-5, Ikonos, Quickbird, and MODIS. For the Landsat and ASTER sensors also band numbers are given. The 5 ASTER thermal bands are not shown. The numbers in front of the SPOT spectral ranges refer to the satellite number. Abbreviations: NIR=near infrared, SWIR=shortwave infrared, TIR = thermal infrared, N/B=nadir/back looking.

Band	Landsat 4/5 TM [µm]	Landsat 7 ETM+ [µm]	ASTER [µm]	SPOT 1 – 5 [µm]	Ikonos [µm]
1	0.45 – 0.52	0.45 – 0.515	0.52 – 0.60	0.50 – 0.59	0.445 – 0.516
2	0.52 – 0.60	0.525 – 0.605	0.63 – 0.69	0.61 – 0.68	0.506 – 0.595
3	0.63 – 0.69	0.63 – 0.69	0.78 – 0.86 (N/B)	0.78 – 0.89	0.632 – 0.698
4	0.76 – 0.90	0.78 – 0.90	1.60 – 1.70	1.58 – 1.75 (SPOT 4/5)	0.757 – 0.853
5	1.55 – 1.75	1.55 – 1.75	2.145 – 2.185	0.50 – 0.73 (PAN, 1 – 3) 0.48 – 0.71 (PAN, 5)	---
6	10.40 – 12.50	10.40 – 12.50	2.185 – 2.225	0.61 – 0.68 (MONO, 4)	---
7	2.08 – 2.35	2.09 – 2.35	2.235 – 2.285	---	---
8	---	0.52 – 0.90	2.295 – 2.365	---	---
9	---	---	2.360 – 2.430	---	---
10	---	---	8.125 – 11.65 (failed in October 2007)	---	---
11	---	---	8.475 – 8.825	---	---
12	---	---	8.925 – 9.275	---	---
13	---	---	10.25 – 10.95	---	---
14	---	---	10.95 – 11.65	---	---

Table A.2: Spectral ranges of used optical sensors: Landsat 4/5 TM, Landsat 7 ETM+, ASTER, SPOT 1-5, and Ikonos.

Appendix B – Statistical overview on the case studies

Region / image acquisition date / LSSAR for all glaciers per region	Glacier class	MAX LSSAR	MIN LSSAR	MEAN LSSAR	LSSAR STDEV	Number of glaciers	% of total glacier area
Harding Icefield, AK	1	1,0000	0.0000	0.3156	0.3163	454	1
	2	0.9869	0.0000	0.4179	0.3286	234	4
12.08.2001	3	0.9624	0.0795	0.6108	0.2511	64	9
LSSAR$_{all}$ = 0.74	4	0.9212	0.4540	0.7405	0.1330	16	29
	5	0.9190	0.5736	0.7616	0.1223	6	57
Sargent Icefield, AK	1	0.8897	0.0000	0.2234	0.2809	762	1
	2	0.9055	0.0000	0.2420	0.2772	364	6
21.08.2001	3	0.8673	0.0000	0.2912	0.2577	119	16
LSSAR$_{all}$ = 0.54	4	0.8533	0.0000	0.4491	0.2428	36	42
	5	0.8711	0.6083	0.7040	0.1069	4	35
Grewingk-Yalik	1	0.8338	0.0000	0.2681	0.2300	175	2
Glacier Complex, AK	2	0.9134	0.0000	0.3970	0.2479	81	5
09.08.2000	3	0.8922	0.4904	0.6812	0.1308	11	9
LSSAR$_{all}$ = 0.65	4	0.8413	0.4965	0.6679	0.0931	12	84
	5					0	0
Ötztal Alps, AT	1	0.7256	0.0000	0.2045	0.1876	74	2
	2	0.7957	0.0000	0.2019	0.2215	105	21
15.09.2000	3	0.7302	0.0000	0.2002	0.1969	27	66
LSSAR$_{all}$ = 0.39	4	0.2436	0.2436	0.2436	0.0000	1	11
	5					0	0
Stubai Alps, AT	1	0.8095	0.0000	0.2554	0.2799	27	4
	2	0.6872	0.0000	0.3675	0.2099	35	33
15.09.2000	3	0.8096	0.0176	0.4225	0.2336	11	63
LSSAR$_{all}$ = 0.49	4					0	0
	5					0	0

Sagarmatha basin,	1	0.8801	0.0000	0.2268	0.2410	47	1
NP	2	0.9568	0.0000	0.3288	0.2650	107	12
17.10.2001	3	0.8294	0.0000	0.3359	0.2282	35	29
$LSSAR_{all} = 0.33$	4	0.4365	0.1466	0.2850	0.0849	6	58
	5					0	0
Svartisen /	1	0.3182	0.0000	0.0120	0.0445	125	1
Blåmannsisen, NO	2	0.4319	0.0000	0.0338	0.0681	246	14
20.08.2001	3	0.6502	0.0000	0.1382	0.1607	100	42
$LSSAR_{all} = 0.23$	4	0.6965	0.0524	0.3561	0.2233	12	43
	5					0	0
North Patagonian	1					0	0
Icefield, CL	2	0.6523	0.0824	0.4393	0.1796	9	0
08.03.2000	3	0.7204	0.0000	0.2822	0.2546	64	6
$LSSAR_{all} = 0.45$	4	0.7307	0.0000	0.3395	0.2232	28	20
	5	0.8228	0.3587	0.5674	0.1293	9	74
Barnes Icecap, CA	1					0	
	2					0	
08.08.2001	3					0	
$LSSAR_{all} = 0.15$	4					0	
	5					0	
	6	0.1532	0.1532	0.1532	0.0000	1	100
Flade Isblink, GL	1					0	
	2					0	
03.07.2001	3					0	
$LSSAR_{all} = 0.51$	4					0	
	5					0	
	6	0.5100	0.5100	0.5100	0.0000	1	100

Table B.1: Minimum, maximum, mean late summer snow area ratios, number of glaciers and the percentage of the total glacier area per glacier class in the selected regions derived from Landsat data of 2000 and 2001, respectively. The LSSARs for all investigated glaciers in the individual regions are added in the first column.

References

ACIA (2005) Arctic Climate Impact Assessment. Available at: http://www.acia.uaf.edu.

Abdalati W, Krabill W, Frederick E, Manizade S, Martin C, Sonntag J, Swift R, Thomas R, Yungel J, Koerner R (2004) Elevation changes of ice caps in the Canadian Arctic Archipelago. Journal of Geophysical Research 109:11.

Abermann J, Lambrecht A, Fischer A, Kuhn M (2009) Quantifying changes and trends in glacier area and volume in the Austrian Ötztal Alps (1969-1997-2006). The Cryosphere 3:415-441.

Adalgeirsdóttir G, Echelmeyer KA, Harrison WD (1998) Elevation and volume changes on the Harding Icefield, Alaska. Journal of Glaciology 44:570 - 582.

Andreassen LM, Elvehoy H, Kjollmoen B, Engeset RV, Haakensen N (2005) Glacier mass-balance and length variation in Norway. Annals of Glaciology 42:317 – 325.

Andrews JT, Holdsworth G, Jacobs JD (2002) Glaciers of Canada. U.S. Geological Survey Professional Paper 1386-J-1:37.

Angelis H De, Rau F, Skvarca P (2007) Snow zonation on Hielo Patagónico Sur, Southern Patagonia, derived from Landsat 5 TM data. Global and Planetary Change 59:149-158.

Aniya M (1988) Glacier inventory for the Northern Patagonian Icefield, Chile, and variations 1944/45 to 1985/86. Arctic and Alpine Research 20:179 - 187.

Aniya M (2007) Glacier variations of Hielo Patagónico Norte, Chile, for 1944/45 - 2004/05. Bulletin of Glaciological Research 24:59-70.

Aniya M, Sato H, Naruse R, Skvarca P, Casassa G (1996) The use of satellite and airborne imagery to inventory outlet glaciers of the Southern Patagonian Ice field, South America. Photogrammetric Engineering and Remote Sensing 62:1361 - 1369.

Armenakis C (2008) Determination of geospatial changes of the Barnes Ice Cap using EO data. The International Archives of the Photogrammetry, Remote Sensing and Spatial Information Sciences 37:1437-1442.

Bamber JL, Rivera A (2007) A review of remote sensing methods for glacier mass balance determination. Global and Planetary Change 59:138-148.

Benson CS (1958) Physical investigations on the snow and firn of Northwest Greenland during 1952, 1953, and 1954. Trans. Am. Geophysl. Union 39:538.

Beusekom A Van, O'Neel SR, March RS, Sass LC, Cox LH (2010) Re-analysis of Alaskan Benchmark Glacier Mass-Balance Data Using the Index Method. USGS Scientific Investigations Report:16 pp.

References

Bhatt BC, Nakamura K (2005) Characteristics of Monsoon Rainfall around the Himalayas Revealed by TRMM Precipitation Radar. Monthly Weather Review 133:149-165.

Bindschadler R, Dowdeswell J, Hall D, Winther JG (2001) Glaciological applications with Landsat-7 imagery: Early assessments. Remote Sensing of Environment 78:163 – 179.

Bippus G (2007) Modelling Mass Balance and Climate Sensitivity of Glaciers of the Southern Patagonia Icefield. Diploma Thesis at the University of Innsbruck, Austria:111 pp.

Braithwaite RJ (1984) Can the mass balance of a glacier be estimated from its equilibrium-line altitude? Journal of Glaciology 30:364-368.

Braun M, Schuler TH, Hock R, Brown I, Jackson M (2007) Remote sensing derived glacier facies maps at Engabreen, northern Norway. IAHS Red Books.

Chander G, Markham BL, Helder DL (2009)(a) Summary of current radiometric calibration coefficients for Landsat MSS, TM, ETM+, and EO-1 ALI sensors. Remote Sensing of Environment 113:893 - 903.

Chander G, Markham BL, Helder DL (2009)(b) Summary of current radiometric calibration coefficients for Landsat MSS, TM, ETM+, and EO-1 ALI sensors. Remote Sensing of Environment 113:893-903.

Cogley G (2009) A more complete version of the World Glacier Inventory. Annals Of Glaciology 50:32-38.

Cuffey KM, Paterson WSB (2010) The Physics of Glaciers - Fourth edition. Butterworth-Heinemann, Elsevier.

Dozier J (1989) Spectral signature of alpine snow cover from Landsat 5 TM. Remote Sensing of Environment 28:9 - 22.

Dyurgerov M, Meier MF, Bahr DB (2009) A new index of glacier area change: a tool for glacier monitoring. Journal of Glaciology 55:710-716.

Dyurgerov MB (1996) Substitution of long-term mass balance data by measurements of one summer. Zeitschrift für Gletscherkunde und Glazialgeologie 36:177-184.

Ekstrand S (1996) LandsatTM - based forest damage assessment: correction for topographic effects. Photogrammetric Engineering and Remote Sensing 62:151 – 161.

Fischer A (2010) Glaciers and climate change: Interpretation of 50years of direct mass balance of Hintereisferner. Global and Planetary Change 71:13-26.

Floricioiu D, Rott H, Fischer A, Oberparleiter C, Nagler T, Rack W (2002) Multi-Sensor and Interferometric Retrieval Techniques. Final Report: ESA Contract No. 14568/00/NL/JA:107 pp.

Gao Y, Zhang W (2009) A simple empirical topographic correction method for ETM+ imagery. International Journal of Remote Sensing 30:2259-2275.

Giffen BA, Hall DK, Chien JYL (2007) Alaska: Glaciers of Kenai Fjords National Park and Katmai National Park and Preserve (Chapter 12). NASA Technical Reports Server Web Site, Goddard Space Flight Center:20 pp.

Greuell W, Oerlemans J (2005) Validation of AVHRR- and MODIS-derived albedos of snow and ice surfaces by means of helicopter measurements. Journal of Glaciology 51:37 – 48.

Gross GH, Kerschner H, Patzelt G (1977) Methodische Untersuchungen über die Schneegrenze in alpinen Gletschergebieten. Zeitschrift für Gletscherkunde und Glazialgeologie 12:223-251.

Hall DK, Chang ATC, Siddalingaiah H (1988) Reflectances of glaciers as calculated using Landsat-5 Thematic Mapper data. Remote Sensing of Environment 25:311-321.

Hall DK, Martinec J (1985) Remote sensing of ice and snow. New York: Chapman and Hall.

Hall DK, Ormsby JP, Bindschadler RA, Siddalingaiah H (1987) Characterization of snow and ice zones on glaciers using Landsat Thematic Mapper data. Annals of Glaciology 9:104 - 108.

Hall DK, Riggs GA (2007) Accuracy assessment of the MODIS snow products. Hydrological Processes 21:1534- 1547.

Hoinkes H (1970) Methoden und Möglichkeiten von Massenhaushaltsstudien auf Gletschern. Ergebnisse der Messreihe Hintereisferner (Ötztaler Alpen) 1953–1968. Zeitschrift für Gletscherkunde und Glazialgeologie 6:37-90.

Jarvis A, Reuter HI, Nelson A, Guevara E (2008) Hole-filled SRTM for the globe Version 4, available from the CGIAR-CSI SRTM 90m Database. Available at: http://srtm.csi.cgiar.org.

Jorden WJ (1957) Soviet Fires Earth Satellite Into Space. The New York Times.

Kalnay E (1996) The NCEP-NCAR 40-years reanalysis project. Bulletin of the American Meteorological Society 77:437 - 471.

Kiehl JT, Trenberth KE (1997) Earth's Annual Global Mean Energy Budget. Bulletin of the American Meteorological Society 78:197-197.

Knap WH, Brock BW, Oerlemans J, Willis IC (1999)(a) Comparison of Landsat TM-derived and ground-based albedos of Haut Glacier d'Arolla, Switzerland. International Journal of Remote Sensing 20:3293-3310.

Knap WH, Reijmer CH, Oerlemans J (1999)(b) Narrowband to broadband conversion of Landsat TM glacier albedos. International Journal of Remote Sensing 20:2091 – 2110.

References

Kommission für Glaziologie der BAdW M (2010) Kenngrößen des Massenhaushaltes des Vernagtferners für den Zeitraum 1964 bis 2009. www.glaziologie.de.

Korona J, Berthier E, Bernard M, Remy F, Thouvenot E (2009) SPIRIT. SPOT 5 stereoscopic survey of Polar Ice: Reference Images and Topographies during the fourth International Polar Year (2007-2009). ISPRS Journal of Photogrammetry and Remote Sensing 64:204-212.

Kotchenova SY, Vermote E, Tanré D, Deuzé JL, Herman M, Morcrette JJ (2006)(a) Second Simulation of the Satellite Signal in the Solar Spectrum – Vector (6SV) User Guide Version 3.

Kotchenova SY, Vermote EF (2007) Validation of a vector version of the 6S radiative transfer code for atmospheric correction of satellite data. Part II: Homogeneous Lambertian and anisotropic surfaces. Applied Optics 46:4455 – 4464.

Kotchenova SY, Vermote EF, Matarrese R, Klemm FJJ (2006)(b) Validation of a vector version of the 6S radiative transfer code for atmospheric correction of satellite data. Part I: Path radiance. Applied Optics 45:6762 – 6774.

Kotlarski S, Jacob D, Podzun R, Paul F (2010) Representing glaciers in a regional climate model. Climate Dynamics 34:27-46.

Kulkarni AV (1992) Mass balance of Himalayan glaciers using AAR and ELA methods. Journal of Glaciology 38:101-104.

König M (2001) Measuring snow and glacier ice properties from satellite. Reviews of Geophysics 39:27 pp.

Lambrecht A, Kuhn M (2007) Glacier changes in the Austrian Alps during the last three decades, derived from the new Austrian glacier inventory. Annals of Glaciology 46:177-184.

Law KH, Nichol J (2004) Topographic correction for differential illumination effects on Ikonos satellite imagery. Proceedings of XXth ISPRS Congress: Geo-imagery bridging continents, Istanbul, Turkey, ISPRS 35:6 pp.

Martimort P, Berger M, Carnicero B, Bello U Del, Fernandez V, Spoto F, Sy O, Arino O, Biasutti R, Greco B (2007) Sentinel-2: The Optical High-Resolution Mission for GMES Operational Services. ESA Bulletin 131:18 - 23.

McClatchey RA, Fenn RW, Selby JEA, Volz FE, Garing JS (1971) Optical properties of the atmosphere.

McDonald ER, Wu X, Caccetta P, Campbell N (2000) Illumination correction of Landsat TM data in south east NSW. Proceedings of the Tenth Australasian Remote Sensing Conference.:13 pp.

Meier MF, Post AS (1962) Recent variations in mass net budgets of glaciers in western North America. In: Symposium of Obergurgl (on Variations of the Regime of Existing Glaciers) IAHS 58:63 - 77.

Meyer P, Itten KI, Kellenberger T, Sandmeier S, Sandmeier R (1993) Radiometric corrections of topographically induced effects on Landsat TM data in alpine terrain. ISPRS:20 pp.

Minnaert N (1941) The Reciprocity Principle in Lunar Photometry. Astrophysical Journal 93:403 - 410.

Müller F (1962) Zonation in the accumulation area of the glaciers of Axel Heiberg Island, N.W.T., Canada. Journal of Glaciology 4:302-310.

Ohmura A (2009) Completing the World Glacier Inventory. Annals of Glaciology 50:144-148.

Orthophotokarte (2001) Vernagtferner 1999 (Maßstab 1:10000).

Owen L, Benn D (2005) Equilibrium-line altitudes of the Last Glacial Maximum for the Himalaya and Tibet: an assessment and evaluation of results. Quaternary International 138:55-78.

Parajka J, Blöschl G (2006) Validation of MODIS snow cover images over Austria. Hydrology and Earth System Sciences 10:679-689.

Paterson WSB (1981) The Physics of Glaciers (2nd edition). Pergamon Press, New York.

Paul F, Barry RG, Cogley JG, Frey H, Haeberli W, Ohmura A, Ommanney CSL, Raup B, Rivera A, Zemp M (2010) Guidelines for the compilation of glacier inventory data from digital sources. 1.0:23 pp.

Pfeffer WT, Bretherton CS (1987) The effect of crevasses on the solar heating of a glacier surface In The Physical Basis of Ice Sheet Modelling (Proceedings of the Vancouver Symposium) IAHS Publ. no. 170: 191-206.

Rabatel A, Dedieu JP, Vincent C (2005) Using remote-sensing data to determine equilibrium-line altitude and mass-balance time series: validation on three French glaciers, 1994–2002. Journal of Glaciology 51:539 - 546.

Racoviteanu AE, Paul F, Raup B, Khalsa JSJ, Armstrong R (2009) Challenges and recommendations in mapping of glacier parameters from space: results of the 2008 Global Land Ice Measurements from Space (GLIMS) workshop, Boulder, Colorado, USA. Annals of Glaciology 50:53-69.

Rasmussen LA, Conway H, Raymond CF (2007) Influence of upper air conditions on the Patagonia icefields. Global and Planetary Change 59:203-216.

Rau F, Mauz F, Vogt S, Jodha S, Khalsa S, Raup B (2005) Illustrated GLIMS Glacier Classification Manual. :1-36.

References

Raup B, Khalsa SJS (2010) GLIMS Analysis Tutorial. :pp. 16 Available at: http://www.glims.org.

Raup B, Khalsa SJS, Racoviteanu A, Helm C, Armstrong R, Arnaud Y (2007) The GLIMS geospatial glacier database: A new tool for studying glacier change. Global and Planetary Change 56:101 – 110.

Raup BH, Kieffer H, Hare TM, Kargel JS (2000) Generation of data acquisition request for the ASTER satellite instrument for monitoring a globally distributed target: Glaciers. IEEE Transactions on Geosciences and Remote Sensing 38:1-10.

Richter R, Kellenberger T, Kaufmann H (2009) Comparison of Topographic Correction Methods. Remote Sensing 1:184-196.

Riggs GA, Hall DK, Salomonson VV (1994) A snow index for the Landsat Thematic Mapper and Moderate Resolution Imaging Spectroradiometer In Geoscience and Remote Sensing Symposium International: IGARSS '94. Surface and Atmospheric Remote Sensing: Technologies, Data Analysis and Interpretation., p. 1942-1944.

Rivera A, Benham T, Casassa G, Bamber J, Dowdeswell J (2007) Ice elevation and areal changes of glaciers from the Northern Patagonia Icefield, Chile. Global and Planetary Change 59:126-137.

Rott H, Markl G (1989) Improved snow and glacier monitoring by Landsat Thematic Mapper. Proceedings of a workshop on Earthnet Pilot Project on Landsat Thematic Mapper Applications ESA SP-110:3 - 12.

Scaramuzza P (2002) LPGS / NLAPS Level 1 Product Radiometric Comparison. :1-17.

Schicker I (2006) Changes in Area of Stubai Glaciers analysed by means of Satellite Data for the GLIMS Project. Diploma Thesis at the University of Innsbruck, Austria:89 pp.

Singh P, Ramasastri KS, Kumar R (1995) Topographical influence on precipitation distribution in different ranges of western Himalaya. Nordic Hydrology 26:259-284.

Sneed WA, Hooke RL, Hamilton GS (2008) Thinning of the south dome of Barnes Ice Cap, Arctic Canada, over the past two decades. Geology 36:71-74.

Takeuchi N (2009) Temporal and spatial variations in spectral reflectance and characteristics of surface dust on Gulkana Glacier, Alaska Range. Journal of Glaciology 55:701-709.

Teillet PM, Guindon B, Goodenough DG (1982) On the slope-aspect correction of multispectral scanner data. Canadian Journal of Remote Sensing 8:84 - 106.

Törma M, Härmä P (2003) Topographic correction of Landsat ETM-Images in Finish Lapland. Geoscience and Remote Sensing Symposium, 2003. IGARSS '03.Proceedings. 2003 IEEE International 6:3629 – 3631.

U.S. Department of Commerce, National Oceanographic and Atmospheric Administration, Earth System Research Laboratory, Physical Science Division (2011) NCEP / NCAR Reanalysis 1981 - 2010. Available at: http://www.esrl.noaa.gov/psd/cgi-bin/data/composites/printpage.pl [Accessed July 2011].

Vermote E, Tanré D, Deuzé JL, Herman M, Morcrette JJ (1997) Second Simulation of the Satellite Signal in the Solar Spectrum - User Guide Version 2.

WGMS (2008) Global Glacier Changes : facts and figures. Contents: M. Zemp, I. Roer, A. Kääb, M. Hoelzle, F. Paul, and W. Haeberli, eds. UNEP, World Glacier Monitoring Service, Zurich, Switzerland.

WMO, IOC, UNEP, ICSU (2010) Implementation plan for the global observing system for climate in support of the UNFCCC. GCOS-138 GOOS-148, :180 pp.

Warren SG (1982) Optical properties of snow. Reviews of Geophysics and Space Physics 20:67 - 89.

Williams RS, Hall D, Benson CS (1991) Analysis of glacier facies using satellite techniques. Journal of Glaciology 37:120 - 128.

Wiscombe WJ, Warren SG (1980) A model for the spectral albedo of snow, I, pure snow. Journal of Atmospheric Science 37:2712 - 2733.

Zemp M, Hölzle M, Häberli W (2009) Six decades of glacier mass-balance observations: a review of worldwide monitoring network. Annals of Glaciology 50:101 - 111.

Ziegler M, Schardt M, Granica K, Gallaun H (2006) Topographic Normalisation – best practice guide. Integrated Project geoland, EC Proposal Reference No. FP-6-502871 CSL-0350-R:10 pp.

References

Acknowledgements

Curriculum Vitae

PERSONAL DATA:

Name:	Gabriele Maria Bippus
Date of birth:	16 May 1981
Address:	Müllerstr. 31, 6020 Innsbruck, AUSTRIA
E-Mail:	gabriele.bippus@enveo.at
Nationality:	German

SCHOOL:

1987—1991	Elementary school, Tittmoning, Germany
1991 - 2000	High School at the Kurfürst – Maximilian Gymnasium, Burghausen, Germany
2000	School Leaving Exam

STUDIES:

2000 – 2007	Diploma study of Meteorology and Geophysics at the University of Innsbruck, Austria
2006 – 2007	Master thesis under supervision of Prof. Helmut Rott:
	'Modelling Mass Balance and Climate Sensibility of Glaciers of the Southern Patagonia Icefield'
April 2007	Graduation (Mag.rer.nat) in Meteorology and Geophysics
2007 – 2011	PhD study at the Department of Meteorology and Geophysics, University of Innsbruck, Austria
Sept 2008	Regular student at the IMAU - Summer School in Karthaus, Italy, on 'Glaciers and Ice sheets in the climate system'

VOCATIONAL EXPERIENCE:

Summer 1997	Vacation job at the Rosenberger Hochfrequenztechnik GmbH & Co., Fridolfing, Germany
Summer 1998	Vacation job at the order processing of the Hermann OTTO GmbH, Fridolfing, Germany

Curriculum Vitae

2000 – 2003	Vacation job at the accounts department and order processing of the Hermann OTTO GmbH, Fridolfing, Germany
2003 – 2007	Regular field work on alpine glaciers (e.g. mass and energy balance, ice thickness measurements, velocity measurements)
Summer 2005	Professional practical training at the meteorological bureau of the Airport Innsbruck, Austria
Since May 2007	Scientific employee at ENVEO IT GmbH
Jun 2007 – Feb 2008	Contract work: digitisation of mass balance maps 1953 – 2006 of Hintereisferner, Austria. Principal: Dr. Andrea Fischer, Institute of Meteorology and Geophysics, University of Innsbruck, Austria
Nov 2007 – Nov 2010	Main project at ENVEO IT GmbH: ESA DUE GlobGlacier
Winter 2007	Participation on field campaigns within the project ESA-KU-Band SAR - Measurements for Snow Applications: Modelling and Sensitivity (Prime Contractor,2005-2006) of ENVEO IT GmbH in cooperation with Keith Morrison of the University of Sheffield and ESA
Summer 2009	Field work on glaciers in Norway (mass and energy balance, terminus position measurements)

TEACHING EXPERIENCE:

2005 – 2006	Tutor for exercise courses to theoretical meteorology
2008 – 2009	Tutor for exercise courses to remote sensing in glaciology

SPECIAL QUALIFICATIONS:

Languages:	German: native language
	English: spoken and written very well
	French: basics
Computer skills:	MS Office, GRASS GIS, QGIS, C, Python, Linux, MySQL, LaTex, Matlab, ArcGIS
	Basic skills: HTML, Fortran

LIST OF PUBLICATIONS AND PRESENTATIONS

Monograph

Bippus, G., 2007: Modelling mass balance and climate sensibility of glaciers of the Southern Patagonia Icefield. *Diploma Thesis, University of Innsbruck, Austria, 111 pp.*

Peer – Review publications

Rott, H., T. Nagler, P. Malcher and G. Bippus, 2007: Modelling mass balance of glaciers using satellite data. *Proc. Envisat Symposium 2007, Montreux, Switzerland, 23-27 April 2007 (ESA SP-636, July 2007), 6 pp.*

Zemp, M., F. Paul, L.M. Andreassen, O. Arino, G. Bippus, T. Bolch, R. Braithwaite, L. Braun, B.E. Cáceres, G. Casassa, K.A. Casey, C.L. Ceballos, M. Citterio, H. Delgado, M. Demuth, L.E: Espizua, A. Farokhnia, A. Fischer, N. Foppa, H. Frey, K. Fujita, I. Gärtner-Roer, P. Glowacki, W. Haeberli, J.O. Hagen, M. Hoelzle, P. Holmlund, R.H. Giesen, A. Kääb, T. Khromova, S. Kotlarski, R. Le Bris, Z. Li, M. Meier, M., Meneghel, P. Mool, S.U. Nussbaumer, P. Peduzzi, S. Plummer, V.V. Popovnin, R. Prinz, W. Rack, P. Rastner, B. Raup, E. Rinne, F.M. Seifert, G. Seiz, I. Severskiy, A. Shepherd, O. Sigurðsson, T. Strozzi, C. Vincent, R. Wheate, and A. Yakovlev, 2011: Summary of international glacier monitoring summit. *The Earth Observer, 23 (4): p. 28-31.*

Poster

Bippus, G., L. Nicholson and R. Prinz, 2010: Satellite mapping of snow cover extent on Mt Kenia, 2000 – 2009. *Poster presentation: Workshop on Cold Regions Hydrology, 28. – 30.04.2010, Innsbruck, Austria.*

Oral presentations at summer schools, symposiums, and conferences

G. Bippus, H. Rott and T. Nagler, 2009: Automated mapping of snow and ice areas on glaciers from optical satellite data as contribution to the ESA project GlobGlacier. *Alpine Glaciology Meeting, Innsbruck, Austria, 26.02.2009.*

G. Bippus, H. Rott and T. Nagler, 2009: Automated retrieval of snow and ice areas on glaciers from optical satellite data. (*Invited). Hydrology Department at Norwegian Water Resources and Energy Directorate, Oslo, Norway, 21.09.2009.*

F. Paul, H. Frey, R. LeBris and G. Bippus, 2010: Mapping glaciers, snow and albedo. *RSL, Zurich, Switzerland, 16.06.2010.*

G. Bippus and H. Rott, 2010: Spatial and temporal pattern of snow and ice area extent in late summer in various glacier regions of the world observed by Landsat. *24ᵗʰ International Polar Meeting, Obergurgl, Austria, 06.-10.09.2010.*

Publications with the GlobGlacier consortium:

Paul, F., G. Bippus, K.A. Casey, H. Frey, A. Kääb, R. LeBris, T. Nagler, E. Rinne, H. Rott, A. Shepherd, T. Strozzi, F.M. Seifert (until Feb. 2010) and S. Plummer (since Feb. 2010):

Poster

GlobGlacier: A new ESA project to map the world's glaciers and ice caps from space. *EGU General Assembly, Vienna, Austria, 14. – 18.04.2008.*

GlobGlacier: A new ESA project to map and monitor the world's glaciers from space. *IGS Workshop on World Glacier Inventory, Lanzhou, China, 20. – 24. 09.2008.*

GlobGlacier: A new ESA project to map and monitor the world's glaciers from space. *HMRSC Workshop, Kathmandu, Nepal, 08. – 11.09.2008.*

Mapping the world's glaciers from space: First results from the ESA project GlobGlacier. *Poster presentation: MOCA, IAMAS – IAPSO – IACS Joint Assembly, Montreal, Canada, 19. – 29.07.2009.*

Mapping the world's glaciers from space: Results from the ESA project GlobGlacier. *EGU General Assembly, Vienna, Austria, 02. – 07.05.2010.*

Oral presentations at summer schools, symposiums, and conferences

Mapping the world's glaciers and ice caps from space for improved climate change impact assessment. *EARSeL workshop on Remote Sensing of Land Ice and Snow, Berne, Switzerland, 11. – 13.02.2008.*

GlobGlacier: A new ESA project to map the world's glaciers and ice caps from space. *12ᵗʰ Alpine Glaciology Meeting, Grenoble, France, 06. – 07.03.2008.*

GlobGlacier: A new ESA project to map and monitor the world's glaciers from space. *(Invited). Colloquium in Remote Sensing, Remote Sensing Laboratories, University of Zurich (RSL), Switzerland, 16.10.2008.*

GlobGlacier : A new ESA project to map the world's glaciers from space. *6ᵗʰ Swiss Geoscience Meeting, Lugano, Switzerland, 14. – 16.11.2008.*

GlobGlacier: Mapping the world's glaciers and icecaps from space. *CryoClim Meeting, Oslo, Norway, 30.11.2009.*

Mapping the world's glaciers and icecaps from space: Results from the ESA project GlobGlacier. *Alpine Glaciology Meeting, Milan, Italy, 25. – 26.03.2010.*

Glaciers_cci. *ESA Living Planet Symposium, Bergen, Norway, 28.06. – 02.07.2010.*

Remote sensing of glaciers: current status and challenges. *(Invited). WGMS NC meeting, Zermatt, Switzerland, 03.09.2010.*

From the ESA project GlobGlacier to Glaciers_cci: Establishing a service for space-borne glacier monitoring. *6ᵗʰ EARSeL Workshop LISSIG, Bern, Switzerland, 07. – 09.02.2011.*

From the ESA project GlobGlacier to Glaciers_cci: Establishing a service for space-borne glacier monitoring + DVD presentation. *15ᵗʰ Alpine Glaciology Meeting, Munich, Germany, 24. – 25.02.2011.*